Coherent X-ray Scattering From Soft-Matter Surfaces

Dissertation

zur Erlangung des Doktorgrades der Naturwissenschaften
des Fachbereichs Physik der Universität Dortmund

vorgelegt von

Robert Fendt

Dezember 2006

Contents

List of Figures

List of Tables

1 Introduction

X-ray scattering techniques using coherent radiation, X-ray photon correlation spectroscopy (XPCS) in particular, are well-suited for the investigation of soft-matter systems. The effect of external total reflexion allows for surface-sensitive measurements, e.g. on liquid surfaces. Tuning of the photon energy allows for measurements that are sensitive to certain materials [66, 69, 95], and the possibility to penetrate opaque materials allows to study e.g. colloidal systems in higher concentrations or buried interfaces [57].

Modern synchrotron sources can provide X-rays with a high degree of coherence. For example, one can observe Fraunhofer diffraction [50, 52, 94] and speckle patterns [12, 49, 71, 72]. Up to now, coherent scattering has been mostly performed using laser sources and thus with visible light. Therefore most of the techniques employed for coherent X-ray scattering are modifications of visible-light techniques. With the availability of third-generation synchrotron sources, experiments with partially coherent X-rays become increasingly common. For example, a number of established laser techniques such as holography [21], photon correlation spectroscopy [15, 54, 58, 84, 89] or phase contrast imaging [60] are now available using X-rays, making it possible to investigate materials on smaller length scales.

The main focus of this thesis is the special application of XPCS to the study of surface dynamics. Since XPCS is still a very new technique, not all effects and measurement artifacts are commonly taken into account during data analysis. One important difference to light scattering are the comparatively small coherence lengths, which lead to a reduced resolution in reciprocal space. Especially neglecting the effects of finite experimental resolution can yield misleading results, making it imperative to implement a standard procedure to take them into account.

For example, in the case of XPCS the limited experimental resolution modifies the results of a measurement significantly. The measured dynamic structure factor of the sample is broadened and shifted, which could be falsely interpreted as a modified surface tension combined with a drastically increased viscosity [30]. One main aspect of this thesis therefore was the study of XPCS resolution effects and the implementation of a simplified convolution

formalism which makes it possible to take the finite experimental resolution into consideration in a practical way.

For this purpose, XPCS measurements were performed on liquid surfaces. Hexane, water and ethanol were used as samples. The fluid properties of these liquids are well-known, which means they provide suitable references for the experiments. The emphasis was therefore not on the discovery of "new physics" concerning the sample materials. They present rather some very well-known substances that are easy to control and to obtain, making it easier to reproduce results. The actual goal of the experiments is to further the understanding of the characteristics of surface-XPCS measurements. Until now, the results of XPCS measurements are usually interpreted analogous to dynamic light scattering data (e.g. [74]), which is an apparent oversimplification as will be shown by the comparison of experimental data to the predictions of the hitherto used formalism.

A new approach to take the effects of finite resolution in XPCS into account will be discussed. The comparison between the calculated correlation functions and the measured results provides information on the experimental resolution. This information can then be used in subsequent experiments for a quantitatively-correct data analysis.

Since the samples are low-viscosity liquids, they show propagating capillary waves on the surface. A general formalism to describe the dynamic structure factor of a liquid surface based on its visco-elastic properties [34, 33] was used to verify the validity of the low-viscosity capillary waves approximation. Since this formalism is useful especially when dealing with liquids of medium viscosity, it is discussed in detail in the thesis.

During the XPCS measurements, a possible slight dependence of the experimental resolution on the sample material was observed. To get more information on this effect, Young's double-slit experiment was combined with a surface-sensitive scattering setup to analyse the coherence properties of the specularly scattered radiation. A double mirror at grazing angle was illuminated by the specular reflexion off a liquid surface. The mirror produces the same diffraction pattern as a double slit, and the visibility of the diffraction minima yields information on the coherence length of the radiation.

A standard extension to photon correlation spectroscopy using visible light is the technique of heterodyne mixing. The scattered signal is superimposed by a static reference signal, which can be produced e.g. by placing a diffraction grating in the beam in front of the sample. The measurement then takes place in the vicinity of the diffraction maxima. This variation makes it possible to directly access e.g. the height-height correlation function of a liquid surface,

as well as improve the signal-to-noise ratio by as much as one order of magnitude [36]. It is therefore a very interesting extension also for XCPS, and possibilities of implementation using X-rays are being studied.

Another aspect of the thesis was therefore the study of possibilities to implement heterodyne mixing with XPCS. One variant that will be discussed is the application to thin adsorbed alkane films. Into the silicon substrate, a grating structure was etched. The idea is that the diffraction maxima from the substrate can function as reference beams as well. However, the measurements yielded the surprising result that no surface dynamics at the investigated dynamics could be measured. Instead, static speckle patterns were observed, which will be presented as well.

The thesis is divided into a theoretical (chapter 2) and an experimental part (chapter 3). After a short introduction into the basic principles of X-ray scattering in section 2.1, the XPCS technique will be discussed in section 2.2. Since all presented experiments deal principally with the dynamics of liquid surfaces, the corresponding visco-elastic formalism will be presented and discussed in section 2.3.

In the experimental part, the practical application of XPCS resolution calculations to surface-sensitive XPCS measurements on liquid surfaces will be presented first (section 3.1), and the experiments to determine a possible influence of the sample material on the coherence properties of the radiation in section 3.2. The chapter closes with the results of the experiments on surface-diffraction gratings and scattering measurements on adsorbed thin films in section 3.3. The thesis closes with a summary and conclusions in chapter 4.

2 Theory

In this chapter, basic principles of X-ray scattering will be discussed, followed by a short discussion of coherent scattering. In the next section, an introduction into X-ray photon correlation spectroscopy will be given, while the last section deals with the dynamics of liquid surfaces.

2.1 X-ray scattering

2.1.1 Basic principles

In the following, some general properties of X-ray scattering experiments will be presented. See also [27, 67, 92] for more details. The general principle can be described as follows: an incident wave

$$\vec{E}(\vec{r},t) \quad = \quad \vec{E}_0 \mathrm{e}^{\mathrm{i}(\omega t - \vec{k}\vec{r})} \tag{2.1}$$

hits the target and is scattered, i. e., the wave vector $\vec{k}$ with $|\vec{k}| = \frac{\omega}{c} = \frac{2\pi}{\lambda}$ and possibly the amplitude $|\vec{E}_0|$ is changed. λ denotes the wave length, and c the speed of light. In the following, we will consider the elastic case only, meaning that the frequency ω is constant.

Consider the scattered wave

$$\vec{E}'(\vec{r},t) \quad = \quad \int \mathrm{d}\Omega \, \vec{E}_0'(\Omega) \, \mathrm{e}^{\mathrm{i}(\omega t - \vec{k}'(\Omega)\vec{r})} \tag{2.2}$$

with $|\vec{k}'| = |\vec{k}|$ and $\mathrm{d}\Omega = \mathrm{d}\phi \mathrm{d}\theta \sin\theta$, where ϕ and θ are spherical coordinates. It is assumed here that for a linearly polarised incident wave the scattered wave is again linearly polarised. This is not true in the general case, as the scattering material can change the polarisation state of the radiation. In general $\vec{E}_0'$ depends on $\vec{k}$ and $\vec{k}'$. In most cases, this dependence is actually on the wave vector transfer $\vec{q} := \vec{k}' - \vec{k}$, which in turn is a function of Ω.

Kinematic approximation

In the so-called kinematic approximation, only single-scattering events are taken into account. In this limit, the scattering function $S(\vec{q})$ is given by [80, 92]

$$S(\vec{q}) = \int\int \rho(\vec{r})\rho(\vec{r}\,')e^{i\vec{q}(\vec{r}\,'-\vec{r})}\,d\vec{r}\,d\vec{r}\,' \tag{2.3}$$

with $\vec{r}$ and $\vec{r}\,'$ being two independent spatial coordinates and $\vec{q}$ the wave vector transfer or scattering vector as defined before. $\rho(\vec{r})$ denotes the electron density. The scattering function is proportional to the differential cross-section $d\sigma/d\Omega$ and therefore to the scattered intensity [80, 92]:

$$\frac{d\sigma}{d\Omega} = P_1 r_e^2 S(\vec{q}), \tag{2.4}$$

with the Lorentz polarisation factor P_1 and the classical electron radius of the electron

$$r_e = \frac{e^2}{4\pi\epsilon_0 mc^2}. \tag{2.5}$$

Equation (2.3) does not include any resolution terms concerning the wave vector $\vec{q}$, i.e. the incident radiation is assumed to be completely coherent. In this case, $S(\vec{q})$ usually shows very sharp and seemingly random fluctuations, so-called speckles, which depend on the actual scattering volume, i.e. the exact position of the sample in the beam (see e.g. figure 2.1). This approximation is only valid if the scattering volume is smaller than the so-called coherence volume of the radiation.

If the scattering volume is larger than the coherence volume, the contributions of several coherence volumes have to be added, corresponding to different sample positions. The result of this so-called ensemble average is usually a smooth scattering function containing information on the average statistical structure of the sample. More details, as well as a simplified definition and geometric interpretation of the coherence volume will be given in section 2.1.3.

In the incoherent limit, i.e. if the coherence volume is very small compared to the scattering volume, $S(\vec{q})$ can be calculated by convolution with a resolution function, $\tilde{R}(\vec{q})$. Therefore the incoherent case can be described by considering the average scattered signal of several independent beams with different wave vectors. This is especially important when considering the off-specular scattering from an inhomogeneous sample (section 2.1.2).

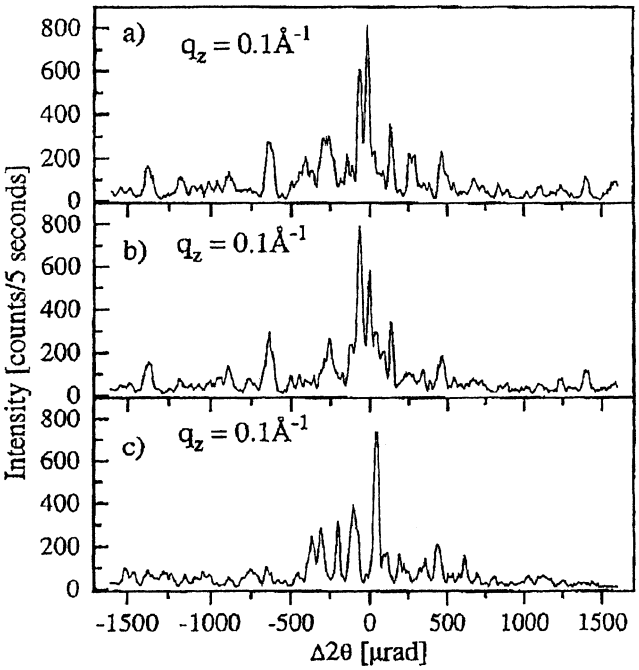

Figure 2.1: Speckle patterns from a Si(111) wafer, measured at the National Synchrotron Light Source (NSLS). $\Delta 2\theta$ denotes the deviation from the specular position (in-plane scan). Images a), b), and c) show scans on different spots of the sample. Image taken from [49].

2.1.2 Off-specular scattering

When a relatively smooth surface is illuminated by X-rays at a shallow angle, part of the radiation is transmitted into the sample, and part is reflected specularly. Since in reflectivity experiments the wave vector transfer is perpendicular to the surface, the analysis of the angle-dependent X-ray reflectivity (see appendix A.1) yields information that is laterally averaged over the illuminated area of the sample. The result is a mean electron density profile that only depends on the direction z perpendicular to the surface.

Of course, radiation is also scattered in off-specular directions. By measuring this diffusely scattered intensity, information on the lateral structure of the sample surface can be obtained. In particular, one can probe lateral correlation lengths in the (x, y) plane.

The scattering function [80]

$$S(\vec{q}) = \frac{\mathrm{e}^{-q_z^2\sigma^2}}{q_z^2} \int \mathrm{e}^{q_z^2 C_{zz}(\vec{r})} \mathrm{e}^{-\mathrm{i}\vec{q}\vec{r}}\, \mathrm{d}^2 r \tag{2.6}$$

can often be separated into a specular and a diffuse part

$$S(\vec{q}) = S_{\text{spec}}(\vec{q}) + S_{\text{diff}}(\vec{q}) \tag{2.7}$$

with the specular and diffuse parts given by

$$S_{\text{spec}}(\vec{q}) = \frac{\mathrm{e}^{-q_z^2\sigma^2}}{q_z^2}\int_A \mathrm{e}^{-\mathrm{i}\vec{q}\vec{r}}\,\mathrm{d}^2r \tag{2.8}$$

$$\text{and } S_{\text{diff}}(\vec{q}) = \frac{\mathrm{e}^{-q_z^2\sigma^2}}{q_z^2}\int_A \left[\mathrm{e}^{q_z^2 C_{zz}(\vec{r})} - 1\right]\mathrm{e}^{-\mathrm{i}\vec{q}\vec{r}}\,\mathrm{d}^2r. \tag{2.9}$$

The diffuse scattering contains information on the lateral structure of the sample through the height-height correlation function of the surface

$$C_{zz}(\vec{r}\,' - \vec{r}) = \int \mathrm{d}^2q\,\left\langle|\tilde{h}(\vec{q})|^2\right\rangle_t \mathrm{e}^{\mathrm{i}\vec{q}\cdot(\vec{r}\,'-\vec{r})}. \tag{2.10}$$

As can be seen in (2.10), the height-height correlation function is the Fourier transform of the mean spectral power density $\left\langle|\tilde{h}(\vec{q})|^2\right\rangle_t$ of the surface.

For example in the case of a surface covered by capillary waves, the height-height correlation function of the surface can be approximated for large $\vec{r}$ as [27, 92]

$$C_{zz}(|\vec{r}|) \approx -\frac{k_BT}{2\pi\gamma}\left[\gamma_E + \ln\left(\frac{\sqrt{g\rho_m/\gamma}\,|\vec{r}|}{2}\right)\right] \tag{2.11}$$

with the Euler constant γ_E, the liquid density ρ_m and the surface tension γ. Since this approximation is invalid for small $\vec{r}$, the integral in (2.10) has to be truncated by a cut-off function [27].

Using (2.11) in (2.10), one gets [27, 80]

$$S(\vec{q}) = \frac{2\pi}{q_z^2}\frac{\mathrm{e}^{-q_z^2\sigma_{\text{eff}}^2}}{\Delta q^2}\Gamma[1-\eta/2]\,{}_1F_1[1-\eta/2;1;-q^2/2\Delta q^2] \tag{2.12}$$

with

$$\eta = q_z^2 B/2 \tag{2.13}$$

$$B = \frac{k_BT}{\pi\gamma} \tag{2.14}$$

$$\sigma_{\text{eff}}^2 = \sigma^2 + \frac{1}{2}B\gamma_E - \frac{1}{2}B\ln\left(\frac{\sqrt{2}\,\Delta q}{\sqrt{g\rho_m/\gamma}}\right). \tag{2.15}$$

Δq denotes the q resolution, the parameter σ_{eff} describes an effective roughness including experimental resolution effects and ${}_1F_1(i;k;x)$ denotes the Kummer function[1]. A more thorough and general presentation of the scattering function of liquids is given e.g. by [27].

If q_z is held constant, and far from the (pseudo) specular peak, the logarithmic correlation function leads to the scattering function showing a characteristic power law

$$S_{\text{liquid}}(q_{||}) \propto q_{||}^{\eta(q_z)-2} \tag{2.16}$$

$$\text{with } \eta(q_z) = \frac{B}{2}q_z^2. \tag{2.17}$$

If $\eta(q_z) \ll 1$, the measured scattering function can therefore approximately be described by a $q_{||}^{-2}$ behaviour.

Many solid surfaces on the other hand show locally a fractal, self-affine behaviour in the sense that on small length scales, they can be very well described by a height-height correlation function of the following form [85]:

$$C_{\text{aff}}(R) = \sigma^2\left[1-\left(\frac{R}{\xi}\right)^{2h}\right]. \tag{2.18}$$

ξ is a characteristic length scale in the surface, and $0 < h < 1$ denotes the Hurst parameter. Small values of h correspond to very jagged surfaces, while $h \to 1$ yields a smoother behaviour.

On longer length scales, a solid surface looks smooth, which means that the autocorrelation function given above has to be modified. Sinha et al. have proposed the following form [80]:

$$C_{\text{solid}}(R) = \sigma^2 \mathrm{e}^{-(R/\xi)^{2h}}. \tag{2.19}$$

This model ensures a smooth surface (with a mean roughness σ) on large length scales, while the self-affine behaviour on small length scales is preserved. Assuming that the surface shows dominantly self-affine behaviour on the observed length scale, the scattering function can be approximated as [31, 80]

$$S(q_{||}) \approx \frac{2\pi\sigma^2\xi^2}{(\xi^2 q_{||}^2 + \sigma^4 q_z^4)^{3/2}}, \tag{2.20}$$

[1] Since there are several functions called "Kummer functions" in the literature: the one meant here is also known as the 'confluent hypergeometric function of the first kind' [2].

assuming a Hurst parameter $h = 1/2$. For $\xi^2 q_{||}^2 \gg \sigma^4 q_z^4$, the scattering function therefore shows a q^{-3} behaviour. This has been observed e.g. on dewetting polymer surfaces [93].

2.1.3 Coherent scattering

This section will present a short introduction into the concept of optical coherence. After a simplified, geometric interpretation, the principles of a statistical description based on the so-called mutual coherence function of the radiation will be described.

In the previous sections, the effects of finite beam divergence, energy spread etc. have been considered by means of convoluting the scattering function $S(\vec{q})$ with an experimental resolution function $\tilde{R}(\vec{q})$. This treatment is only valid if the illumination is incoherent, and if the conditions of Fraunhofer scattering are met. The latter essentially means that the distances between source, sample and detector are large compared to the quantity a^2/λ, where a^2 denotes the scattering area transverse to the beam (as e.g. defined by a pinhole). This is also called the far-field diffraction limit, and is not necessarily satisfied in X-ray scattering experiments. If the far-field approximation is invalid, the full Fresnel formalism has to be used [8, 56]. However, Fresnel diffraction will not be discussed here.

Coherence lengths

The term "coherent illumination" will be used to describe the idealised case of illumination by one single incident electromagnetic wave. In reality, perfect coherence of light can usually not be achieved, since every light source has both a finite source size and energy spread. The result is that the sample is not illuminated by a single wave, but by many slightly different ones.

Each scattered wave produces a diffraction pattern, which is detected in the experiment. If the waves are very similar, the patterns will be almost identical, and assuming coherent illumination is a valid approximation. Whether this is the case depends on the ratio of the scattering volume to the so-called coherence volume. The former is essentially determined by the sample size and e.g. beam-defining apertures, while the latter describes the coherence of the incident radiation in a quantitative way.

To define the coherence volume, usually two quantities are used which denote the maximal size of the scattering volume in order to show a mostly coherent diffraction pattern:

1. The *temporal coherence* or coherence time describes the maximal temporal distance between two points of the scattering volume in order to produce a coherent scattering

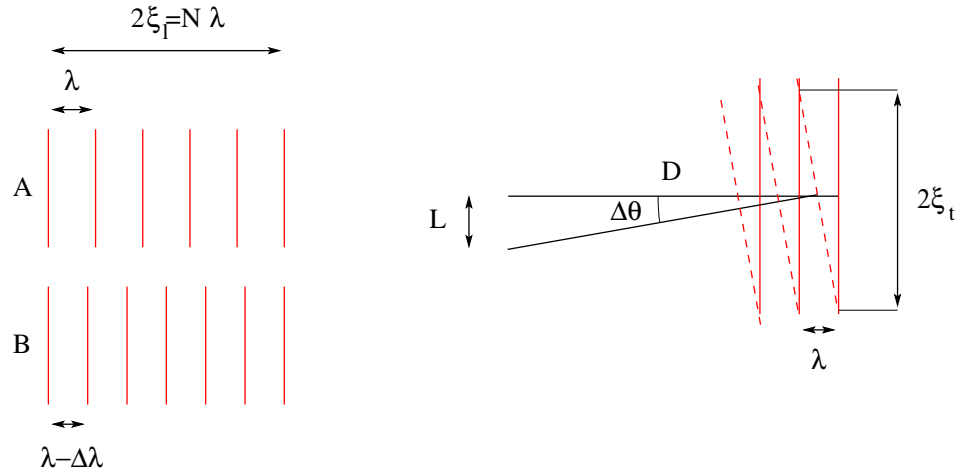

(a) Temporal coherence (b) Spatial coherence

Figure 2.2: Schematical representation of coherence properties. (a) Two plane waves are propagating in the same direction, with slightly different wave lengths. After having travelled a distance equal to the longitudinal coherence length ξ_l, the two waves are completely out of phase. (b) Two plane waves of identical wave length are emitted from opposing ends of a finite-sized source with the size L, positioned at a distance D from the sample. At the sample position, a distance ξ_t perpendicular to the radiation again causes the waves to be out of phase. Image taken from [5] and modified.

pattern. Using the speed of light in vacuum, one can also calculate the length of the corresponding flight path, yielding the longitudinal coherence length.

2. The *spatial coherence* or transverse coherence length of the radiation is the maximal (spatial) distance between two points in the scattering volume, which cannot be exceeded if a mostly coherent diffraction pattern should be observed.

If many scatterers contributing to the scattered signal are located at a distance significantly larger than the coherence length, the averaging process during detection sums over a large number of different individual diffraction patterns, smearing them out. The result is a so-called diffuse pattern, which depends only on the mean structure of the sample. This is called incoherent scattering, and can be expressed in reciprocal space by convolution with a resolution function as mentioned above. While diffuse scattering does yield information e.g. on the lateral structure of a rough surface, this information is averaged over the whole interaction volume.

Figure 2.2 shows schematical representations of the two kinds of coherence. In the following, first temporal and then the spatial coherence will be considered.

The temporal coherence is a function of the monochromaticity of the radiation. Monochromatic light shows a larger coherence time than e.g. white light, which shows virtually no longitudinal coherence. Consider a source emitting photons at a mean wave length λ, with a standard deviation given by $\Delta\lambda$. Then one can define the longitudinal coherence length as the flight distance it takes two plane waves with wave length difference $\Delta\lambda$ to be completely out of phase, i. e., have a phase difference of 180° [5].

After N wave lengths, the two waves are in phase again (see fig. 2.2(a)); we define this as twice the coherence length ξ_l:

$$\begin{aligned} 2\xi_l = N\lambda &= (N+1)(\lambda - \Delta\lambda) && (2.21)\\ \Rightarrow (N+1)\Delta\lambda &= \lambda \\ \Rightarrow \lambda/\Delta\lambda &\approx N \\ \Rightarrow \xi_l &= \frac{\lambda^2}{2\Delta\lambda} && (2.22) \end{aligned}$$

For a white (i. e., polychromatic) source, $\Delta\lambda \to \infty$ and thus $\xi_l \to 0$ as expected.

The spatial coherence or transverse coherence length is a function of the size of the source. Thus, even white light can be spatially coherent [46]. However, e.g. a light bulb is a large source, showing little spatial coherence. On the other hand, a very small aperture (thus approximating a point source) can increase the spatial coherence significantly. In fact, this is essentially the same technique that is employed to produce partially coherent X-rays, although here the source is usually an insertion device inside a synchrotron facility, and the source size is a function of machine parameters.

Consider a finite-sized source of diameter L, in distance D from the sample. Then the standard deviation of the radiation angle is $\Delta\theta \approx L/D$. At the sample position, one has to traverse the distance ξ_t for two waves with an angle difference $\Delta\theta$ to be out of phase (see figure 2.2(b)). Here one gets

$$\begin{aligned} \frac{\lambda}{2\xi_t} &= \tan(\Delta\theta) = \frac{L}{D} && (2.23)\\ \Rightarrow \xi_t &= \frac{\lambda D}{2L}. && (2.24) \end{aligned}$$

The transverse coherence length is therefore a function of the ratio D/L. This is important to note, as it has a strong influence on the design of e.g. beamlines and end stations at synchrotron facilities. One important point in this case is to choose a sufficiently large

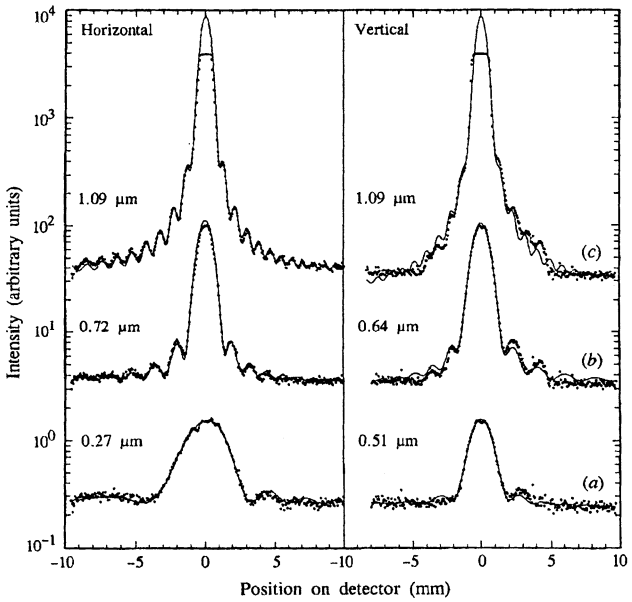

Figure 2.3: Fraunhofer diffraction from a pinhole, measured at the ESRF beamline ID3. Shown are horizontal and vertical traces through the Fraunhofer patterns from square slits of different dimensions. Image taken from [94].

distance between the source and the experimental station. For example, at the European Synchrotron Radiation Facility (ESRF) [22] or at the Advanced Photon Source (APS) [3] distances of $>$ 40m are common. Another possibility to enhance the ratio D/L is to reduce the source size.

In the following, example values for the longitudinal and transverse coherence lengths at currently available experimental stations shall be given, namely for the experimental station ID10A/C of the "Troïka" beamline (ESRF), where most of the measurements presented in this thesis took place. Here the band width of the radiation after the monochromator is $\Delta\lambda/\lambda \sim 10^{-4}$, leading to a longitudinal coherence length $\xi_l \approx 1\mu$m (at $\lambda = 1.54$Å). The transverse coherence length at the ID10 is about one order of magnitude larger ($\xi_t \sim 10\mu$m). The coherence lengths that are achieved by modern synchrotron sources are sufficient to enable several coherent scattering techniques. As an example for coherence in hard X-rays, figure 2.3 shows Fraunhofer diffraction from a pinhole measured at the beamline ID3 (ESRF).

Modern sources usually use undulators as insertion devices instead of wigglers. In addition to a reduced virtual source size, an undulator shows well-defined intensity maxima at certain energies, enhancing both the longitudinal coherence and the flux at those energies. Usually several parameters are combined into one quantity, the so-called spectral brilliance which describes the photon flux per area, per solid angle and per wave length interval of 0.1%.

To describe the radiation properties at the sample, the brilliance is often defined in a slightly different way, viz.

$$B_m = \frac{F}{(\Delta\alpha_y \Delta\alpha_z)(a_y a_z)(\Delta\lambda/\lambda)}, \tag{2.25}$$

where F denotes the number of incident photons per second, $\Delta\alpha_{y,z}$ the horizontal and vertical beam divergence, $a_y a_z$ the illuminated area and $\Delta\lambda/\lambda$ the band width.

The spatially coherent flux at the sample position is then given by [88]

$$F_c = \frac{(\lambda/2)^2}{(\Delta\alpha_y \Delta\alpha_z)(a_y a_z)} F \tag{2.26}$$

$$\Rightarrow F_c = \frac{\Delta\lambda}{\lambda} B_m \cdot \left(\frac{\lambda}{2}\right)^2, \tag{2.27}$$

which means that the brilliance is a main parameter for increasing the coherent flux. The band width $\Delta\lambda/\lambda$ is a function of the monochromator and is usually of the order of 10^{-4}.

Considering the coherence time

$$t_c = \xi_l/c = \frac{\lambda^2}{2c\Delta\lambda}, \tag{2.28}$$

one can calculate the number of photons per coherence volume as [47]

$$\begin{aligned} \delta_D &= F_c \cdot t_c \\ &= \frac{B_m}{c} \cdot \left(\frac{\lambda}{2}\right)^3. \end{aligned} \tag{2.29}$$

δ_D is also called the degeneracy parameter, and is proportional to λ^3.

If one compares e.g. radiation of 500Å (VUV) to hard X-rays of 1.5Å, the λ^2 dependence of F_c yields a factor of five orders of magnitude. If one considers the degeneracy parameter, the difference is even more than seven orders of magnitude. Scattering experiments with coherent radiation are therefore generally much easier to perform at lower energies and become increasingly challenging with decreasing wave length.

Partial coherence

If one considers coherent scattering, often the idealised case of complete coherence is assumed. It is usually also assumed that the Fraunhofer limit is satisfied and a plane-wave

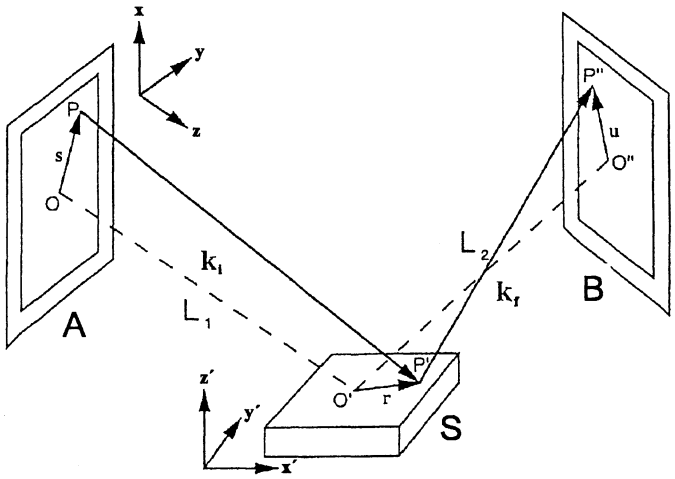

Figure 2.4: Schematic representation of the scattering geometry. The directions (x, y, z) represent the laboratory system, while (x', y', z') denote sample-fixed coordinates. Also shown are two example traces $P - P' - P''$ and $O - O' - O''$ originating from different positions in the aperture A. B marks the detector aperture. Image taken from [92].

approximation is valid. In the case of laser illumination, this assumption is often justified, since the Fraunhofer scattering approximation is usually valid and lasers can provide very large coherence lengths.

However, this is an oversimplification in the case of X-rays. Here the coherence lengths are usually comparable to or even smaller than the illuminated sample size. Furthermore one can not necessarily assume that the Fraunhofer limit is satisfied. The simple, geometric interpretation of coherence given in the previous section is still useful, but it is not sufficient. A common way to describe the propagation of coherence properties in a quantitative way is provided by the Gaussian Schell-model [56], which will not be discussed here in detail. However, it is necessary to take into account the effects of partial coherence if one wants to get quantitative results from coherent X-ray experiments. For example, in the case of X-ray photon correlation spectroscopy (XPCS), very recent calculations yield that partial coherence results in a reduced resolution in q-space [27, 30]. Those results will be discussed in more detail in section 2.2.

Starting point for the calculation of the wave propagation is the last aperture A before it hits the sample (see also figure 2.4). Let the electric field $\vec{E}(\vec{s}, t)$ at an arbitrary position $\vec{s}$ in the aperture be given as

$$\vec{E}(\vec{s}, t) = \vec{A}(\vec{s}, t)\mathrm{e}^{-\mathrm{i}\omega t} \tag{2.30}$$

with the average frequency $\bar{\omega}$ of the radiation, and the characteristic time scale of $\vec{A}(\vec{s},t)$ be $\gg \bar{\omega}^{-1}$, i.e. the amplitude fluctuations due to the finite monochromaticity of the beam can be regarded as a slow beat. The mutual coherence function (MCF) of the radiation can then be defined by [81, 92]

$$\Gamma(\vec{s},\vec{s}',\tau) \quad = \quad \left\langle \vec{A}(\vec{s},t)\vec{A}^*(\vec{s}',t+\tau)\right\rangle_t . \tag{2.31}$$

$\Gamma(\vec{s},\vec{s}',\tau)$ describes the correlation of the radiation at a time difference τ and two different positions $\vec{s}, \vec{s}'$ in the aperture, and is maximal for $\vec{s}=\vec{s}'$ and $\tau = 0$.

Now the following ansatz is done [8, 61, 62, 56]:

$$\Gamma(\vec{s},\vec{s}',\tau) \quad = \quad \Psi(\vec{s})\Psi^*(\vec{s}')g(\vec{s}-\vec{s}')F(\tau)\frac{I}{A} \tag{2.32}$$

with the amplitude factor $\Psi(\vec{s})$, the coherence factor $g(\vec{s}-\vec{s}')$, the total intensity I of the beam and the aperture area A. This representation is called the Schell form of the MCF. The normalisation is such that $g(0)=1$, $F(0)=1$ and $\int |\Psi|^2 \, \mathrm{d}A = A$, with

$$\frac{\mathrm{d}I}{\mathrm{d}A}(\vec{s}) \quad = \quad \Gamma(\vec{s},\vec{s},0) = |\Psi(\vec{s})|^2 \frac{I}{A}. \tag{2.33}$$

$|\Psi(\vec{s})|^2$ therefore describes the flux density of the radiation at the position $\vec{s}$ in the aperture. Often $g(\vec{r})$ is assumed to be of a Gaussian form:

$$g(\vec{r}) \quad \propto \quad \mathrm{e}^{-\frac{1}{2}\left[\frac{x^2}{\xi_x^2}+\frac{y^2}{2\xi_y^2}\right]}, \tag{2.34}$$

where ξ_x and ξ_y play the role of transverse coherence lengths. Commonly the amplitude distribution $\Psi(\vec{s})$ is also assumed to be Gaussian. This special approximation is usually called the Gaussian Schell model.

The function $F(\tau)$ is a temporal autocorrelation function which approaches unity for $\tau \to 0$ and zero for $\tau \to \infty$. The ansatz used in (2.32) yields that $F(\tau)$ is a simple exponential

$$F(\tau) \quad = \quad \mathrm{e}^{-\tau/\eta} \tag{2.35}$$

with the characteristic decay time η. This value can be interpreted as a coherence time with the corresponding longitudinal coherence length $c\eta = \xi_l$.

Using the kinematic approximation, one can calculate the intensity in a detector behind the second aperture B to be [81, 92]

$$I(\vec{q}) = \frac{r_e^2 \bar{\omega}}{2\pi\lambda^2} \cdot \frac{1}{L_1^2 L_2^2} \cdot \frac{I}{A} S(\vec{q}) \tag{2.36}$$

with the scattering function

$$S(\vec{q}) = \frac{q\xi_l}{k_{L_2}^4 c} \int \frac{1}{1 + (k\xi_l/q)^2 (q-Q)^2} \left(\int_B \hat{S}_Q(\vec{q} + k_{L_2}^2 \vec{u}) \, \mathrm{d}\vec{u} \right) \frac{\mathrm{d}Q}{Q^2}, \tag{2.37}$$

where k denotes the mean wave vector of the incident radiation, $Q = q(1 + \frac{\delta\lambda}{\lambda}) = q(1 + \lambda/(2\xi_l))$ and $k_{L_2} = \sqrt{k/L_2}$. $L_{1,2}$ denote the distances between the aperture A and the sample and between the sample and the detector aperture B, respectively. The $\vec{u}$ integral is taken over the area of the detector area B.

Therefore the detected intensity is given by the function $\hat{S}_Q$ convoluted with a Lorentzian resolution function which describes the longitudinal coherence. It should be noted that the coherence lengths are projected into the sample plane. For example, $\xi_l' = \xi_l \cdot k/q$ is the effective longitudinal coherence length on the sample, and $\xi_l' \gg \xi_l$ for small scattering vectors ($q \ll k$).

The function $\hat{S}_Q$ is given by

$$\hat{S}_Q(\vec{K}) = \iint \rho_F(\vec{r}) \rho_F^*(\vec{r}\,') R(\vec{r}\,', \vec{r}) \exp\left[\mathrm{i}(Q/q)\vec{K} \cdot (\vec{r}\,' - \vec{r}) \right] \mathrm{d}\vec{r}\,' \, \mathrm{d}\vec{r} \tag{2.38}$$

with

$$\begin{aligned} R(\vec{r}\,', \vec{r}) = & \iint \Psi(\vec{s}) \Psi^*(\vec{s}\,') g(\vec{s} - \vec{s}\,') \exp\left[\mathrm{i}(Q/q) k_{L_1}^2 (s^2 - s'^2)/2 \right] \\ & \cdot \exp\left[\mathrm{i}(Q/q) k_{L_1}^2 (\vec{s}\,'\vec{r}\,' - \vec{s}\vec{r}) \right] \mathrm{d}\vec{s} \, \mathrm{d}\vec{s}\,'. \end{aligned} \tag{2.39}$$

In the incoherent case ($\xi_{x,y} \to 0$), the coherence factor is $g(\vec{s} - \vec{s}\,') = \delta(\vec{s} - \vec{s}\,')$. In this case, $R(\vec{r}\,', \vec{r})$ is a function purely of the distance $\vec{r}\,' - \vec{r}$, namely the Fourier transform of $|\Psi|^2$. If $|\Psi|$ is assumed to be of Gaussian shape, equation (2.39) therefore is a Gaussian-shaped resolution function that only depends on $\vec{r}\,' - \vec{r}$. The result is equivalent to the conventional

result obtained by convolution with a finite resolution function, if one assumes that ρ_F is the electron density. Actually, ρ_F is the so-called Fresnel electron density

$$\rho_F(\vec{r}) \quad = \quad \rho(\vec{r}) \exp\left[\mathrm{i}\frac{Q}{2q}\left(k_{L_1}^2 r_{\perp,1}^2 + k_{L_1}^2 r_{\perp,2}^2\right)\right], \tag{2.40}$$

where $r_{\perp,1}$ and $r_{\perp,1}$ denote the components of $\vec{r}$ perpendicular to $\vec{k}_{i,f}$. ρ_F reduces to the electron density for large $L_{1,2}$ ($k_{L_{1,2}} \to 0$), i.e. in the Fraunhofer scattering case.

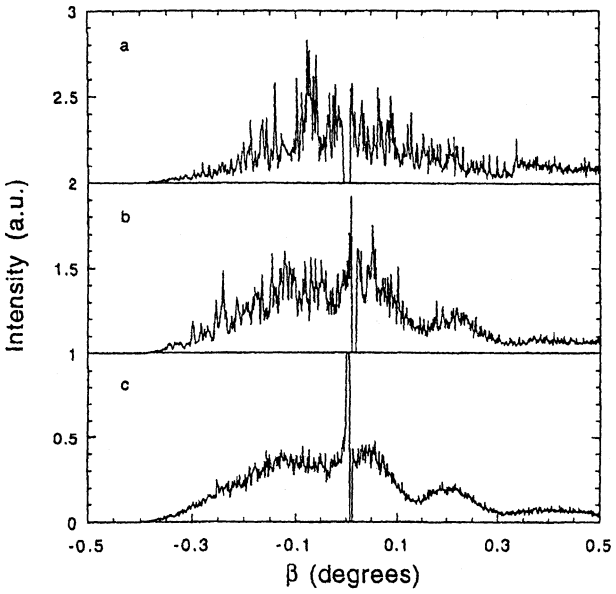

Figure 2.5: Speckle patterns from a diblock copolymer thin film (PS and PMMA, coated with 200Å Au layer). $\alpha_i = 0.4°$, and β is the deviation from the specular position. The images a, b and c correspond to different collimating pinhole sizes (5, 12 and 60μm). Figure taken from [12].

Figure 2.5 shows an experimental example for the effects of partial coherence on the measured intensity. The three images depict speckle patterns measured using different pinhole sizes. A larger pinhole size of course yields a larger scattering volume. If the latter becomes large compared to the coherence volume, the measurement yields a result that becomes increasingly similar to that of an experiment using incoherent radiation. If one increases the relative size of the coherence volume (e.g. by decreasing the pinhole diameter), the result becomes more and more speckled.

Until now, only static samples were considered. If the sample changes shape during the measurement time, the speckle pattern will change, too. This allows for in-situ measurement of sample dynamics. The technique is usually referred to as "X-ray photon correlation spectroscopy" (XPCS) and is a direct adaptation of dynamic light scattering. Chapter 2.2 will

give an introduction into surface-sensitive XPCS, since the technique was used in many of the presented experiments in this thesis.

2.2 X-ray photon correlation spectroscopy

2.2.1 Introduction

In section 2.1.3, the coherent diffraction of X-rays from static structures has been presented. The resulting speckle patterns can reveal information on the static properties of the sample. If the sample shows any dynamical behaviour, this corresponds to a temporal change of the electron density distribution.

If the electron density changes, the diffraction pattern changes accordingly (i.e., shows a different speckle pattern). The result is a fluctuating speckle pattern. The analysis of such patterns is usually known as photon correlation spectroscopy (PCS) or "dynamic light scattering" (DLS) [14]. The application to X-rays is commonly called X-ray photon correlation spectroscopy (XPCS).

The principle of photon correlation techniques is as follows: a dynamic sample is illuminated coherently. This yields a fluctuating, speckled interference pattern, which shows dynamics on time scales that are connected closely to the time scales of the sample. The scattering vector selects the observed length scale. The main difference between PCS and XPCS is (apart from the wave length) the coherence of the radiation. PCS is commonly performed using lasers, which produce almost perfectly coherent light. The coherence of X-rays on the other hand is usually quite low by comparison, even at the most powerful synchrotron sources available today. As has been discussed in section 2.1.3, the coherence lengths scale proportional to λ. The coherent flux scales $\propto \lambda^2$ (equation (2.27)), and the degeneracy factor even $\propto \lambda^3$ (equation (2.29)).

The result is that coherent measurements become increasingly difficult at shorter wave lengths. Comparing VUV radiation at 500Å to hard X-rays at 1.5Å wave length yields a difference of more than two orders of magnitude in the coherence lengths and five orders of magnitude in the coherent flux. Due to the short coherence lengths of hard X-rays one almost always has to consider the case of partially-coherent illumination, since the scattering volume is not much smaller than the coherence volume of the radiation. This affects the measurement results in subtle ways, which are still an area of investigation [27, 30].

Although the short wave length of hard X-rays increases the complexity of coherent measurements, it also is a major advantage. Since $\lambda \sim 1$Å (for hard X-rays) or even smaller, this allows in principle for the investigation of relatively slow dynamics ($10^{-2}\text{Hz} < \tau < 10^{6}\text{Hz}$) on nanometer scales. The scattering vectors necessary for this investigation are

impossible to reach using visible or even UV light. If length scales of 100Å or smaller are to be investigated, then of course the wave length of the radiation has to be shorter than this value. Using hard X-rays allows in principle to investigate structures and dynamics on length scales below 10Å. In this sense XPCS is complementary to other established techniques like Raman scattering, PCS and neutron scattering.

One application of XPCS is the combination with grazing incidence diffraction (GID): it allows for the direct measurement of surface dynamics e.g. on liquids. Since all XPCS experiments presented in this thesis have been performed in GID geometry, the following considerations will centre on this particular setup.

Grazing incidence diffraction makes use of the fact that the index of refraction is smaller than unity for hard X-rays. This means that one observes total external reflexion below a critical incident angle α_c (section A.1). At very shallow angles $\alpha_i < \alpha_c$, the penetration depth is typically limited to values below 100Å. Therefore the dynamics in the measured signal is caused by surface fluctuations, and no bulk scattering has to be considered.

2.2.2 General principles

In elastic X-ray scattering experiments, the main observable quantity is usually the spatial distribution of the scattered intensity. In the case of XPCS, one measures the temporal intensity autocorrelation function defined by

$$G_2(\vec{q}_1, \vec{q}_2, \tau) = \langle I(\vec{q}_1, t) I(\vec{q}_2, t+\tau) \rangle_t , \tag{2.41}$$

where τ denotes the time between individual intensity measurements, and $\vec{q}_{1,2}$ are scattering vectors. The correlation function is connected to the temporal spectral power density of the intensity I by means of a Fourier transform, and therefore carries the same information. However, G_2 can be calculated in-situ, i.e. during the measurement, and is therefore often chosen instead of the power spectrum. In fact, hardware-supported autocorrelation software was available at the beamline ID10A (ESRF).

The index of G_2 indicates that it is a second-order correlation function in terms of the intensity. In terms of the scattered fields it reads

$$G_2(\vec{q}_1, \vec{q}_2, \tau) = \langle E^*(\vec{q}_1, t) E(\vec{q}_1, t) E^*(\vec{q}_2, t+\tau) E(\vec{q}_2, t+\tau) \rangle_t . \tag{2.42}$$

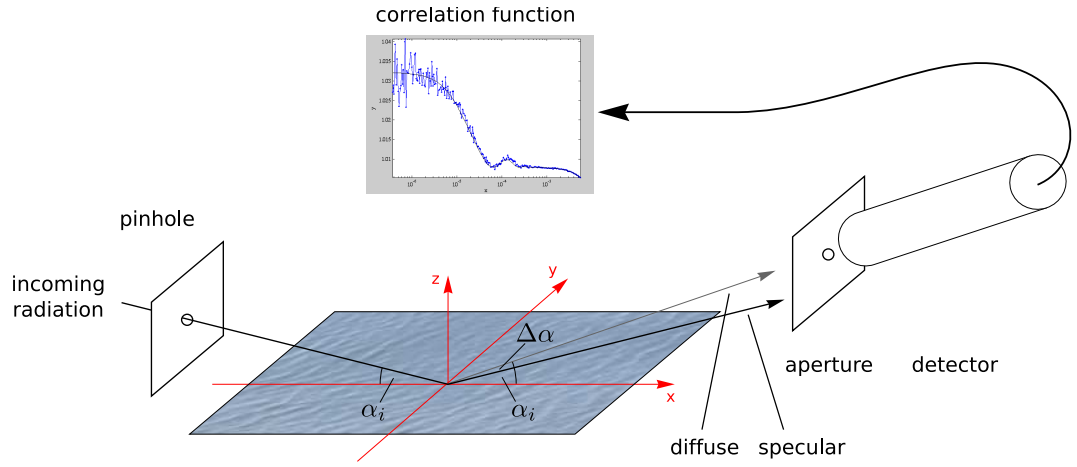

Figure 2.6: Schematics of a surface-XPCS setup. The radiation hits the sample at a shallow angle (usually $\alpha_i < \alpha_c$), limiting the penetration depth into the surface. The detector is placed at an off-specular position (difference angle $\Delta\alpha$) to introduce a lateral scattering vector component.

Assuming that the mean value of the scattered electric fields is zero and that the fields show Gaussian statistics, (2.42) transforms into [27, 56]

$$G_2(\vec{q},\tau) = \langle I(\vec{q},t)\rangle_t \langle I(\vec{q},t)\rangle_t + |G_1(\vec{q},\tau)|^2 \tag{2.43}$$

$$\Rightarrow g_2(\vec{q},\tau) = \frac{G_2(\vec{q},\tau)}{\langle I(\vec{q},t)\rangle_t^2} = 1 + \frac{|G_1(\vec{q},\tau)|^2}{\langle I(\vec{q},t)\rangle_t^2} \tag{2.44}$$

$$= 1 + |g_1(\vec{q},\tau)|^2, \tag{2.45}$$

where

$$g_1 = \frac{\langle E^*(\vec{q},t)E(\vec{q},t+\tau)\rangle_t}{\langle E(\vec{q},t)\rangle_t^2} \tag{2.46}$$

denotes the normalised correlation function of the electric fields, and perfect resolution has been implicitly assumed ($\vec{q}_1 = \vec{q}_2 = \vec{q}$). Equation (2.45) is also called the Siegert relation, and is commonly used to analyse XPCS data.

2.2.3 Surface-sensitive XPCS

Figure 2.6 shows the principle setup of a surface-sensitive XPCS setup. The radiation hits the sample surface at a shallow angle below the critical angle of total external reflexion, $\alpha_i < \alpha_c$. This limits the penetration depth, typically to a value below 100Å. The detector is placed at

an off-specular position, usually in the scattering plane that is defined by the incident and specular beam directions. In the context of this thesis, this will be referred to as in-plane geometry.

The placement of the detector at an off-specular position introduces a lateral scattering vector component

$$\vec{q}_{||} = \vec{k}\,[\cos(\alpha_i) - \cos(\alpha_i + \Delta\alpha)] \neq 0, \tag{2.47}$$

where α_i denotes the incident angle and $\Delta\alpha$ the angular offset from the specular position. This setup makes the measurement sensitive to the average lateral structure of the sample surface, with the scattering vector selecting the investigated length scale via $l = 2\pi/q_{||}$.

In order to analyse the data of surface-XPCS, one has to determine the dependence of the field correlation function $g_1(\vec{q}, \tau)$ on the surface fluctuations. In general, the field fluctuations depend on fluctuations of the electron density in the scattering material as well as fluctuations in the incoming radiation in a non-trivial way.

Under ideal conditions, neglecting effects of detector resolution and partial coherence, as well as assuming the Fraunhofer scattering case, one gets [27]

$$G_1(\vec{q}, \tau) \propto C_{zz}(q_{||}, \tau) \tag{2.48}$$

$$\Rightarrow g_1(\vec{q}, \tau) = g_1(q_{||}, \tau) = c_{zz}(q_{||}, \tau), \tag{2.49}$$

where $C_{zz}(q_{||}, \tau)$ [$c_{zz}(q_{||}, \tau)$] denotes the [normalised] height-height correlationfunction of the liquid surface, and $q_{||}$ the modulus of $\vec{q}_{||}$. The height-height correlation function is connected to the dynamic structure factor of the liquid surface by means of a Fourier transform [34]:

$$c_{zz}(k, \tau) \propto \frac{1}{2\pi} \int \mathrm{d}\omega\, \mathrm{e}^{i\omega\tau} S(k, \omega). \tag{2.50}$$

Surface-sensitive XPCS measurements therefore allow to directly probe the dynamic structure factor of a liquid sample. $\vec{q}_{||}$ selects the probed length scale and thus the in-plane wave vector $\vec{k}$ of the liquid. Therefore we choose $|\vec{k}| = q_{||}$. The correlation function is assumed to be stationary both in the temporal and in the spatial domain, i.e. it does not depend on the position on the sample and does not change with time.

For example, as seen in section 2.3, in the case of propagating capillary waves on a liquid surface (low-viscosity limit) the dynamic structure factor $S(\vec{q},\omega)$ takes the form of a Lorentzian. This means that the height-height correlation function is given by

$$c_{zz}(\vec{q},\tau) = \int \mathrm{e}^{\mathrm{i}\omega\tau} S(\vec{q},\omega) \tag{2.51}$$

$$= \cos\left[\omega_0(\vec{q})\tau\right] \mathrm{e}^{-\Gamma(\vec{q})\tau} \tag{2.52}$$

with

$$\Gamma(\vec{q}) = 2\eta|\vec{q}|^2/\rho_m \tag{2.53}$$

$$\text{and } \omega_0(\vec{q}) = |\vec{q}|^{3/2}\sqrt{\gamma/\rho_m}. \tag{2.54}$$

i.e. an exponentially-damped cosine oscillation.

Using this result and inserting it into the Siegert relation (2.45), the autocorrelation function of the scattered intensity is obtained as

$$g_{2,\text{low-visc.}} = 1 + \cos^2\left[\omega_0(\vec{q})\tau\right] \mathrm{e}^{-2\Gamma(\vec{q})\tau}. \tag{2.55}$$

This result is commonly called the homodyne correlation function, since in this detection scheme the measured intensity depends solely on the electric fields scattered by the sample.

2.2.4 Heterodyne mixing

In dynamic light scattering commonly a setup modification called heterodyne mixing is used, where the scattered fields are superimposed by a reference field with amplitude $E_{\text{ref}} \gg E_{\text{scat}}$, i.e. that is much stronger than the scattered radiation itself [14]. A possible modification of the surface-sensitive setup shown in figure 2.6 can bee seen in figure 2.7. In front of the sample, a grating is placed. This grating produces well-defined diffraction maxima at different angles, thus deflecting a part of the incident radiation. If one places the detector close to one of these diffraction maxima, the detected intensity depends on the superposition of both the scattered and reference fields.

In principle, this modification of the setup is possible with X-rays as well [29, 53]. One goal of the experiments presented in this thesis was to develop and test a heterodyne XPCS setup. However, due to the small coherence lengths in the hard X-ray regime, this setup adds considerable complexity to an experiment. The setup shown in figure 2.7 could not be used

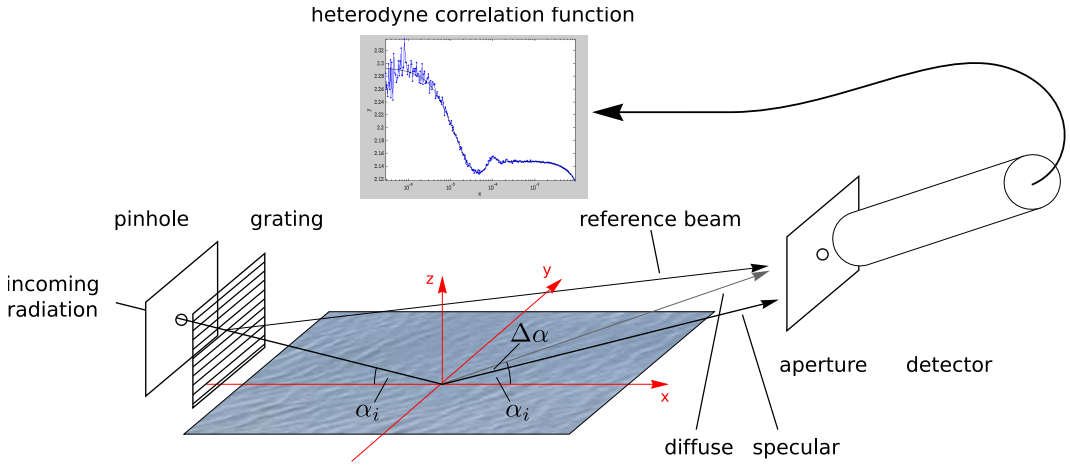

Figure 2.7: Schematics of heterodyne mixing in surface-sensitive XPCS. The setup is identical to the one shown in figure 2.6, with the addition that a diffraction grating is placed in the beam in front of the sample. The detector is placed close to a diffraction order of the grating which serves as static reference signal.

successfully yet, although first tests using transmission gratings optimised for hard X-rays [13] look promising. In the experimental part of the thesis, one example of heterodyne mixing is discussed, proving that the principle works.

In heterodyne detection mode, the calculated intensity correlation has to be modified, since now a term $\propto E_{\mathrm{ref}} \cdot E_{\mathrm{scat}}$ becomes dominant. One gets for the detected intensity and correlation function [19]

$$
\begin{aligned}
I(\vec{q},t) &= \left[E_{\mathrm{scat}}(\vec{q},t) + E_{\mathrm{ref}}(t)\right]\left[E_{\mathrm{scat}}(\vec{q},t) + E_{\mathrm{ref}}(t)\right]^{*} && (2.56)\\
G(\vec{q},\tau) &= \left\langle I(\vec{q},t) I(\vec{q},t+\tau)\right\rangle_{t} && (2.57)\\
&= \left\langle I_{\mathrm{scat}}(\vec{q}) + I_{\mathrm{ref}}\right\rangle^{2} + 2\left\langle I_{\mathrm{scat}}(\vec{q})\right\rangle\left\langle I_{\mathrm{ref}}\right\rangle g_1(\vec{q},\tau) \\
&\quad + \left\langle I_{\mathrm{scat}}(\vec{q})\right\rangle^{2}\left(g_2(\vec{q},\tau) - 1\right) && (2.58)\\
&\approx \left\langle I_{\mathrm{ref}}\right\rangle^{2} + 2\left\langle I_{\mathrm{scat}}\right\rangle\left\langle I_{\mathrm{ref}}\right\rangle g_1(\tau), && (2.59)
\end{aligned}
$$

or in the normalised form

$$
g_2(\vec{q},\tau) \approx 1 + \underbrace{2\frac{\left\langle I_{\mathrm{scat}}\right\rangle}{\left\langle I_{\mathrm{ref}}\right\rangle}}_{=:C} g_1(\vec{q},\tau). \qquad (2.60)
$$

The contrast C of the correlation function is determined by the ratio of the scattered intensity to the reference intensity, with the important property $C \to 0$ for $I_{\mathrm{ref}} \to \infty$, i.e. the contrast decreases for increasing reference intensity. However, heterodyning can still yield a gain with regard to the signal-to-noise ratio. Theoretical calculations show that the ratio can be increased by one order of magnitude under optimal conditions [36].

In the heterodyne regime, the measured intensity autocorrelation is proportional to the autocorrelation function g_1 of the scattered electric field. The example of capillary waves on a low-viscosity liquid now yields

$$g_2(\vec{q}) \quad = \quad 1 + C \cdot \cos\left[\omega_0(\vec{q})\tau\right] \mathrm{e}^{-\Gamma(\vec{q})\tau}. \tag{2.61}$$

This example is particularly interesting, since here the correlation functions of the two cases are easily distinguishable due to the clear difference between the cos and $\cos^2$ behaviour. Low-viscosity liquids showing propagating waves are therefore ideal systems for experiments on heterodyne mixing itself. In the case of overdamped waves the correlation function is a simple exponential, and the difference between the homodyne and heterodyne regime is merely a factor 2 in the damping constant.

The fact that in heterodyne detection mode the measured correlation function is directly proportional to the autocorrelation of the electric fields g_1 makes it possible to directly measure the height-height correlation function of a liquid surface. This property makes this modification very attractive, since it usually makes the analysis of the measured data less complex.

It should be stressed that in this idealised limit of complete coherence and Fraunhofer scattering, without an external reference source one always detects a homodyne correlation function. Heterodyne mixing can only occur if an external reference source is used. While systematic, external heterodyning as described here is a standard technique in the field of light scattering, the task is non-trivial in the case of X-rays, since the coherence lengths are much shorter.

However, there are cases in which intrinsically heterodyne correlation functions have been measured. If a finite experimental resolution is taken into account, it can be shown that the specular reflexion itself can act as a reference source, as will be discussed in the next section.

2.2.5 Resolution effects in surface-sensitive XPCS

In the previous sections, for the discussion of XPCS results the possible finite resolution of the scattering vector $\vec{q}$ has been neglected. This assumption is only true in the case of perfect coherence and if the Fraunhofer scattering conditions are met. In a real experiment, the coherence lengths of the incident radiation are always limited. In the case of hard X-rays, the coherence volume is not necessarily larger than the interaction volume with the sample.

Additionally, the Fraunhofer scattering regime is very difficult to achieve for X-rays. Since the pinhole is of course an aperture, the Fraunhofer approximation is only valid if the so-called Fresnel number [81]

$$F := \frac{a^2}{D\lambda} \tag{2.62}$$

(with the pinhole diameter a, the distance D to the sample and the wave length λ) is much smaller than unity, i.e. $F \ll 1$. For a typical setup using hard X-rays (e.g. 8keV), $a \approx 12 - 15\mu$m, $D \approx 0.5$m and $\lambda \approx 1.5$Å. This yields $F \approx 2$, meaning that the assumption of Fraunhofer scattering is an undue simplification.

For the correct interpretation of XPCS results, one must therefore assume a finite experimental resolution. The simple relationship (2.49) is usually invalid in the case of X-rays, i.e. the autocorrelation function of the scattered field is *not* identical to the height-height correlation function of the sample surface. Furthermore, for correct results one has to work with the Fresnel formalism. However, it is possible to calculate the result even for the Fresnel case, by taking into account a generalised resolution function in the calculation. A first thorough treatment has been done by T. Ghaderi [27], and a second by C. Gutt [30].

While the complete treatment is quite complicated and highly non-trivial, a simplified result shall be given here, which has also been used to interpret the experimental data in this thesis. This is necessary since the results of the calculation are not directly applicable to experimental data.

In this treatment, the intensity autocorrelation function is quite generally of the following form:

$$\tilde{G}_2(q_{||},\tau) \propto \left| \underbrace{R(q_{||})}_{\text{specular}} + \underbrace{\frac{k_B T}{\gamma} \int_0^\infty \mathrm{d}^2 q'_{||}\, c_{zz}(q_{||},\tau) R(q'_{||} - q_{||})}_{\text{diffuse}} \right|^2 , \tag{2.63}$$

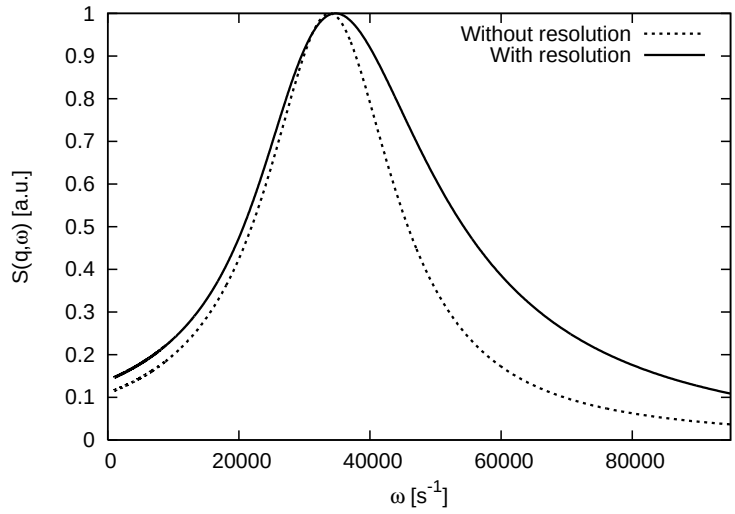

Figure 2.8: Effects of resolution on the measured dynamic structure factor $S(\vec{q},\omega)$ of capillary waves. It can be clearly seen that the effective spectrum gets broader and shifted to higher frequencies.

where k_B is the Boltzmann constant, T the temperature, γ the surface tension of the liquid and R a resolution function that is not in general accessible by experiment, but has to be left as a fit parameter. This resolution function depends on the optics of the beamline, on the scattering geometry and on the sample as well, and can therefore be only approximated to a certain degree.

As simple as this approximation is, some important points can be seen in eq. (2.63). First, the surface correlation function is convoluted with the finite resolution function R (which is equivalent to a resolution convolution of the dynamic structure factor). This yields a broadening of the spectrum as well as a possible shift of the mean frequency.

The impact of resolution on the effective dynamic structure factor is illustrated by figure 2.8. The broadening and shift of the convoluted spectrum can be clearly seen, yielding a measured correlation function that is more strongly damped and shifted towards shorter timescales.

Secondly, the first resolution term can act as a "reference term" much like in the case of systematic heterodyne mixing as discussed in the previous section. This part corresponds to the specular reflexion, while the convolution part accounts for the diffuse scattering from the surface. Under certain conditions, the specular reflexion can therefore replace the external reference beam used for heterodyne mixing. This means that the resulting correlation function can be homodyne or heterodyne, depending on the actual resolution functions of the setup. This has first been experimentally observed on water samples [29].

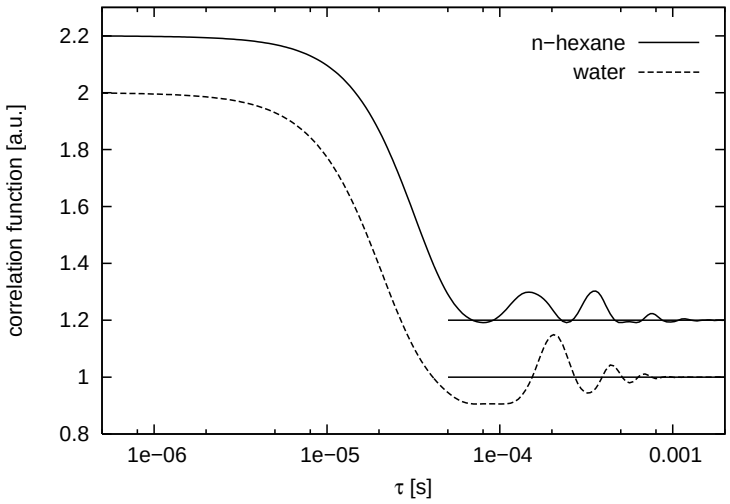

Figure 2.9: Influence of the surface tension on the measured correlation function. Calculations were done for water and n-hexane. Scattering vector was $q_x = 2.12 \cdot 10^{-6}\text{Å}^{-1}$, and resolution parameters were $\delta q_x = 1.58 \cdot 10^{-7}\text{Å}^{-1}$, $\delta q_y = 1.21 \cdot 10^{-5}\text{Å}^{-1}$. Neither function can be described as purely homodyne or heterodyne. However, the correlation function of hexane shows a more homodyne behaviour, while the water function is clearly more heterodyne.

The surface tension of the liquid also has a certain influence on the observance of heterodyne mixing, since the intensity of the diffuse scattering is proportional to $1/\gamma$. A liquid with a very low surface tension like e.g. n-hexane shows a stronger diffuse scattering than e.g. water. This can shift the ratio between the two summands of (2.63), shifting the result slightly towards the heterodyne or towards the homodyne case. This is shown in figure 2.9, which compares calculations for n-hexane and water. The only difference between the two calculations are the material parameters, most importantly the surface tension. It can be seen that the water function ($\gamma \approx 72\text{mN/m}$) is dominated by the heterodyne case, while the hexane calculation ($\gamma \approx 18\text{mN/m}$) shows an almost-homodyne result.

It should be noted that the generalised resolution function R can in theory be calculated completely if the influence of every optical element in the beamline is very well known. [27] gives examples of several different scattering setups and calculates their resolution functions. On the other hand, this approach is hardly feasible in practice, since every element of the experiment (including the sample itself) influences the optical properties of the radiation.

In this thesis, the resolution functions are therefore assumed to be of a simple, Gaussian shape and used as fit parameters. Although this is an oversimplification, this approach is still very useful, since it should be possible to determine the effective resolution of the setup to a

sufficient degree by measuring a well-known sample first. The fit result can then be used for the interpretation of the actual experimental data.

Therefore the following procedure is proposed to deal with XPCS resolution effects. First the surface dynamics of a well-known sample that shows dynamics on a time scale similar to the actual sample is measured. Then the actual measurement on the unknown sample is performed. The effective resolution broadening for the current experimental setup is determined from the reference measurements in a first data analysis step. The actual measurement data is then analysed using the now known experimental resolution.

2.3 Dynamics of liquid surfaces

A liquid-gas interface is never perfectly smooth. In fact, the surface of a liquid is always covered with microscopic fluctuations. Those fluctuations usually manifest themselves as thermally-excited waves. The excitation is provided by the Brownian motion of the liquid particles, and the dominant restoring force is the liquid's surface tension: gravity forces are negligible on a microscopic scale. Because of that, these waves are called capillary waves. Their wave lengths are usually below 1cm, depending on the sample system (see fig. 2.10).

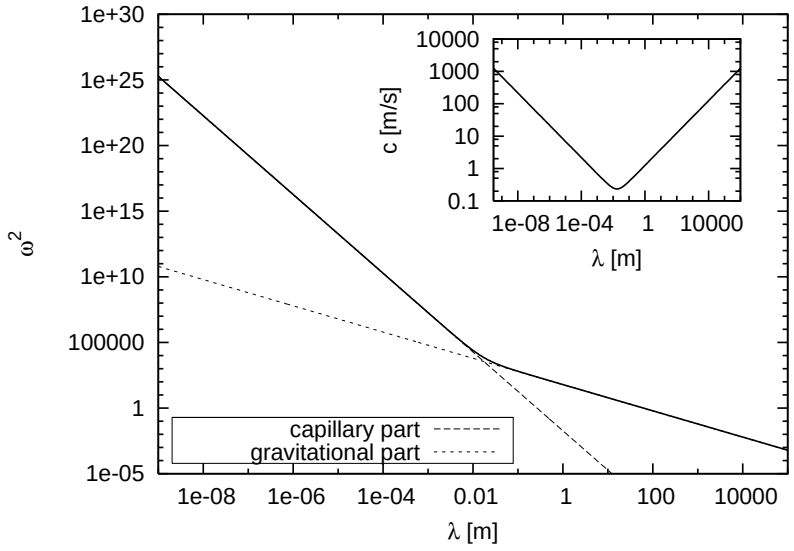

Figure 2.10: Angular and phase velocity of surface waves, depending on wave vector $\vec{k}$ (calculated for water). The two different cases (capillary- and gravity-dominated) can be clearly discerned. The capillary forces become dominant for wave lengths of about 1cm and less.

In this section, the spectral power distribution or dynamic structure factor $S(|\vec{k}|, \omega)$ of capillary waves, depending on the wave vector $|\vec{k}|$ and the frequency ω, will be discussed. The results are used for the interpretation of measurements presented later in this work.

The capillary waves model is well-established. Notable early publications include those of Lamb [41] and Levich [48]. Therefore, the two main results for capillary waves of classical hydrodynamics are presented first, namely the so-called low- and high-viscosity limit of the surface wave spectrum. The transition region between the two cases is discussed theoretically by [34] and has been subject to recent research [54]; the corresponding theoretical result and an even more general case will be presented in section 2.3.2.

2.3.1 Classical capillary waves theory

According to [48], the capillary wave spectrum of an ideal, incompressible liquid of infinite depth shows two distinct limits: the so-called low-viscosity or inelastic and the high-viscosity or elastic limit. Many liquids like water or hexane ($\eta \ll 10$mPas) are well-described by the former (at least for small $|\vec{k}|$), while e.g. glycerol is an example for the latter. In this section, the two cases will be discussed and compared.

Low-viscosity limit

Low-viscosity liquids show propagating oscillatory modes on their surface. Their behaviour is dominated by the surface tension, with the viscosity acting as a weak damping mechanism of the oscillations. Therefore, we first consider the case of an ideal liquid ($\eta = 0$). Here one gets [48]

$$x = x_0 + a e^{|\vec{k}|z_0} \cos(|\vec{k}|x_0 - \omega_0 t) \tag{2.64}$$

$$\text{and } z = z_0 + a e^{|\vec{k}|z_0} \sin(|\vec{k}|x_0 - \omega_0 t) \tag{2.65}$$

as the motion of a liquid particle, with (x_0, z_0) denoting the mean coordinates of that particle. x denotes a lateral direction, while z is the direction perpendicular to the liquid surface. Each particle in the liquid therefore moves on the circumference of a circle with the angular velocity

$$\omega_0(\vec{k}) = |\vec{k}|^{3/2}\sqrt{\gamma/\rho_m}, \tag{2.66}$$

and a radius $ae^{|\vec{k}|z_0}$, where a denotes the amplitude of the wave at the surface. The radius decreases exponentially with increasing depth ($z_0 < 0$), and ω_0 is determined by the liquid's surface tension γ and density ρ_m.

A liquid's viscosity describes the dissipation of oscillatory energy with time and can be interpreted analogous to the damping constant of a harmonic oscillator. Just as the harmonic oscillator shows two distinct limits depending on the magnitude of the damping constant (*weak* and *strong* damping), we can discern the corresponding cases for capillary waves. In the case of sufficiently low viscosity, the eigenfrequencies are expected to be very similar to those of an ideal liquid.

Introducing the kinematic dynamic viscosity $\nu = \eta/\rho_m$, and if the inequality

$$\frac{a}{2\nu|\vec{k}|^2} \gg 1 \tag{2.67}$$

holds, the oscillatory modes take the following form [48]:

$$x = x_0 + a\mathrm{e}^{|\vec{k}|z_0}\cos(|\vec{k}|x_0 - \omega t)\mathrm{e}^{-2\nu|\vec{k}|^2 t} \tag{2.68}$$

$$\text{and } z = z_0 + a\mathrm{e}^{|\vec{k}|z_0}\sin(|\vec{k}|x_0 - \omega t)\mathrm{e}^{-2\nu|\vec{k}|^2 t} \tag{2.69}$$

with $\omega \approx \omega_0$. The only modification is therefore an exponential damping with time.

From this result it is now possible to calculate the dynamic structure factor of the surface. This quantity is defined as the inverse Fourier transform of the height-height correlation function: [34]

$$S(\vec{k},\omega) = \int_{-\infty}^{\infty} \mathrm{d}t\, \mathrm{e}^{-\mathrm{i}\omega t}\left\langle z(\vec{k},t)z(-\vec{k},0)\right\rangle. \tag{2.70}$$

To ease calculations, both the height-height correlation function and the structure factor are commonly defined to be even functions of t and of ω respectively, e.g. $S(\vec{k},\omega) = S(\vec{k},-\omega)$.

Since the correlation function replicates the cosine behaviour of the surface displacement functions, the structure factor shows a distinct peak at the frequency ω_0 which takes the form of a Lorentzian [11]

$$S(\vec{k},\omega) \propto \frac{1}{\pi\Gamma_0\left[1+\left(\frac{\omega-\omega_0}{\Gamma_0}\right)^2\right]} \tag{2.71}$$

with a half-width-at-half-maximum (HWHM) given by [48]

$$\Gamma_{0,\text{low-visc.}}(\vec{k}) = 2\eta|\vec{k}|^2/\rho_m. \tag{2.72}$$

High-viscosity limit

A highly-viscous liquid is the analogon of a strongly-damped harmonic oscillator; we therefore do not expect any oscillatory behaviour, but rather a simple exponential decay. While in the low-viscosity case the viscosity only affects the temporal damping, in this case the behaviour is solely defined by the quantity γ/η, thus both parameters (surface tension *and* viscosity) play an equally important role.

We define the high-viscosity limit by the inverse of (2.67):

$$\frac{a}{2\nu|\vec{k}|^2} \ll 1. \tag{2.73}$$

In this case, we get a simple exponential decay with time, as expected:

$$x = x_0 + a\mathrm{e}^{|\vec{k}|z_0}\cos(|\vec{k}|x_0)\mathrm{e}^{-\frac{\gamma|\vec{k}|}{2\eta}t} \tag{2.74}$$

$$\text{and } z = z_0 + a\mathrm{e}^{|\vec{k}|z_0}\sin(|\vec{k}|x_0)\mathrm{e}^{-\frac{\gamma|\vec{k}|}{2\eta}t}, \tag{2.75}$$

with the damping constant [48]

$$\Gamma_{0,\text{high-visc.}}(\vec{k}) = \frac{\gamma|\vec{k}|}{2\eta}. \tag{2.76}$$

The dynamic structure factor takes again the form of a Lorentzian, but this time centered at $\omega = 0$:

$$S(\vec{k},\omega) \propto \frac{1}{\pi\Gamma_0\left[1+\left(\frac{\omega}{\Gamma_0}\right)^2\right]}. \tag{2.77}$$

It should be noted that in the presented considerations the amplitude of the waves is still a parameter. It is therefore not possible to calculate e.g. the surface roughness without further boundary conditions. In order to quantitatively compare other calculations to these results, they have to be normalised.

Using the well-known result (see e.g. [9]) that the surface roughness is given by

$$\sigma^2 = \frac{k_B T}{2\pi\gamma}\ln\left(\frac{k_{uc}}{k_{lc}}\right) \tag{2.78}$$

in conjunction with the relation [34]

$$2\pi\sigma^2 = \int_{k_{lc}}^{k_{uc}} \mathrm{d}k\, kS(k) \tag{2.79}$$

one directly gets the classical result $k_B T/(\gamma k^2) = S(k)$. If we assume a Lorentzian shape and take into account that the dynamic structure factor is an even function of ω, we have to modify equation (2.71) by the factor $\pi k_B T/(\gamma k^2)$; a similar consideration leads to a modification of equation (2.77) by $2\pi k_B T/(\gamma k^2)$.

2.3.2 Dynamics of a liquid film of arbitrary depth: viscoelastic theory

Wetting phenomena play an important role both in science and in technology. Therefore the dynamics of thin films have repeatedly been subject to scientific investigation [4, 16, 32, 64]. For the investigation of wetting phenomena, the interfacial tension and substrate interactions play a key role, which are in turn determined by the dependance of the surface free energy on the local displacement of the interface. Another important influence is the confinement, i. e. the fact that movement of the liquid molecules is hampered due to the presence of e.g. a hard wall (the substrate) in addition to the liquid-gas interface. If the film is thick enough, the presence of the substrate can be expected to have little effect, which is the limit of a liquid of "infinite" depth (discussed in the previous section). However, for sufficiently thin films, the geometric confinement gains importance.

In this section, geometric constraints for the power spectrum of capillary waves on the surface of a viscoelastic liquid of finite depth will be derived. These results represent the most general case and include the low- and high-viscosity limits for infinite depth as discussed earlier in this chapter. The calculations presented here were first done by Jäckle et al.; for a more detailed presentation, please see appendix A.2 and [33, 34].

Following linear response theory, the dynamic structure factor of the liquid surface is connected to the dynamic susceptibility $\chi_{zz}(|\vec{k}|,\omega)$ of the liquid by [33]

$$S(\vec{k},\omega) = \frac{2k_BT\,\Im(\chi_{zz}(k,\omega))}{\omega}. \tag{2.80}$$

The dynamic susceptibility $\chi_{zz}(k,\omega)$ marks the ratio of a vertical displacement u_z of the surface to an external pressure P_z. $\Im(\chi_{zz})$ denotes the imaginary part of χ_{zz}.

Solving the linearised Navier-Stokes equation

$$\frac{\partial}{\partial t}\vec{v} = -\frac{1}{\rho_m}\nabla P + \nu\Delta\vec{v}, \tag{2.81}$$

with the velocity $\vec{v}$, the pressure P and the kinematic viscosity $\nu = \eta/\rho_m$ of the liquid, using a plane waves ansatz

$$\vec{v}(\vec{r},t) = (\bar{v}_x(z)\hat{e}_x + \bar{v}_z(z)\hat{e}_z)\exp[\mathrm{i}(kx-\omega t)] \tag{2.82}$$

$$P(\vec{r},t) = \bar{P}(z)\exp[\mathrm{i}(kx-\omega t)] \tag{2.83}$$

yields

$$\bar{v}_z(z) = -\mathrm{i}\left[Ak\left(\cosh(kz)-\cosh(\kappa z)\right)+B\left(\kappa\sinh(kz)-k\sinh(\kappa z)\right)\right] \quad (2.84)$$

$$\text{and } \bar{v}_x(z) = A\left(k\sinh(kz)-\kappa\sinh(\kappa z)\right)+B\kappa\left(\cosh(kz)-\cosh(\kappa z)\right) \quad (2.85)$$

$$\text{with } \kappa = \sqrt{k^2-\mathrm{i}\omega/\nu},\ \Re(\kappa)>0 \quad (2.86)$$

as the transverse and lateral speed components, respectively.

The coefficients A and B have to be determined through boundary conditions. At the free surface ($z = h$), these are [33, 41]:

$$\left.\frac{\partial}{\partial z}v_x+\frac{\partial}{\partial x}v_z\right|_{z=h} = 0 \quad (2.87)$$

$$\text{and } \left.-P+2\eta\frac{\partial}{\partial z}v_z\right|_{z=h} = \gamma\frac{\partial^2}{\partial x^2}u_z-g\rho_m u_z+P_z \quad (2.88)$$

with the vertical surface displacement

$$u_z = \frac{\mathrm{i}}{\omega}v_z\big|_{z=h} \quad (2.89)$$

and an external force per area

$$P_z(x,t) = P_{z,0}\exp[\mathrm{i}(kx-\omega t)] \quad (2.90)$$

which acts on the surface in the z direction. g denotes the gravitational acceleration.

Evaluating the boundary conditions leads to a linear equation system

$$A_{11}A+A_{12}B = 0 \quad (2.91)$$

$$A_{21}A+A_{22}B = \frac{P_{z,0}}{\rho_m} \quad (2.92)$$

with the coefficients

$$A_{11} = 2k^2\cosh(kh)-(k^2+\kappa^2)\cosh(\kappa h) \quad (2.93)$$

$$A_{12} = 2k\kappa\sinh(kh)-(k^2+\kappa^2)\sinh(\kappa h) \quad (2.94)$$

and

$$\begin{aligned} A_{21} &= -\mathrm{i}\nu\left[(k^2+\kappa^2)\sinh(kh) - 2k\kappa\sinh(\kappa h)\right] \\ &\quad + \frac{k}{\omega}\left[\frac{\gamma k^2}{\rho_m} + g\right]\left[\cosh(kh) - \cosh(\kappa h)\right] \qquad (2.95) \\ A_{22} &= -\mathrm{i}\nu(k^2+\kappa^2)\frac{\kappa}{k}\cosh(kh) + 2i\nu k\kappa\cosh(\kappa h) \\ &\quad + \frac{1}{\omega}\left[\frac{\gamma k^2}{\rho_m} + g\right]\left[\kappa\sinh(kh) - k\sinh(\kappa h)\right]. \qquad (2.96) \end{aligned}$$

Solving this equation system and inserting the result into (2.83) and (2.84) allows to calulate the dynamic susceptibility

$$\begin{aligned} \chi_{zz}(k,\omega) &:= \frac{u_z}{P_z} \qquad (2.97) \\ &= \frac{A_{11}\left(\kappa\sinh(kh) - k\sinh(\kappa h) - A_{12}k\left(\cosh(kh) - \cosh(\kappa h)\right)\right)}{\rho_m\omega\left(A_{22}A_{11} - A_{12}A_{21}\right)}. \qquad (2.98) \end{aligned}$$

[33] discusses several limiting cases of this general formula, some of which will be presented in the following.

Substrate interaction

Up to now, we have neglected a possible interaction between substrate and liquid by van der Waals forces. In fact, in the case of very thin films, the van der Waals interaction becomes dominant and e.g., gravity effects can be neglected. Also, when calculating the roughness of a liquid film using the result (2.98), the calculated value turns out to be independent of the film thickness, which does not correctly describe the behaviour of very thin films.

[59, 73, 92] suggest modifying the boundary condition at the surface (2.88):

$$-P + 2\eta\frac{\partial}{\partial z}v_z\Big|_{z=h} = \gamma\frac{\partial^2}{\partial x^2}u_z - g\rho_m u_z + \frac{A_{\mathrm{eff}}}{2\pi h^4}u_z + P_z \qquad (2.99)$$

with the term containing the system's effective Hamaker constant A_{eff} accounting for the van der Waals attraction between liquid and substrate, assuming that the surface roughness is small compared to the film thickness. A_{eff} is assumed to be negative.

For a thin film, the Hamaker constant can be approximated by [16]

$$\begin{aligned} A_{\text{eff}} &\approx \frac{3k_BT}{4}\left(\frac{\epsilon_s-\epsilon_l}{\epsilon_s+\epsilon_l}\right)\left(\frac{\epsilon_g-\epsilon_l}{\epsilon_g+\epsilon_l}\right) \\ &\quad + \frac{3h\nu_e}{8\sqrt{2}}\frac{(n_s^2-n_l^2)(n_g^2-n_l^2)}{\sqrt{n_s^2+n_l^2}\sqrt{n_g^2+n_l^2}\left[\sqrt{n_s^2+n_l^2}+\sqrt{n_g^2+n_l^2}\right]}, \end{aligned} \tag{2.100}$$

where $\epsilon_{s,l,g}$ denote the dielectric constants of the substrate, liquid and gas, respectively. $n_{s,l,g}$ are the materials' indices of refraction. $\nu_e \approx 3\cdot 10^{15}\text{s}^{-1}$ denotes the mean absorption frequency of the three phases [16].

When repeating the calculation including this modification of the boundary conditions, the result is equivalent to a modification of the gravitational acceleration g:

$$g \;\rightarrow\; g' = g - \frac{A_{\text{eff}}}{2\pi\rho_m h^4} \tag{2.101}$$

with A_{eff} being typically of the order of -10^{-20}J. The van der Waals forces cause a faster motion of very thin films (in the range of e.g., $\sim$ 100Å or even less), as well as a reduced roughness, but can be neglected in the case of a deep liquid.

A_{eff} is itself a function of the film thickness, consisting of a static part and a part that decreases as $1/h$ for film thicknesses of more than $50-100$Å [16]. Due to these so-called retardation effects, a more appropriate estimate of the Hamaker term for mesoscopic films of a few μm thickness would be $A_{\text{eff}} \sim -10^{-21}$J or less [16]. However, for mesoscopic films the calculation yields that the influence of the van der Waals forces on the surface dynamics can be neglected completely. The influence becomes most significant for very thin films in the region $h \sim 100$Å, and the A_{eff} retardation effects are therefore not considered in the presented results.

Static susceptibility

A very important quantity is the static susceptibility

$$\chi_0(k) := \lim_{\omega\to 0}\chi_{zz}(k,\omega) \tag{2.102}$$

$$= \frac{1}{\gamma k^2 + g\rho_m - \frac{A_{\text{eff}}}{2\pi h^4}} \tag{2.103}$$

which allows e.g. to calculate the roughness of the liquid. It should be noted that the film thickness enters (2.103) only through the Hamaker term, which means that the confinement of the film alone only slows down the surface motion. The mean quadratic surface displacement (defining the roughness) is not changed. However, introducing van der Waals interaction, χ_0 becomes h-dependent. This causes the film roughness to decrease for the case of very thin films.

The total intensity of the surface wave spectrum is directly proportional to the static susceptibility [34]:

$$\begin{aligned} S(k) &= k_B T \chi_0(k) \\ &= \frac{k_B T}{\gamma} \cdot \frac{1}{k^2 + g\rho_m/\gamma - A_{\text{eff}}/(2\pi\gamma h^4)} \end{aligned} \tag{2.104}$$

This allows to calculate the mean quadratic surface displacement [34]

$$\sigma^2 = \langle u_z^2 \rangle = \iint \frac{d^2k}{(2\pi)^2} S(k) \tag{2.105}$$

$$= \frac{1}{2\pi} \int_0^{k_{uc}} k\, S(k) \tag{2.106}$$

$$= \frac{k_B T}{4\pi\gamma} \ln\left(\frac{k_{uc}^2 + g\rho_m/\gamma - A_{\text{eff}}/(2\pi\gamma h^4)}{g\rho_m/\gamma - A_{\text{eff}}/(2\pi\gamma h^4)} \right) \tag{2.107}$$

$$=: \frac{k_B T}{4\pi\gamma} \ln\left(\frac{k_{uc}^2 + k_{\text{vdW}}^2}{k_{\text{vdW}}^2} \right). \tag{2.108}$$

The upper cut-off vector k_{uc} is necessary, since the integral diverges for $k_{uc} \to \infty$. It makes sense to choose as cut-off the wave vector corresponding to the smallest length scale which is expected to show liquid behaviour. Therefore we define k_{uc} by the molecule radius r_M:

$$k_{uc} = \frac{2\pi}{2r_M} \tag{2.109}$$

In the case of e.g. hexane, r_M is ~ 3.7Å, which leads to an upper cut-off of $k_{uc} \sim 0.84\text{Å}^{-1}$. Table 2.1 lists molecule sizes of different typical sample liquids; for reference, the respective radius of gyration is also given where available. While the two values are usually similar, differences of $\sim 100\%$ can occur (e.g. water). It should be noted, though, that the dependence of (2.108) on k_{uc} is rather weak, because of which most often a rough estimate of the molecule diameter is sufficient.

	formula	r_M [Å]	r_G [Å]
n-pentane	C_5H_{12}	3.585	3.385
n-hexane	C_6H_{14}	3.736	3.812
n-heptane	C_7H_{16}	3.882	4.267
water	H_2O	1.927	0.615
ethanol	C_2H_6O	2.855	2.250
methanol	CH_4O	2.527	1.536
glycerol	$C_3H_8O_3$	3.073	-

Table 2.1: Molecular radii of different sample liquids. The radii given were calculated from molecular weight and density data of the respective liquid [38]. For reference, the molecule's radius of gyration r_G is also given, where available.

If the inequation $k_{\mathrm{vdW}} \ll k_{uc}$ holds, equation (2.108) can be approximated as

$$\sigma^2 \approx \frac{k_B T}{4\pi\gamma} \ln\left(\frac{k_{uc}^2}{k_{\mathrm{vdW}}^2}\right), \tag{2.110}$$

which is equivalent to the result given e.g. by [9].

In this limit, k_{vdW} acts as lower cut-off vector. The cut-off is dominated by gravity or van der Waals forces, depending on the film's thickness [91]. It should be noted that in the case of very thin films ($h \to 0$, typically $h < 10$Å) k_{vdW} can in fact be comparable to k_{uc} (even $k_{\mathrm{vdW}} > k_{uc}$ is possible), meaning that the simple interpretation as a lower cut-off is valid only for films of sufficient thickness.

"Deep" limit: $h \to \infty$

While the result that was presented in this chapter is useful as the most general case, it is difficult to calculate since the formula is numerically ill-conditioned. It is therefore often interesting to consider the case of an "infinitely deep" (i. e., sufficiently deep) liquid, since the dependency on the film thickness is not always necessary.

The limit $h \to \infty$ yields [33]

$$\chi_{zz}(k,\omega) = \frac{k/\rho_m}{(\gamma/\rho_m)k^3 + gk - \omega^2 - i\omega\nu k^2\kappa/(k+\kappa)}. \tag{2.111}$$

(2.111) is numerically much better conditioned[2] than (2.98). Also, it is more efficient to calculate, which makes this variant a desirable option as long as the film thickness is large (usually $h \gg 1\mu\text{m}$).

The mean square surface displacement in this limit is

$$\sigma^2 = \langle u_z^2 \rangle = \frac{k_B T}{4\pi\gamma} \ln\left(\frac{\rho_m g/\gamma + k_{uc}^2}{\rho_m g/\gamma}\right) \approx \frac{k_B T}{4\pi\gamma} \ln\left(\frac{k_{uc}^2}{\rho_m g/\gamma}\right). \tag{2.112}$$

Here the approximation is valid, since $\sqrt{\rho_m g/\gamma} \ll k_{uc}$ is usually satisfied. For example, in the case of n-hexane, the ratio is $\sqrt{\rho_m g/\gamma}/k_{uc} \approx 7 \cdot 10^{-8}$. It is interesting to note that the surface roughness is independent of the liquid's viscosity (which is a general result of the calculation and not only valid for the "deep" limit).

Overdamped and propagating behaviour

The transition of overdamped to propagating capillary waves has been subject to recent research [54, 78, 77]. The advantage of the viscoelastic formalism is that it is able to describe this transition region between the two limits; recent experimental results have shown that e.g. the behaviour of glycerol-water mixtures can be described both qualitatively and quantitatively [54]. Since the viscoelastic formalism should include both limiting cases, it is therefore an important test case to verify that the spectra obtained from this theory converge against the classical results presented in section 2.3.1. Figure 2.11 shows calculations for both a high-viscosity (glycerol, $\rho_m \approx 1260\text{kg/m}^3$, $\gamma \approx 64\text{mN/m}$, $\eta \approx 1500\text{mPa s}$) and a low-viscosity liquid (n-hexane, $\rho_m \approx 655\text{kg/m}^3$, $\gamma \approx 18\text{mN/m}$, $\eta \approx 0.3\text{mPa s}$) at a lateral wave vector of $k = 3.3 \cdot 10^{-6}\text{Å}^{-1}$, which is a value typical of XPCS experiments using a point detector.

The dynamic structure factor of hexane shows a clear lorentzian-like peak at $\omega \approx 54 \cdot 10^3\text{s}^{-1}$, while the power spectrum of glycerol shows a maximum at $\omega = 0$. These results clearly correspond to the two cases which were discussed at the beginning of this chapter.

Figure 2.12 shows calculations based on the same parameters as in figure 2.11, this time comparing the viscoelastic to the classical result given in 2.3.1. The curves show good agreement in the well-known limits, thus strengthening both older experimental and theoretical results and the newer, more general formalism.

[2] I. e., small calculation errors due to the finite precision of every numerical calculation have a significantly smaller effect.

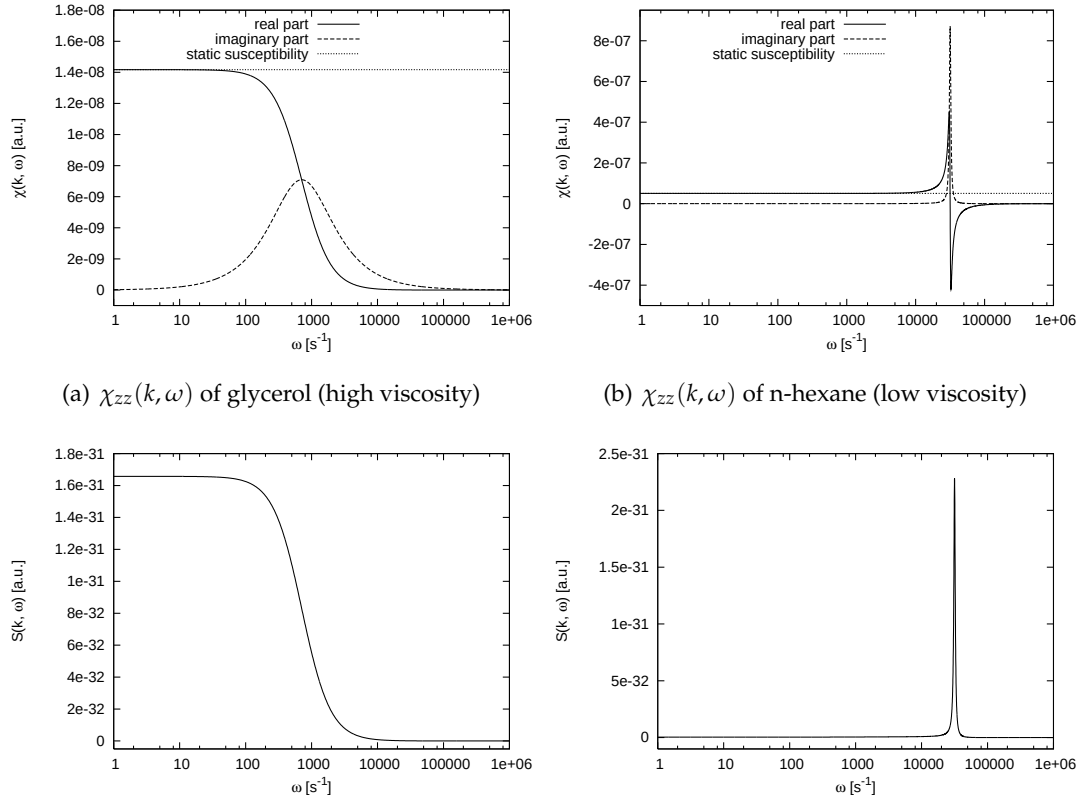

(a) $\chi_{zz}(k,\omega)$ of glycerol (high viscosity)

(b) $\chi_{zz}(k,\omega)$ of n-hexane (low viscosity)

(c) $S(k,\omega)$ of glycerol (high viscosity)

(d) $S(k,\omega)$ of n-hexane (low viscosity)

Figure 2.11: Comparison of the susceptibility and structure factor of high- and low-viscosity liquids. The figures on the left show the calculation results for the parameters of a glycerol sample, while the figures on the right show the results for n-hexane. It can be clearly observed that the susceptibility converges to the static value for $\omega \to 0$. The lower figures show the corresponding calculations for the dynamic structure factor. The wave vector used was $k = 3.3 \cdot 10^{-6}\text{Å}^{-1}$.

Shallow limit ($kh \ll 1$)

A very interesting region is the case of mesoscopically and microscopically thin films; usually this means the region of a few hundred nanometers down to 10Å. In this limit the surface interactions play a major role, and the influence of gravity plays only a minor role. For example, for a thickness of 100nm and an effective Hamaker constant of $A_{\text{eff}} \sim -10^{-20}$J, the van der Waals interaction is typically about 3 orders of magnitude stronger than the gravity influence.

Thin films usually do not show propagating waves. At the solid-liquid interface, movement of the molecules is hampered by the substrate interaction. In the viscoelastic formalism, this is taken into account by means of a no-slip boundary condition at the substrate. The movement

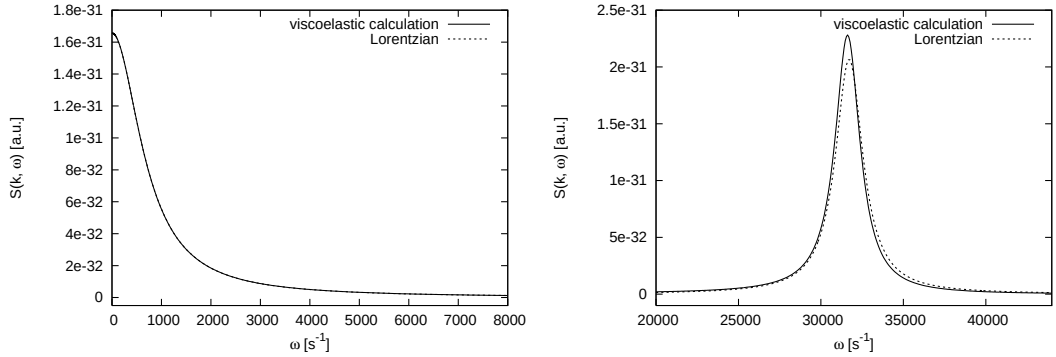

(a) $S(k,\omega)$ of glycerol (high viscosity) (b) $S(k,\omega)$ of n-hexane (low viscosity)

Figure 2.12: Comparison of the viscoelastic to the classical result. The curves in the high-viscosity case (left) are indistinguishable, while the low-viscosity result shows small differences. However, both position and width of the peak are in good agreement.

of molecules in direct vicinity of the substrate is slowed down significantly in the lateral directions.

The result is a dynamic structure factor which shows clearly overdamped characteristics. The following result describes the the dynamic susceptibility in the shallow limit [33]:

$$\chi_{zz}(k,\omega) = \frac{k^2h^3/(3\eta)}{-\mathrm{i}\omega + \left(\left(\frac{\gamma}{\rho_m}\right)k^3 + g'k\right)kh^3/(3\nu)} \tag{2.113}$$

with g' defined as in (2.101).

This result applies only if the following conditions are fulfilled:

$$kh \ll 1 \tag{2.114}$$

$$\text{and } \sqrt{\frac{\omega}{2\nu}}h \ll 1. \tag{2.115}$$

For example, at a film thickness of 100nm and a lateral wave vector of 10^{-5}Å^{-1}, one gets $kh \sim 10^{-2}$. The second limit is usually well-satisfied as well, as will be shown by calculating the film's relaxation time.

The dynamic structure factor takes the form of a Lorentzian (centered at $\omega = 0$)

$$S_{zz}(k,\omega) = \frac{2k_BTk^2h^3/(3\eta)}{\omega^2 + \left[\left(\left(\frac{\gamma}{\rho_m}\right)k^3 + g'k\right)kh^3/(3\nu)\right]^2} \tag{2.116}$$

$$= \frac{2\pi k_BT}{\gamma k^2 + g\rho_m - \frac{A_{\text{eff}}}{2\pi h^4}} \cdot \frac{1}{\pi\Gamma_0\left[1 + \left(\frac{\omega}{\Gamma_0}\right)^2\right]} \tag{2.117}$$

with the damping constant

$$\Gamma_{0,kh\ll1} = \frac{\left(\gamma k^2 + g\rho_m - \frac{A_{\text{eff}}}{2\pi h^4}\right)k^2h^3}{3\eta}. \tag{2.118}$$

This result is analogous to the high-viscosity limit, showing that a sufficiently thin liquid film shows indeed overdamped capillary waves and no propagating modes. Due to the van der Waals interaction, Γ_0 shows a minimum at a certain film thickness (depending on the wave vector), meaning that the surface motion should actually get faster when the thickness decreases.

For a thin hexane film with a thickness in the range between 10Å and 500nm at $k \sim 10^{-5}\text{Å}^{-1}$ with an effective Hamaker constant of -10^{-20}J, one gets e.g. $\max(\Gamma_0) \sim 200\text{s}^{-1}$. If one wants to evaluate the $S(k,\omega)$ function up to e.g. $\omega \sim 100\Gamma_0$, this means $\omega < 2\cdot10^4\text{s}^{-1}$. Therefore, we get $\sqrt{\omega/(2\eta)}h < 0.015 \ll 1$, satisfying (2.115).

Figure 2.13 shows the influence of film thickness on the surface dynamics. The roughness is reduced, while the power spectrum turns to the overdamped case for film thicknesses of 5µm and less. The damping constant shows a clear minimum, meaning that the surface motion gets faster for very thin films (as mentioned above). For film thicknesses $h \sim 10$Å and less, the initial assumption $\sigma \ll h$ is apparantly no longer valid, meaning that for precise results, higher-order terms of the van der Waals interaction would have to be considered. However such ultra-thin films were not investigated in the presented experiments.

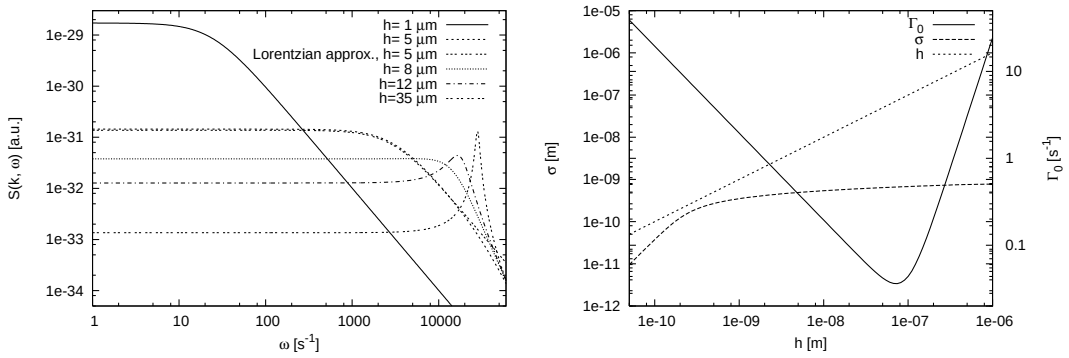

(a) $S(k, \omega)$ (b) Roughness and damping

Figure 2.13: Surface dynamics of thin films. Shown are calculations for a hexane sample at a wave vector $k = 3.3 \cdot 10^{-6} \text{Å}^{-1}$. The left figure shows the transition between propagating and overdamped behaviour. For the 5µm film, the thin-film approximation is shown as well (in the 1µm case, the differences are indiscernible). The right figure shows the influence of film thickness on roughness and damping constant. As a guide for the eyes, the film thickness is shown as well (dashed straight line). It can be seen that the calculated roughness gets very similar to the film thickness for $h \lesssim 1$nm. In this region, the used approximation of the van der Waals interaction breaks down.

3 Experimental results

3.1 Resolution effects in surface-sensitive XPCS

3.1.1 Introduction

In this section, the results of XPCS measurements on liquid surfaces will be discussed. The measurements were performed using the well-known samples n-hexane, ethanol, water and mixtures of ethanol and water. The samples provide a reference point that allows to test the resolution-convolution technique introduced in section 2.2.5.

All the samples show propagating capillary waves at the investigated length scales, allowing to directly decide whether a homodyne or heterodyne correlation function is observed. Since the scattering vector can be determined from the detection angle, the calculated correlation function can be fitted to the observed data just by changing the resolution parameters.

Water occasionally shows the effect of intrinsic heterodyne mixing, which can be explained as a resolution effect. To investigate why water often shows heterodyne functions while e.g. ethanol and hexane do not, the influence of the surface tension was studied. Ethanol is miscible with water at any ratio, allowing for the tuning of the surface tension to any value between those of the two pure liquids.

Measurements on ethanol-water mixtures therefore allow to investigate whether the direct influence of the sample's surface tension that has been discussed in section 2.2.5 (equation (2.63)) is sufficient to explain why water shows intrinsic heterodyne mixing. Another explanation would be that the resolution itself depends on the sample material, which is investigated in the next section.

3.1.2 Experimental station ID10A (ESRF)

The experiments were performed at the experimental station ID10A at the ESRF. ID10A is one of three experimental stations at the undulator ID10, two of which can be used concurrently. The beamline is commonly called the "Troïka" beamline. The stations ID10A and ID10C

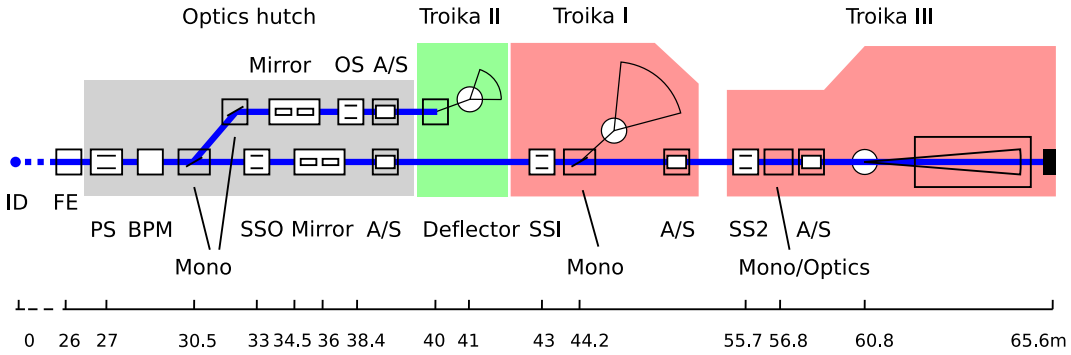

Figure 3.1: Schematics of the Troïka beamline. The radiation from the insertion device (ID) passes through the front end (FE), primary slits (PS) and beam position monitor (BPM), and is monochromatised and collimated further in absorber/slit modules (A/S). The radiation to be used in Troika II is selected in the first monochromator (left). The second (single-bounce) monochromator provides the radiation for Troika I, while Troika III is fed by the third monochromator which is a channel-cut, double-bounce type.

can basically only be used in a mutually exclusive fashion, since the usage of ID10C means that the hutch of ID10A has to be locked. However, it is theoretically possible even to use ID10A/C together in a combined experiment, albeit rarely done.

Figure 3.1 shows the general setup of the Troïka beamline. ID10A or "Troïka I" is situated in the middle, with ID10B (Troïka II) being upstream and ID10C downstream relative to the insertion device.

The insertion device actually consists of three undulator segments in series: one undulator with a 27mm period (U27), one 35mm undulator (U35) and a third section which carries a rotatable setup of both a U27 and U35 undulator, a so-called revolver undulator. Hence the beamline can be used in a 2×U27, 1×U35 as well as in a 1×U27, 2×U35 setup. Highest coherent flux is provided at an energy of $\sim$ 8keV, which is the first harmonic of the U27 and third harmonic of the U35 undulators. The source is a so-called high-β device, meaning essentially that the beam divergence is reduced ($28 \times 17\mu$rad) at the cost of a larger source size ($928 \times 23\mu m^2$). The achievable transverse coherence length at 8keV is $\sim 10\mu$m.

The radiation provided by the source is monochromatised (in the case of ID10A) by a single-bounce, multi-crystal monochromator in horizontal scattering geometry including a Si(111), diamond(111) and diamond(220) crystal. The monochromator can operate at energies $7.5\text{keV} < E < 20\text{keV}$. The intrinsic energy resolution is $0.2 \cdot 10^{-4} < \Delta E/E < 1.4 \cdot 10^{-4}$, yielding a longitudinal coherence length of about 1μm at 8keV.

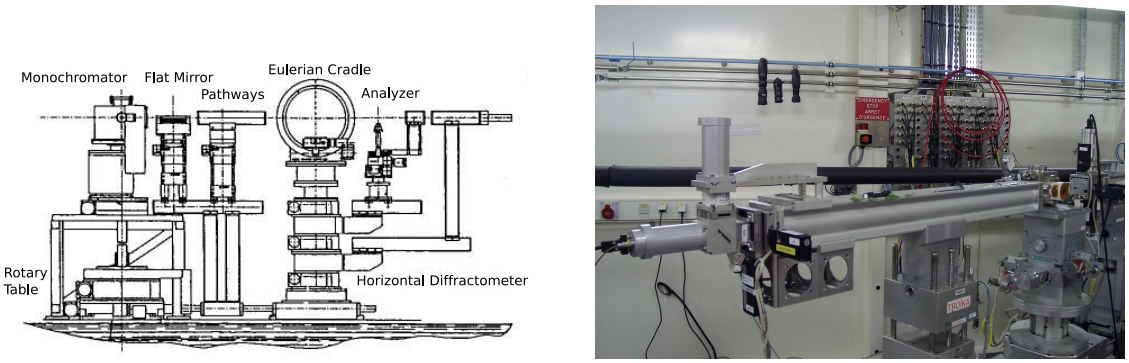

Figure 3.2: ID10A diffractometer. The figure shows a typical setup possibility. The sample cell is commonly placed in the Eulerian cradle; however, in the presented experiments the cradle was not used and therefore not mounted. The right subfigure shows a photograph of the hutch from a different perspective (radiation coming from the right, detector on the left).

The sample cell is mounted into a general purpose 6-circle diffractometer that can be configured for a wide range of different applications (figure 3.2). In our case, the radiation is deflected downwards by a mirror and hits the sample surface at a fixed, shallow angle.

The setup is similar to the setup for surface-sensitive XPCS measurements shown in figure 2.6. The radiation hits the sample at an angle below the critical angle of total external reflexion, limiting the penetration depth into the surface to $\sim$ 100Å. The scattered radiation coming from the sample is detected by an avalanche photo diode (APD), which has the advantage that it can detect very high incoming fluxes at a very high signal-to-noise ratio. The APD is connected to an autocorrelator system which is able to calculate the intensity autocorrelation function in-situ.

The scattering vector depends on the position of the detector, which is determined by a pair of cross slits directly in front of it. Those slits can be moved with µm precision; the detector aperture is therefore very well defined, yielding the possibility to scan the $\vec{q}$ space with high resolution. Directly in front of the sample cell a very small aperture, the pinhole, is placed. The pinhole is used to reduce the beam size, shrinking the scattering volume down to a value comparable to the coherence volume of the radiation. This allows for partially coherent illumination of the sample. A set of guard slits after the pinhole suppresses the Fraunhofer fringes produced by it.

The described beamline setup was used mainly to investigate the dynamics of free liquid surfaces. In this case the sample cell consists of a shallow trough (figure 3.3) with a diameter

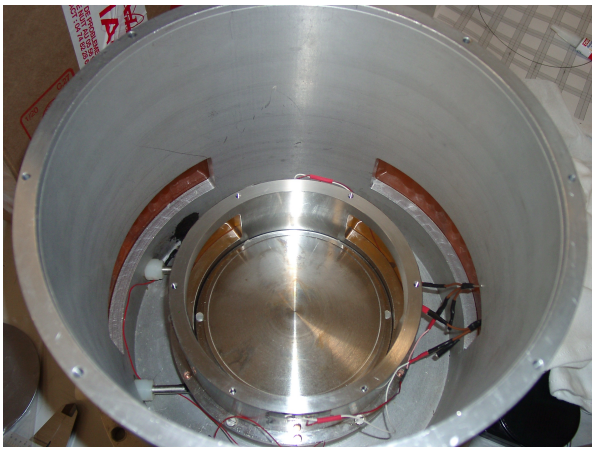

Figure 3.3: Sample trough for grazing-incidence measurements on liquids. The sample cell uses a two-layer design, with the inner cell containing the trough, and an outer cell for increased insulation. The former is placed on top of a combined cooling/heating plate, which can be cooled by e.g. water or nitrogen and temperature-controlled by a heating foil.

of about 10cm and a depth of 1mm or less, to suppress macroscopic waves. The trough is situated inside an air-filled gas-tight cell.

The sample temperature is stabilised at 15°C, which is 5-6 degrees below the temperature inside the experimental hutch. Temperature control is done by flux-controlled cold gaseous nitrogen in combination with an automated temperature controller device (Lakeshore, model 340). A constant temperature increases the stability of the setup, since a free liquid is very susceptible to external perturbation. For the same reason, usually all pumps in the hutch are switched off during the experiment.

3.1.3 Sample systems

In this section, the sample systems investigated will be presented. In particular, two sets of samples were used: n-hexane and ethanol-water mixtures. Hexane (C_6H_{14}) is a non-polar liquid which is part of most fuel mixtures for motor vehicles, as well as being used as a cleaning agent, since it is very lipophilic. Ethanol (C_2H_6O) is a commonly-used alcohol, found e.g. in cleaning liquids, with the important feature that it is fully miscible with water at any ratio. Water (H_2O) finally is a strongly polar liquid and has been subject to numerous theoretical and experimental studies, e.g. concerning wetting behaviour or its role as solvent for organic molecules [26, 65, 75].

The selection of sample liquids was made because of the observation that water regularly shows a heterodyne correlation function (section 2.2.2), while e.g. hexane shows a homodyne

	Formula	ρ_m[g/L]	η[mPa s]	γ[mN/m]
Water	H_2O	0.998	1.00	72.75
Ethanol	C_2H_6O	0.789	1.19	22.68
N-Hexane	C_6H_{14}	0.655	0.32	18.43

Table 3.1: Some selected mechanical properties of the sample materials. Shown are the liquid's density ρ_m, the viscosity η and the surface tension γ under normal conditions. Data taken from [28, 42, 43, 51].

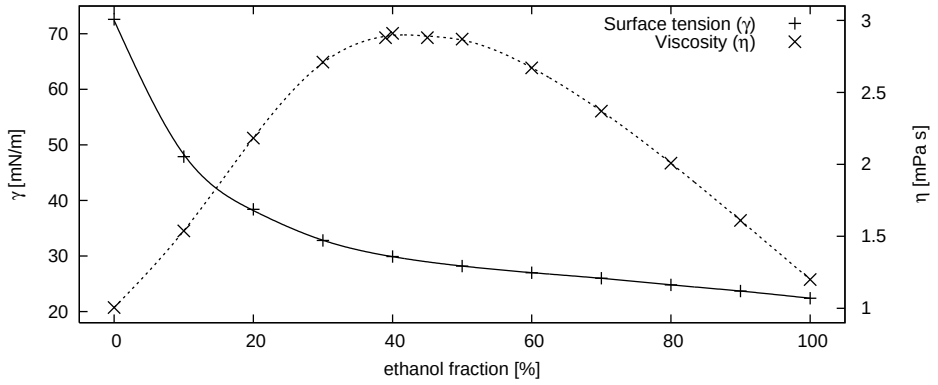

Figure 3.4: Surface tension and viscosity of ethanol-water mixtures. The lines show a smoothed spline interpolation. Data taken from [44, 45].

function. A main difference between the two samples is their surface tension: the value at room temperature is $\gamma \approx 73$mN/m for water and only 18mN/m for hexane. Both samples have a low viscosity ($\eta \approx 1$mPa s for water and $\eta \approx 0.3$mPa s for n-hexane), leaving the surface tension as the most prominent difference in fluid properties (see table 3.1).

To investigate the transition region between low and high surface tension, ethanol-water mixtures have been investigated. The surface tension determines the intensity of the diffuse scattering and therefore has an influence on whether a heterodyne or homodyne correlation function is detected. Ethanol has a low surface tension, comparable to that of n-hexane ($\gamma \approx 23$mN/m), and a low viscosity as well ($\eta \approx 1.2$mPa s). Since both substances are fully miscible at all ratios, the mixture's surface tension can be tuned to a specific value.

The dependence of both surface tension and viscosity of binary ethanol-water mixtures on the substance ratio is shown in figure 3.4. It can be seen that the surface tension drops steeply even when only small amounts of ethanol are present in the mixture. For ethanol fractions of 50% or more the surface tension is already very similar to the value of pure ethanol, changing only slowly. The viscosity increases noticeably for small ethanol fractions, reaching a maximal

value of about 3mPa s at a ratio of $\sim 50\%$. For larger ethanol fractions, the viscosity decreases again towards the low ethanol value of 1.2mPa s.

However, a maximal value of 3mPa s is still relatively low, especially when compared to highly-viscous liquids like e.g. glycerol ($\sim$ 1500mPa s), which shows overdamped behaviour [77]. It is therefore expected that ethanol-water mixtures at any ratio show propagating capillary waves on their surface, making them an ideal candidate to study the influence of the surface tension on the observed correlation function.

The Ethanol used was produced by Riedel-de Haën and provided a purity of $\geq 99.8\%$. The n-hexane produced by Fluka was of purissum grade, showing $\geq 99.0\%$ purity. Both samples were ordered from Sigma-Aldrich. The water was filtered using a PURELAB ultrapure-water filtration system available at the beamline.

3.1.4 Results

Hexane

In order to optimise the XPCS technique and further its understanding, n-hexane has been used as a standard sample several times (e.g. [82]). Since it has a very low viscosity, its power spectrum at the surface should be well-described by a simple Lorentzian, yielding a simple, exponentially-damped $\cos^2$ function (see sections 2.2 and 2.3) of the form

$$g_{2,\text{low-visc.}} = 1 + \cos^2\left[\omega_0(\vec{q})\tau\right] \mathrm{e}^{-2\Gamma(\vec{q})\tau}. \tag{3.1}$$

However, when trying to analyse correlation functions of n-hexane taken at ID10A at different occasions (e.g. [82] and measurements taken for this thesis), one notices that these functions are very difficult to analyse, and even the best fit to the data does not describe the data well. This can be seen in figure 3.5.

While the measured correlation function is apparently homodyne, the calculation according to equation (3.1) does not match the observed data at all. Due to the low viscosity of hexane, the damping of the oscillation should be very weak, but the measured function is quite strongly damped. Also, the frequency is clearly shifted towards higher values.

If one tries to analyse the given correlation function using the idealised result given in section 2.2, the only possible fit parameters are the viscosity of the liquid η and the surface tension γ. The scattering vector is given by the experimental setup and is therefore fixed. The result of fitting the surface tension and viscosity is shown in the figure as well; corresponding

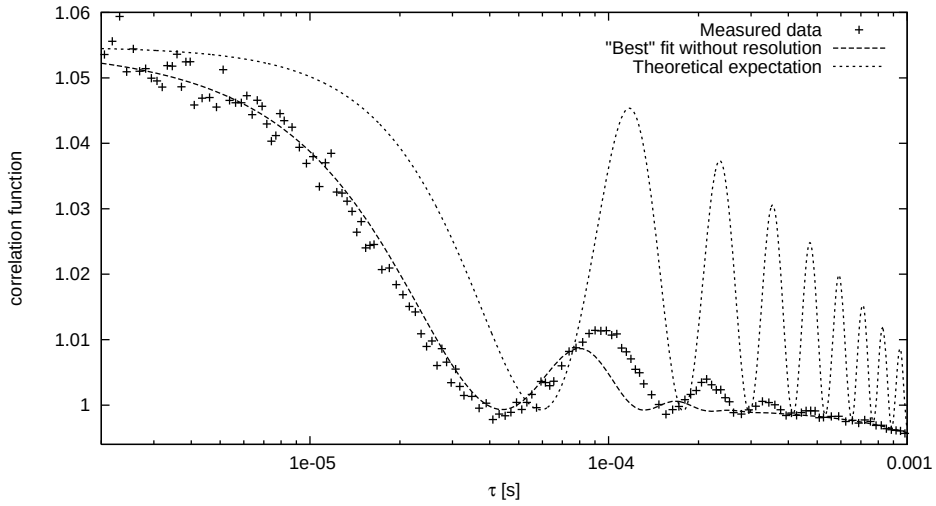

Figure 3.5: Correlation function of n-hexane, taken at ID10A. The measurement was done at an energy of 8keV and a pinhole size of $50 \times 50\mu$m. The calculation according to eq. (3.1), assuming the Fraunhofer case and complete coherence, is very different from the one that is observed. Also shown is the best possible fit achievable when varying the surface tension and viscosity as parameters.

to the curve are $\gamma = 33$mN/m and $\eta = 4.1$mPa s. In comparison to the expected literature values listed in table 3.1, the data fit according to eq. (3.1) therefore yields a surface tension that is off by a factor of 2, and a viscosity that differs by more than one order of magnitude.

It is noticeable that even this best fit according to the simple ansatz (3.1) does not describe the measured data well. Especially the positions of the maxima as well as their height are not reproduced correctly. In the past, a phase shift has been introduced in the correlation function

$$g_{2,\text{shift}} = 1 + \cos^2[\omega_0(\vec{q})\tau + \phi]\mathrm{e}^{-2\Gamma(\vec{q})\tau}, \tag{3.2}$$

for the interpretation of dynamic light scattering data, improving the agreement between fit and measurement [20]. However, this is not justifiable from a theoretical point of view. Furthermore, although the data can be significantly better described by introducing such an arbitrary additional parameter, the problem remains that it is still not possible to reliably deduce any sample properties from the measurement.

The measurements were taken at relatively small scattering vectors (e.g. $q_{||} = 3 \cdot 10^{-6}\text{Å}^{-1}$, corresponding to a lateral length scale of $\sim 200\mu$m). In this region, the validity of the capillary waves model is well-established by dynamic light scattering and other techniques [48]. This means that the discrepancy between measured functions and expected results has to be searched for in the scattering mechanism itself.

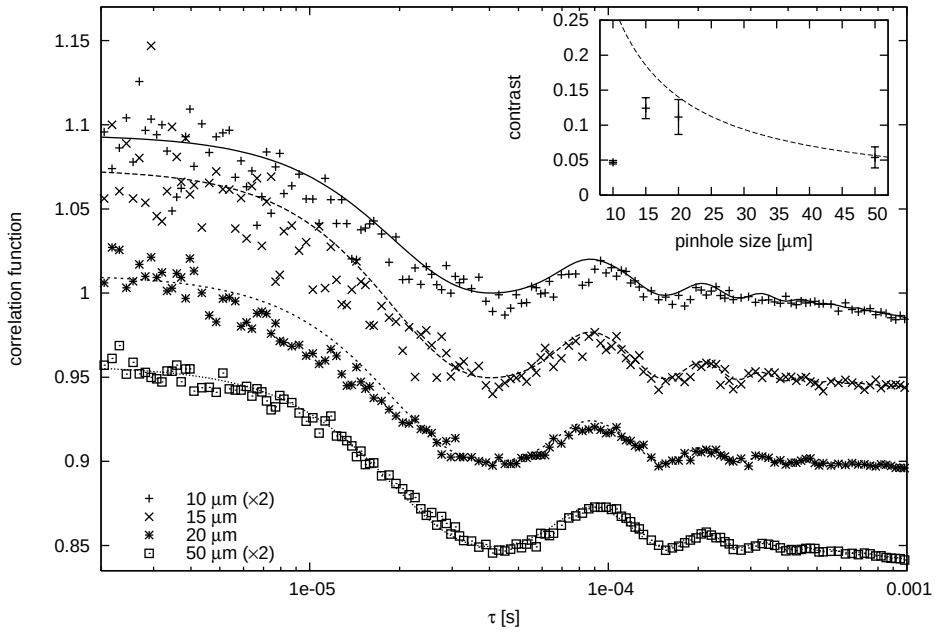

Figure 3.6: Influence of pinhole size on effective resolution. The figure shows correlation functions of n-hexane, taken at ID10A. The measurements were performed using different pinhole settings (10, 15, 20 and 50µm). The functions are shifted for clarity reasons, and the 10µm and 50µm data sets have been scaled-up by a factor of 2. All functions can be explained using the same resolution values, which means that pinhole size has at most a very small influence on the resolution function. The inset shows the achieved contrast values, as opposed to a theoretical estimate.

The most likely explanation is therefore that the assumption of sufficient coherence and Fraunhofer scattering is invalid, and that the idealised expressions commonly used to interpret data in dynamic light scattering cannot be used in unmodified form in XPCS. In fact, such measurements on n-hexane as shown here were the starting point for considering the influence of finite experimental resolution caused by partial coherence and Fresnel scattering on the results of surface-sensitive XPCS experiments.

If the data is re-analysed taking a finite resolution into account using the formalism described in section 2.2.5, the agreement between measurement and theoretical result is improved significantly. Figure 3.6 shows the hexane data analysed with taking a finite experimental resolution into account. The agreement between the modelled curves and the measured data is good, meaning that every correlation function can be explained just by using the known values for the surface tension and viscosity.

The correlation functions in figure 3.6 present in fact a series of identical measurements, where only the pinhole size has been changed between individual sets. All curves can be

modelled using the same resolution parameters ($\delta q_x = 2.2 \cdot 10^{-7}\text{Å}^{-1}$, $\delta q_y = 1.9 \cdot 10^{-5}\text{Å}^{-1}$), meaning that the pinhole size has only a small influence on the experimental resolution. However, it has a strong influence by means of the achievable contrast. In homodyne detection mode, the contrast should be maximal for a pinhole size $L \leq \xi_t$, and decrease for larger pinhole sizes as $\sim L^{-2}$ [55, 90]. In grazing incidence, due to the strongly asymmetric footprint of the radiation on the sample, there is almost no out-of-plane scattering. Thus the scattering is dominated by the in-plane scattering, yielding a L^{-1} behaviour as shown in the inset of figure 3.6.

However, the data shows that this idealised behaviour is usually not observed in practise, since beamline instabilities and alignment problems decrease the actually achieved contrast. Furthermore the undulator is not a point source, and shows domains of different coherence lengths. Because of these effects the contrast can actually decrease for very small pinhole sizes as has been observed here. A "rule of thumb" at the ID10A is that the highest contrast values are achieved for pinhole sizes $\sim 12 - 15\mu\text{m}$.

It should be noted that the resolution parameter in q_y direction is actually much larger than the scattering vector itself. This is to be expected due to the scattering geometry, as y is the direction perpendicular to the scattering plane. The large q_y resolution has a strong influence on the data, as it is the main reason for the observed frequency being shifted towards higher values. In the case of very good q_y resolution $\delta q_y \ll \delta q_x$ the observed correlation function would be shifted towards lower frequencies.

Another series of measurements varied the detector aperture at the same scattering vector position, in order to see if this has a strong influence on the experimental resolution. The results are shown in figure 3.7. Again, each curve can be modelled using the same resolution function, meaning that the detector aperture has little influence on the effective experimental resolution.

However, the contrast is again influenced strongly by the aperture setup. Theoretically, the contrast should decrease as $\sim a^{-1}$, where a is the aperture size [55, 90]. This behaviour is reproduced well, but the actual contrast values are only $1/17$ of the theoretical estimates. A common reason for such low contrast values are alignment problems. At ID10A, values $20\mu\text{m} \leq a \leq 50\mu\text{m}$ usually present a good compromise between contrast and flux, maximising the signal-to-noise ratio.

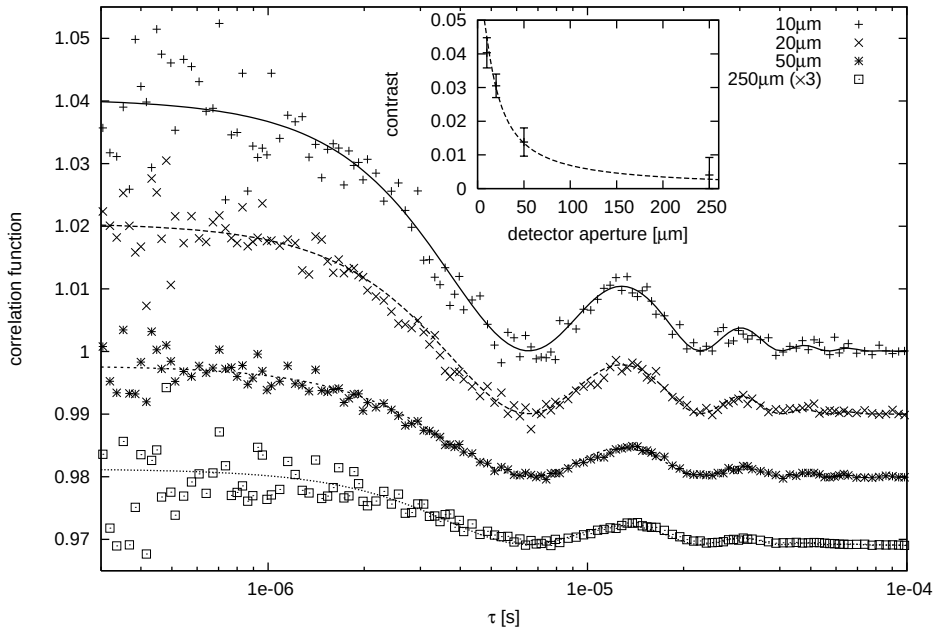

Figure 3.7: Influence of detector aperture on effective resolution. The functions are shifted for clarity, and the 250µm data has been scaled-up by a factor of 3. All functions can be modelled using the same resolution parameters ($\delta q_x = 7.4 \cdot 10^{-7}$Å^{-1}, $\delta q_y = 2.0 \cdot 10^{-5}$Å^{-1}). The contrast as a function of the aperture size is shown in the inset, with the solid line showing a scaled theoretical estimate. The calculated contrast values had to be scaled down by a factor of 17, indicating an alignment problem. However, the functional behaviour is still correct.

Water-ethanol mixtures

As discussed in section 2.2.5, the resolution function has a great influence on whether a homodyne or heterodyne correlation function is observed. In the past, such intrinsically heterodyne correlation functions have been observed during measurements on water surfaces [29], while other XPCS measurements under similar experimental conditions usually showed homodyne functions. The most prominent difference between water and the other investigated samples was the surface tension, and enters equation (2.63) in form of a factor $1/\gamma$. Ethanol-water mixtures permit the continuous variation of the surface tension between the large value of water and the relatively low value of ethanol. This allows for a systematic investigation of the influence of the surface tension on the measurement results.

As seen before, water showed heterodyne correlation functions for all investigated scattering vectors, while ethanol showed homodyne functions. Figure 3.8 summarises the measurements: the mixtures can be divided into two groups – the "water-like" and the "ethanol-like"

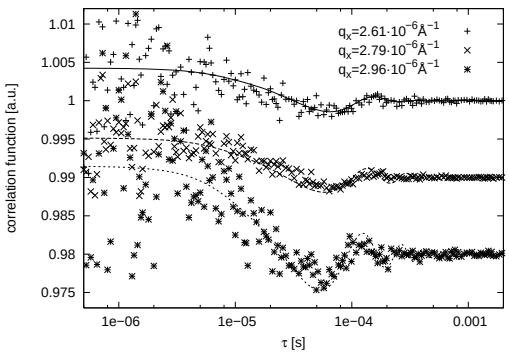

(a) 0% ethanol

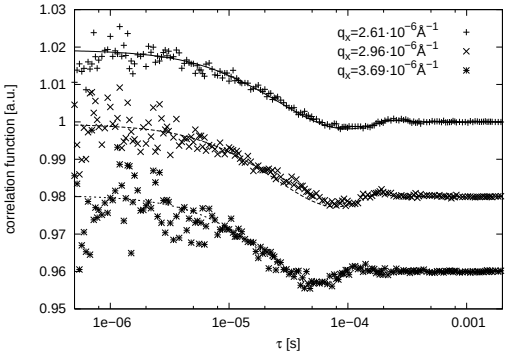

(b) 50% ethanol

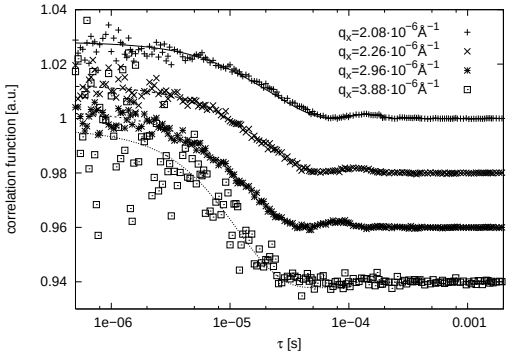

(c) 60% ethanol

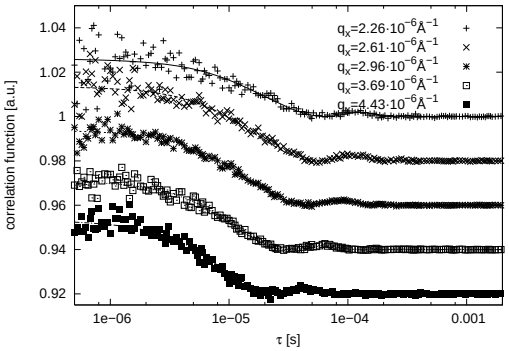

(d) 75% ethanol

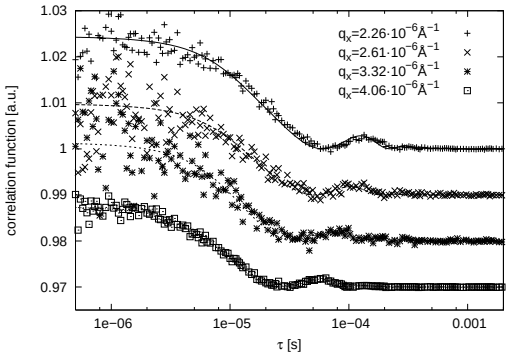

(e) 100% ethanol

Figure 3.8: Correlation Functions of water-ethanol mixtures. Shown are individual measured functions for different water-ethanol ratios. Some of the correlation functions have been scaled to make the individual functions of the respective series comparable to each other. It is noticeable that the samples with lower ethanol fractions show heterodyne correlation functions, while the higher fractions yield homodyne ones.

samples. The water-like group showed heterodyne correlations, while the ethanol-like group showed homodyne ones.

All correlation functions showed propagating capillary waves, which was verified using the viscoelastic formalism (section 2.3.2). The results indicate that the simple Lorentzian description used in the resolution calculations is still a sufficiently good approximation, albeit yielding oscillation frequencies that are slightly too high (about 5%).

The transition between heterodyne and homodyne detection happened in this experiment at an ethanol fraction of $\sim$ 60%. At a fraction of 50%, the measured functions were quite clearly heterodyne, while the 75% results were homodyne. The 60% results seem to be in the transition region between homodyne and heterodyne, albeit basically homodyne. Nevertheless, the 60% functions can only be described properly if one assumes a resolution that is very close to the transition, making the heterodyne and homodyne fractions in the signal almost comparable.

It is not possible to fit all measured data taken at a specific scattering vector q_x using the same resolution parameter. The heterodyne correlation functions show a slightly increased resolution when compared to the homodyne results. This dependence on the sample material was quite surprising, since a mechanism how e.g. the surface tension of the sample can directly influence the experimental resolution is not clear. While (2.63) does include a direct dependence on the surface tension, this dependency is insufficient to explain the data.

The homodyne part is suppressed by the surface tension as $\sim \gamma^{-1}$, but between 50% and 75% ethanol fraction the surface tension changes only by $\sim$ 10%, which is not sufficient to explain the change in the measured functions. One possibility is the mechanical stability of the surface, which is a function of several different parameters like the total amount of liquid in the trough, the liquid's surface tension, vibrations in the experimental hutch and possibly others.

Another possibility is a slight curvature of the sample surface. Since the diameter of the sample trough is limited, the surface is not completely flat. Especially in the case of a liquid with high surface tension, a noticeable meniscus forms, yielding a slight curvature in the middle of the trough. The footprint of the incident beam on the sample surface is about $5 - 10$mm long. On this short length, the surface is usually assumed to be sufficiently planar. On the other hand, a slightly curved surface acts like a concave mirror, changing the effective distance between sample and source. This might modify the experimental resolution sufficiently to cause the transition. However, since the amount of liquid in the trough is

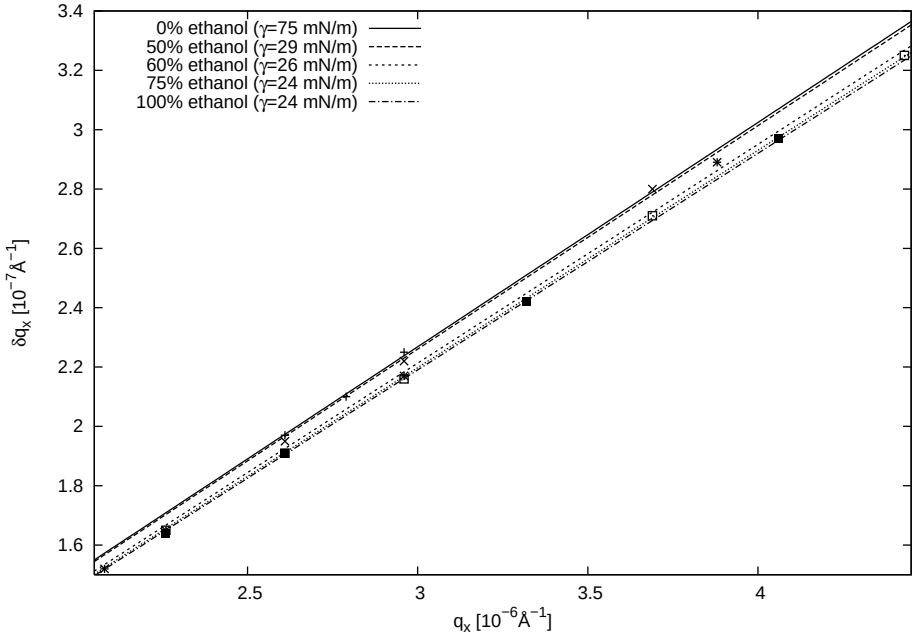

Figure 3.9: Effective resolutions in the water-ethanol measurements. The straight lines represent linear fits to the individual resolution values, which are marked by points. The resolutions have been chosen to be as close to the homodyne-heterodyne transition as possible. Two distinct "sets" of lines can be discerned. The lower set belongs to homodyne measurements, while the upper set belongs to the heterodyne ones.

slightly different for every sample preparation, one would expect different resolution values if the same sample is prepared multiple times. This has not been observed in the measurements.

If one assumes that the resolution is only modified slightly by the sample setup, a set of most-likely resolution parameters can be calculated. The dependence of the correlation function on the resolution in the x-direction is actually quite weak, as the form of the curve is dominated by the q_y resolution, since $\delta q_y \gg \delta q_x$. Due to this weak dependence, normally only a rough estimate of δq_x can be calculated. This means that one can choose δq_x from a large interval without significantly changing the correlation function. However, a change in δq_x is responsible for the homodyne-heterodyne transition. The most likely resolution parameters in x are therefore very close to the transition region, since results from both regimes have been observed in the experiment.

Figure 3.9 shows the resulting resolution values. δq_x increases linearly with q_x. While the resolution in a particular setup cannot be calculated directly, one can make some simple estimates in order to check if the observed linear relationship is at least correct. For this purpose, we will interpret the resolution δq_x as a simple perturbation on the incident angle α_i. This corresponds to the simple geometric interpretation of coherence given in section

2.1.3 where the transverse coherence length is simply a function of the beam divergence. Furthermore, we assume here that δq_x is dominated by the transverse coherence length.

Following section 2.1.3, the coherence length is connected to the beam divergence in the following way:

$$\xi_t = \frac{\lambda}{2\delta\alpha_i} \quad \Leftrightarrow \quad \Rightarrow \delta\alpha_i = \frac{\lambda}{2\xi_t}. \tag{3.3}$$

Consider the scattering vector in x direction given by

$$\begin{aligned} |q_x| &= k\,|\cos(\alpha_i + \Delta\alpha) - \cos(\alpha_i)| && (3.4)\\ &\approx \frac{k}{2}(2\alpha_i\Delta\alpha + \Delta\alpha^2) && (3.5)\\ &\approx k\alpha_i\Delta\alpha, && (3.6) \end{aligned}$$

where $\Delta\alpha$ denotes the angular displacement from the specular position. It has been assumed here that this is small compared to the incident angle ($\Delta\alpha \ll \alpha_i$), which is not true in a strict sense. However, the error in q_x due to the approximation is less than 20%, which should still work well for a rough estimate. Now we consider the effect of a perturbation in α_i on q_x:

$$\begin{aligned} \delta q_x &= \frac{\partial q_x}{\partial \alpha_i}\delta\alpha_i && (3.7)\\ &= k\Delta\alpha \cdot \delta\alpha_i && (3.8)\\ &\approx \frac{|q_x|}{\alpha_i}\delta\alpha_i && (3.9)\\ \text{eq. (3.3)} \Rightarrow &= \frac{\lambda}{2\alpha_i\xi_t}|q_x|. && (3.10) \end{aligned}$$

The x-resolution is therefore expected to be (approximately) proportional to q_x, as is supported by the measurements. Furthermore, we can even estimate e.g. the transverse coherence length from the ratio $\delta q_x/|q_x|$. The slope of the lines in figure 3.9 is approximately $7.5 \cdot 10^{-2}$, the incident angle was $\alpha_i \approx 0.113^\circ$ and the wave length $\lambda \approx 1.55$Å (8keV). This yields a transverse coherence length of $\sim 0.5\mu$m, which is about one order of magnitude lower than the expected value ($\sim 10\mu$m).

The effective resolution is therefore clearly not only a function of the nominal coherence length, although it seems to be the dominating quantity. However, the actual values still have to be determined as indirect measurement results as demonstrated. It should be possible to

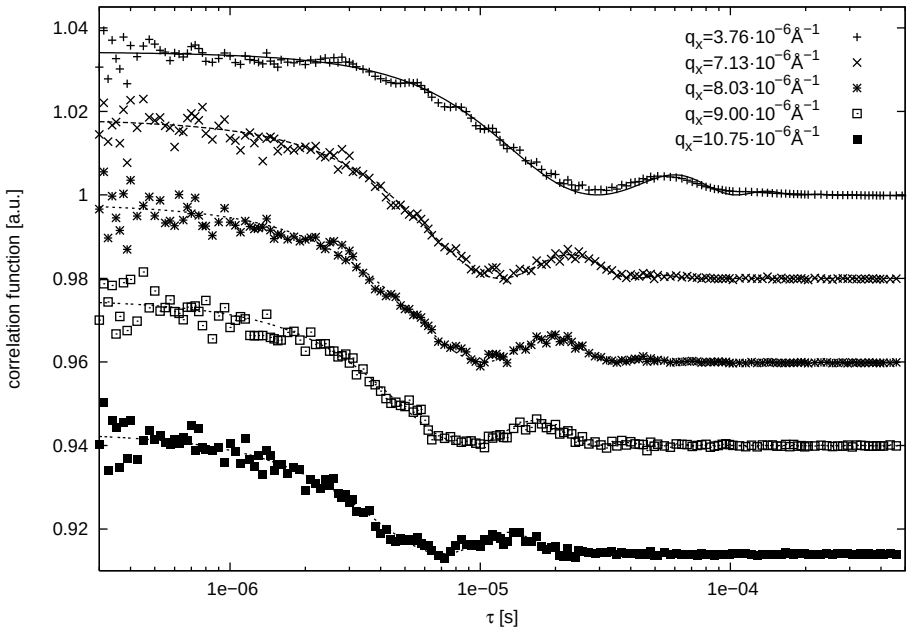

Figure 3.10: Correlation functions of ethanol measured using a Fresnel zone plate, taken at ID10A.

use the resolution parameters obtained this way in a consecutive measurement, e.g. with an unknown sample liquid.

Fresnel zone plate

To see if the resolution function can be broadened by optical elements, possibly leading to e.g. heterodyne correlation functions on samples where those were not observed before, a Fresnel zone plate (FZP) was placed in the beam. In this setup, there is no pinhole, as the scattering volume is limited by the focussing of the Fresnel lens.

The resulting correlation functions can be seen in figure 3.10. They can be described using a q_y resolution of $1.5 \cdot 10^{-5}\text{Å}^{-1}$, which means that the effective resolution broadening was in fact reduced by the FZP and not increased as anticipated. The functions show a low contrast of $\sim 3\%$ which is almost constant over a large q_x range. However, the signal-to-noise ratio is quite high, as the focussing of the zone plate increases the coherent flux on the sample by at least one order of magnitude. This allowed for comparatively large maximal scattering vectors, which were about twice as large as using the pinhole setup. The maximal scattering vector reached was $10.8 \cdot 10^{-6}\text{Å}^{-1}$, corresponding to a lateral length scale of about 60µm.

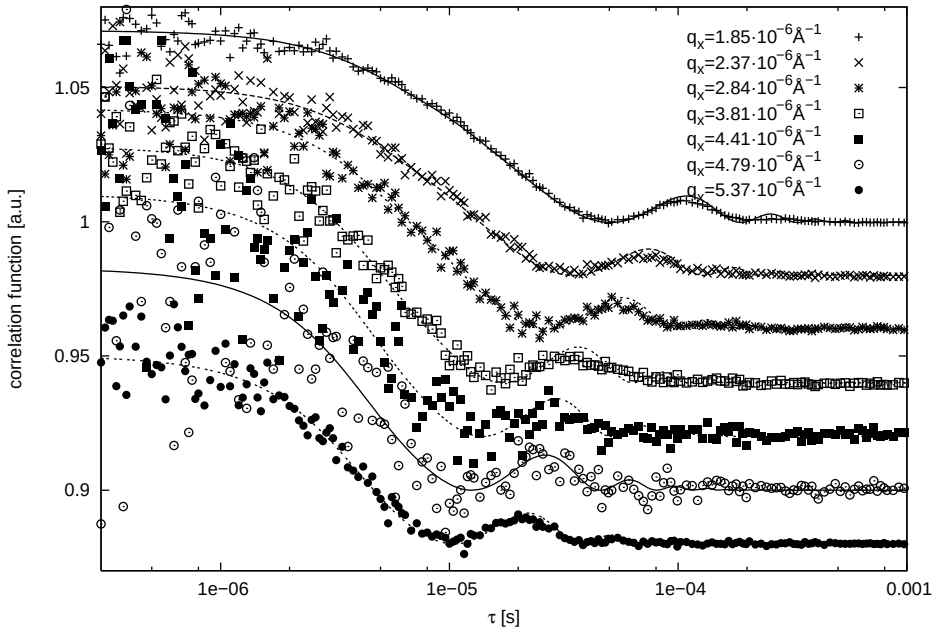

Figure 3.11: Homodyne correlation functions of water. Since the measured correlation functions differ noticeably in contrast, they have been scaled to become comparable. All functions can be described using the same resolution parameters.

Although this length scale is still in a range that is reachable by visible-light techniques, the zone plate modification is very promising. While amplifying the coherent flux is not a universal possibility to increase the scattering vectors by arbitrary amounts (as e.g. beam damage problems also increase), it shows quite impressively that the full potential of the XPCS technique is not reached yet.

The FZP seems to amplify the effect of beam position fluctuations on the signal, as can be seen on the high-frequency oscillations that some of the functions show, e.g. $q_x = 3.76 \cdot 10^{-6}\text{Å}^{-1}$. The strongest oscillation on top of the actual signal has a frequency of 355.4kHz, which corresponds to the storage ring frequency. However, the relative contrast of these artifacts is low, which means they can usually be ignored during analysis.

Outlook

Since the effect of intrinsic heterodyning is still not completely understood, another experiment has been conducted. The original intention was to start again with water samples, which were expected to show heterodyne correlation functions, and then modify the samples' characteristics by e.g. adding tensides which reduce the surface tension. However, this time

water showed homodyne correlation functions, which of course has great implications on the question of the sample-dependence of the experimental resolution.

Figure 3.11 shows the results of this experiment. The correlation functions are clearly homodyne, very different to the heterodyne functions seen during the measurements on ethanol mixtures and e.g. [29]. Due to the weak dependence on the resolution function in the x direction, all functions could be described using the same resolution parameters ($\delta q_x = 1.5 \cdot 10^{-7} \text{Å}^{-1}$ and $\delta q_y = 2.2 \cdot 10^{-5} \text{Å}^{-1}$). Due to the missing homodyne-heterodyne transition, a q-dispersion of the q_x resolution like in the mixtures data could not be calculated.

A possible explanation of the different results are subtle differences of the optical setup. While all described experiments took place at the ID10A beamline, some optical elements were changed between them. This includes the pinhole, which in the past was usually a set of pre-defined etched holes in a metal foil. During the measurements on hexane described earlier, an experimental cross-slit by JJ X-ray was used. This slit setup was dropped later since it did not deliver on the expectations, especially concerning parasitic edge scattering and the well-definedness of the pinhole. The last water measurements were performed using a set of "rollerblade" cross-slits developed by the ESRF, which provide for a very well-defined pinhole setup.

Furthermore, the stability of the beamline was enhanced, suppressing drifts and vibrations even further. The result was a much improved stability of the experimental setup in general. One could argue that the beamline used for the first measurements was actually quite different from the one during the last measurements. This underlines the previous statement that it is very difficult – if not impossible – to predict the experimental resolution function completely from theoretical considerations.

Another effect that was observed points into the same direction: from time to time, a "spike" was observed in the measured intensity, i.e. the intensity increased by at least one order of magnitude for a short period of time. During these spikes, often heterodyne correlation functions were observed.

One particularly clear example for this very interesting effect is shown in figure 3.12. The measurement shown was actually part of the water-ethanol mixture experiment discussed earlier, but the behaviour was the same. The sample was a mixture containing 75% ethanol, which – apart from this example – showed almost exclusively homodyne correlation functions during the whole experiment. In this particular case the measured intensity increased significantly in a matter of seconds, and the measured correlation function changed almost

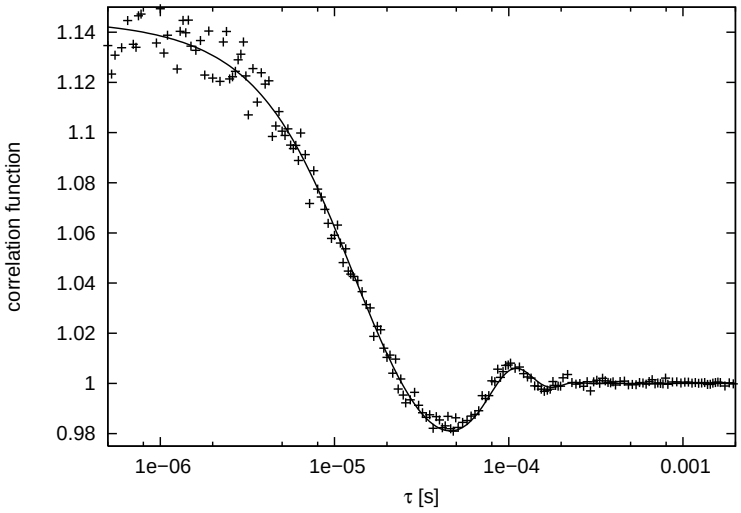

Figure 3.12: Heterodyne correlation function of a water-ethanol mixture containing 75% ethanol. The observed function is actually not 100% heterodyne but rather "mixed", since the heterodyne function is superimposed on a homodyne one.

immediately from homodyne to heterodyne. However, the function saved by the autocorrelator was a mixed function including a $\sim 30\%$ homodyne fraction, since the measurement had already been running for several minutes. After the intensity spike, the state reverted, yielding a purely homodyne correlation function in the next measurement.

The occurrence of spontaneous heterodyne mixing contains little practical value at the moment, but it shows that systematic heterodyning should indeed be possible. Also, both contrast and signal-to-noise ratio of the measured function were very high. This seems to contradict the theoretical prediction that the contrast of the correlation function is significantly lower in the heterodyne case (see section 2.2.4). Furthermore, the high signal-to-noise ratio shows that there seems to be indeed a significant gain in heterodyne mixing.

A working setup for systematic heterodyne mixing could not be implemented successfully yet, although tests using mirrors and diffraction gratings showed that parts of the specular intensity can be deflected towards the detector position. Figure 3.13 shows the diffraction peaks from an X-ray transmission grating [13]. The scan shows noticeable maxima even at higher diffraction orders, which means that at the corresponding detector position a heterodyne correlation functions should be observed. However, experimental results so far indicate an incoherent superposition of the scattered fields, leading to a vanishing contrast in the correlation function and no observable heterodyne mixing.

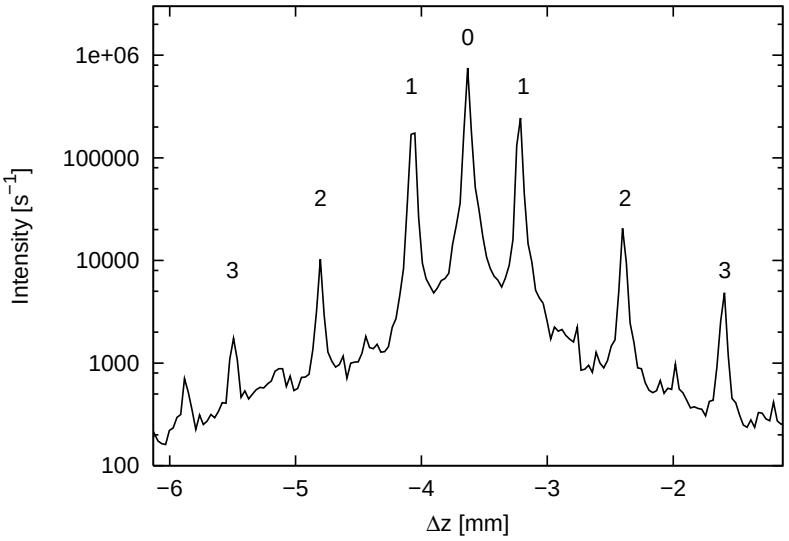

Figure 3.13: Diffraction maxima from an X-ray diffraction grating, measured at the beamline ID10A (ESRF). Three diffraction orders of high aspect ratio can be distinguished. The measurement was performed using a grazing-incidence setup similar to the one shown in figure 2.7.

3.1.5 Summary

It has been shown that the resulting correlation functions of surface-sensitive XPCS measurements cannot be interpreted correctly without taking a finite experimental resolution into account. A simplified formalism has been proven to be useful in both the description and analysis of the data, making it possible to indirectly measure the resolution function of the setup as a fit parameter during a reference measurement. The resulting values can then be used to correctly interpret the data of the actual sample.

It has been shown that finite experimental resolution is a probable explanation for the effect of intrinsic heterodyning, and that the experimental resolution depends on the sample setup in subtle ways. This can cause a slight apparent dependence of the resolution on the sample, possibly changing the detected correlation function from homodyne to heterodyne.

A promising modification in the form of a Fresnel zone plate has been tested, which resulted in a significant increase in the maximal q_x vector that could be reached. Furthermore, non-intrinsic heterodyne mixing has been observed at least once, and with very good signal-to-noise ratio. Therefore heterodyning remains a very interesting subject of research with the possible gain of increasing the maximal scattering vectors.

First tests to implement heterodyne mixing in XPCS have been performed. It could be shown that it is possible to deflect parts of the specularly reflected intensity off a liquid surface towards the detector positioned in the diffuse scattering region. Furthermore, a first successful experiment reaching nanometer length scales has already been performed. In this case, metal clusters on polymer thin films were used to increase the scattered intensity at high $q_{||}$ values [86]. These results indicate that at the moment the potential of XPCS is not completely exploited by far, and that it will be possible to investigate nanometer-scale dynamics of a wide range of systems in the near future.

3.2 Energy-dispersive coherent scattering

3.2.1 Introduction

The XPCS measurements on ethanol-water mixtures presented in the previous section indicated a possible sample dependence of the experimental resolution. To investigate this possibility further, a variation of Young's double-slit experiment was combined with a surface-sensitive scattering setup.

A double-pinhole that is coherently illuminated shows a pronounced diffraction pattern. The visibility of the intensity minima

$$V = \frac{I_{\max} - I_{\min}}{I_{\max} + I_{\min}}, \tag{3.11}$$

where $I_{\max}$ denotes the intensity of the adjacent maximum, is approximately unity for coherence lengths that are much larger than the pinhole distance. If the coherence length decreases, the visibility decreases considerably. This makes it possible to estimate the coherence length of the incident radiation.

If one places the double-pinhole in the reflexion off a liquid surface, it becomes possible to compare different sample liquids concerning their influence on the coherence of the radiation. For the measurements described in this section actually a double-mirror at grazing angle was used, which shows a diffraction pattern identical to a double-slit.

The experiment was performed at the energy-dispersive refraction (EDR) beamline at the BESSY-II synchrotron, using white radiation. This is a noticeable difference to the experiments performed at the ESRF, since here there is practically no longitudinal coherence. However, a small effective coherence length was achieved by analysing the scattered radiation using an energy-dispersive detector. This setup allows in principle for the measurement at several different scattering vectors at once. For example, X-ray reflectivities can not only be measured by varying the incident angle of the radiation, but also the energy [68].

3.2.2 Setup

Figure 3.14 outlines the setup of the experiment. The radiation source at the EDR beamline is a bending magnet, which means that nearly-white radiation was available for the measurements. The scattered intensity was detected by an energy-dispersive detector with a

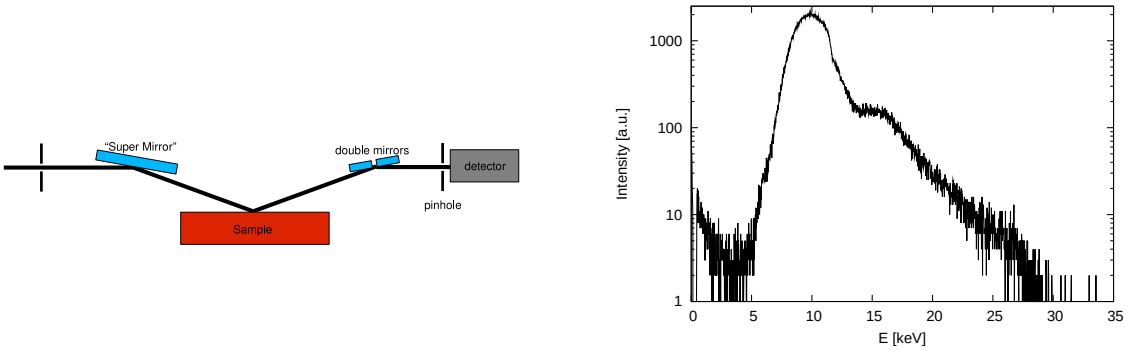

(a) Setup (b) Energy spectrum

Figure 3.14: Setup for energy-dispersive diffraction measurements. The radiation from the bending magnet is deflected downwards by the "super mirror" and hits the sample at a shallow angle. The reflected radiation hits a double-mirror, and the diffraction pattern is measured by the energy-dispersive detector. The right figure shows the energy spectrum from the super mirror (i.e., that hits the sample surface).

resolution of about 50eV, which corresponds to a logitudinal coherence length of about 12nm at 8keV.

The principle of the measurement is a variation of Young's double-slit experiment that had already been performed successfully before using white coherent X-rays [46]. This experiment was modified to incorporate scattering by a liquid surface. The white radiation was deflected downwards by an aperiodic multi-layer mirror called a "super mirror". The special structure of this device allows for high reflectivity values over large angle and energy ranges. One aspect of this experiment was to verify that the mirror could be used to deflect radiation of a wide energy range onto the sample surface. The resulting spectrum coming from the super mirror is shown in figure 3.14 on the right. The maximum intensity was measured at $\sim$ 10keV, with a usable range between 6keV and 25keV.

The radiation hit the sample at a shallow angle, and a double-mirror was placed into the reflexion. A double mirror at a shallow angle acts equivalently to a double pinhole with the effective pinhole distance

$$d \approx 2d' \cdot \alpha_m, \tag{3.12}$$

where d' is the mirror distance and α_m the incident angle on the mirror. The mirror produces a diffraction pattern that can be measured by the energy-dispersive detector. The result of such a measurement is shown in figure 3.15. The left shows the measured data by the detector

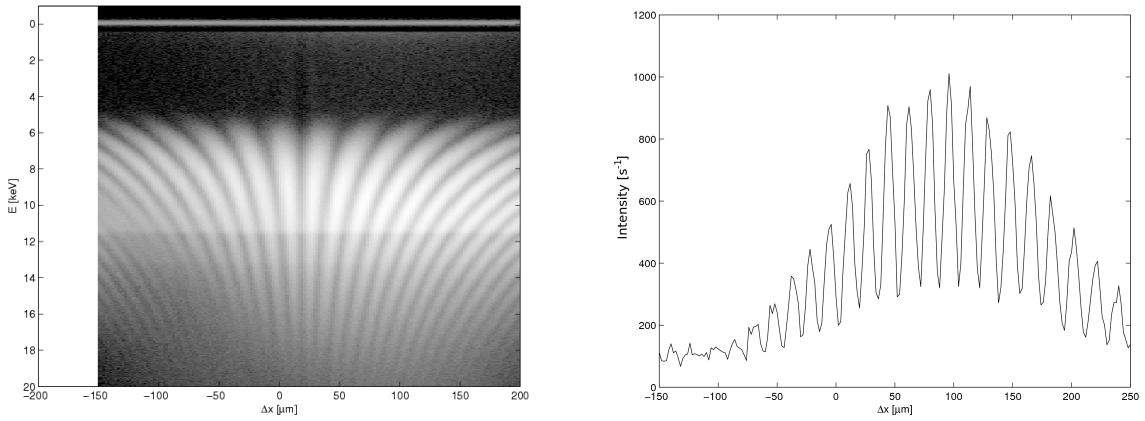

(a) Complete diffraction pattern (b) Cut at constant energy

Figure 3.15: Diffraction pattern produced by the double mirror. The left image shows a 2d map of the complete pattern as measured by the detector. The right image shows a cut at an energy $E = 12\text{keV}$.

in form of a 2d map. From those maps, diffraction patterns at a constant energy could be extracted, as is shown in figure 3.15 (b).

The visibility of the diffraction fringes is a measure for the coherence properties of the radiation. For large coherence lengths $\xi_t \to \infty$, the visibility approaches unity. When the coherence length is reduced, the visibility decreases as [46, 68]

$$V(\lambda) = \left| \frac{\sin\left(\frac{\pi L d}{\lambda D}\right)}{\frac{\pi L d}{\lambda D}} \right| = \left| \text{sinc}\left(\frac{d}{2\xi_t}\right) \right|, \tag{3.13}$$

where L is the size of the source, D the distance source – pinhole, d the pinhole distance and λ the wave length. $\text{sinc}(x) = \sin(\pi x)/(\pi x)$ denotes the sine cardinal function.

The visibility can also be expressed as a function of the photon energy:

$$\Rightarrow V(E) = \left| \text{sinc}\left(\frac{LdE}{hc\,D}\right) \right| =: \left| \text{sinc}\left(\frac{d}{2\zeta_t}E\right) \right|, \tag{3.14}$$

where h denotes the Planck constant and E the radiation energy. ζ is a parameter describing the coherence properties of the radiation. The energy dependence of the coherence length is given as as $\xi_t(E) = \zeta_t/E$. Previous measurements showed $\zeta_t \approx 100\mu\text{m keV}$ at the EDR beamline [46]. The incident angle on the double mirror was 0.05°, and the mirror distance 7mm. This leads to an effective pinhole distance of about 12μm. The measurement time is usually $\sim$ 1s per data point, yielding $\sim$ 3min for the complete diffraction pattern.

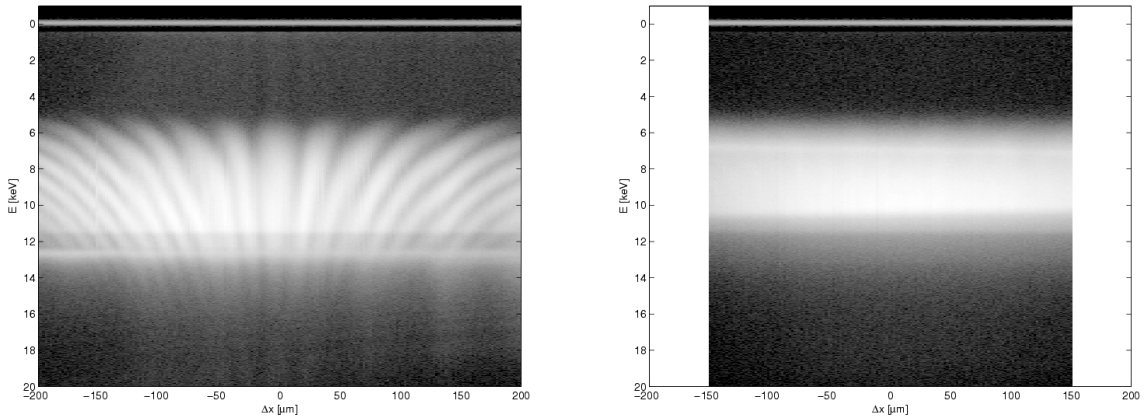

(a) PPG in the beam (b) N-hexane in the beam

Figure 3.16: Diffraction patterns measured in the specular reflexion. (a) shows the pattern of the PPG reflex. The visibility of the diffraction fringes is reduced, but the pattern is still visible. (b) shows the pattern of the hexane reflex. The diffraction pattern looks completely diffuse.

Glycerol, n-hexane and polypropylene glycol (PPG-3500) were used as sample liquids. The hexane used was produced by Fluka, and showed a purity of $\geq 99\%$. The glycerol was also produced by Fluka, while the PPG was produced by Aldrich.

3.2.3 Results

Figure 3.16 shows the patterns measured in the specular reflex of PPG-3500 and n-hexane. The reflex of a PPG surface does not destroy the visibility of the diffraction fringes, although the visibility is noticeably reduced. Glycerol behaves similarly. However, a surprising result was seen when n-hexane was used as sample liquid. The diffraction pattern vanished completely ($V = 0$), yielding a completely diffuse scattering pattern. The reason for this is not clear, as the sample liquid should not be able to destroy the coherence completely.

The results are summarised in table 3.17. As expected, the visibility decreases with increasing energy. The super mirror yields a slight decrease in visibility, and the sample liquids reduce it even further. The coherence parameters calculated from the data are summarised in table 3.2.

PPG has the strongest apparent influence on the visibility of the diffraction fringes, as the decrease is $\sim 30\%$. The results indicate that the actual sample seems to have an influence, as PPG reduces the visibility further than e.g. glycerol, and n-hexane seems to destroy the diffraction pattern completely. However, the reason for this is not clear. Both PPG and

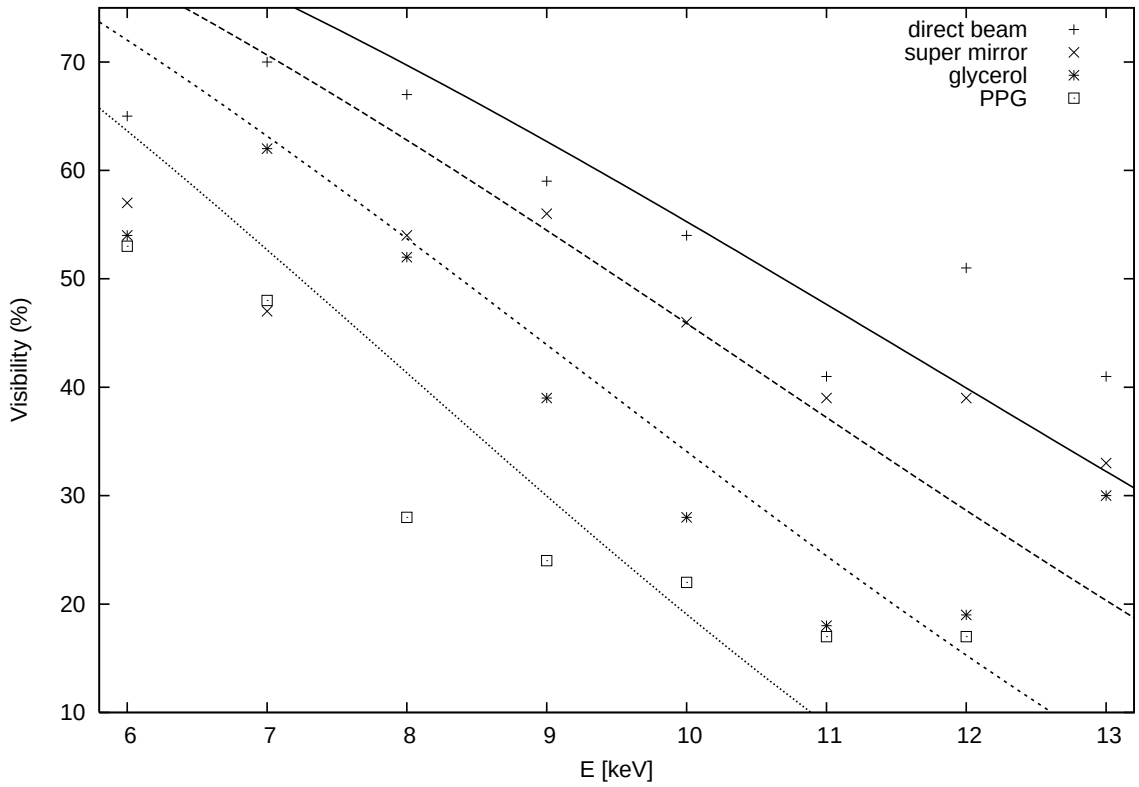

Figure 3.17: Visibility of the diffraction fringes. The lines are fits according to equation (3.14). The super mirror reduces the visibility slightly, and a liquid sample in the beam reduces it noticeably. PPG yields the strongest reduction of visibility ($\sim 30\%$).

	ζ_t [µm keV]	γ[mN/m]	η[mPas]
direct beam	106 ± 5	-	-
super mirror	95 ± 6	-	-
glycerol	83 ± 4	63	1 410
PPG-3500	72 ± 3	31	1 300
n-hexane	0	18	0.32

Table 3.2: Sample dependence of the transverse coherence length. It can be seen that any additional element in the beam reduces the coherence length of the radation. The influence is different for the individual samples. N-hexane destroyed the diffraction pattern completely. Also listed are the viscosity η and surface tension γ of the sample liquids. The PPG data was taken from [83], and the glycerol data from [18, 51]. The data for n-hexane is identical to tab. 3.1.

glycerol are highly viscous liquids, for example ($\eta_{\mathrm{ppg}} = 1300\mathrm{mPa\,s}$ and $\eta_{\mathrm{glyc}} = 1410\mathrm{mPa\,s}$). It is therefore unlikely that the diffraction pattern was smeared out by vibrations, although the beamline was not thermally stabilised. It seems that the sample decreases the effective distance to the source, thus decreasing the coherence length at the double-mirror.

It is possible that the reduction of the coherence length depends systematically on the fluid properties of the sample. Likely quantities are the surface tension and the viscosity of the liquid, although the current data is insufficient to verify this dependence. Therefore further systematic investigation is required. For example, mixtures of water with ethanol and water with glycerol provide the possibility to vary the surface tension and viscosity of the sample.

3.2.4 Summary

An energy-dispersive variation of Young's double-slit experiment was performed incorporating different liquid samples as an additional mirror. The coherence properties of the radiation were determined through the visibility of the diffraction fringes from a double-mirror.

It could be shown that the "super mirror" available at the EDR beamline can be used to deflect nearly-white radiation onto the sample surface. The device had little effect on the coherence properties of the radiation. Introducing a liquid sample as an additional mirror decreased the visibility of the fringes more strongly, indicating a reduced effective distance to the source. This reduction depended on the actual sample material used. N-hexane destroyed the diffraction fringes completely.

Therefore the scattering off a liquid surface seems to decrease the coherence length of the specular reflected radiation. This effect depends on the material used, although it is not clear if there is a functional dependency on a particular fluid property like the surface tension or the viscosity. In this context, further systematic investigation is necessary, e.g. on ethanol-water mixtures, since these allow to vary the surface tension over a wide range (see also section 3.1.3). On the other hand, the viscosity of the sample liquid can be tuned by using mixtures of water with glycerol [77].

3.3 Adsorbed alkane thin films

3.3.1 Introduction

Solid substrates exposed to a vapour atmosphere can attract gas molecules forcing the formation of a liquid film. In case of complete wetting the van der Waals interaction between solid and liquid determines the equilibrium thickness as well as the surface structure of the thin liquid films [25]. The background potential suppresses long-range correlations inducing a lower cut-off q_{vdW} of surface waves (see also eq. (2.108) in section 2.3.2). This cut-off is given by

$$q_{\mathrm{vdW}} \approx a/h^2 \tag{3.15}$$

with the film thickness h and a characteristic "healing length"

$$a = \sqrt{A_{\mathrm{eff}}/2\pi\gamma}, \tag{3.16}$$

which is of the order of $2-5$Å for most liquids (A_{eff} denotes the effective Hamaker constant and γ the surface tension).

At q-values below this cut-off the liquid surface contour is dominated by the substrate [6, 70] while for larger q-values the dynamic structure factor shows a q^{-2} dispersion typical for capillary waves. Surface sensitive X-ray scattering experiments have confirmed the theoretical predictions [17, 91, 92].

If the wetting is only partial, i.e. there are disjunct islands of sample material on the substrate, the dynamics and structure of the liquid surface are changed substantially. Partial wetting and dewetting has been mainly investigated in the case of polymer films, where the structures that form during dewetting have been studied e.g. using atomic force microscopy. In a previous X-ray scattering experiment, capillary waves have been found on thick dewetted polymer films. Thinner films in early stages of dewetting showed a peculiar exponential form of the height-height correlation function [93].

In this section, some results of scattering experiments on thin vapour-deposited alkane films will be discussed. The original purpose of the experiments was to study the influence of the film thickness on the capillary waves spectrum (see section 2.3.2). Another key aspect was the attempt to make use of heterodyne mixing in order to reach higher $q_{||}$ values and thus investigate smaller length scales.

For this purpose, grating structures were etched into the surface of some of the silicon substrates. The gratings produce intensity maxima which are evenly spaced in $q_{||}$. To minimise the influence of the grating on the film dynamics, a very shallow structure was used with a depth of only a few nanometers. The scattered intensity at these maxima superimposes with the diffuse scattering from the adsorbed film. If the illumination is coherent, one expects the grating peaks to be modulated by the scattering off the adsorbed film, leading to a speckled structure in the vicinity of the maximum. In this setup, the XPCS measurement therefore takes place close to a diffraction peak from the grating to yield a heterodyne correlation function. However, the studies showed some surprising results that indicate a partial wetting situation might have been the case, inhibiting the capillary modes at the surface.

3.3.2 Setup

A sample cell had been designed as part of experiments on thin vapour-deposited films performed before, and subsequently re-designed [24, 79]. Both versions of the cell incorporate a vacuum-tight body, in which a temperature-controlled substrate holder is situated. The substrate is cooled by means of a Peltier element, and the temperature is held constant using a heating foil and a Lakeshore 340 temperature controller.

This particular cooling method allows for very precise control, meaning that the temperature can be held constant within a few mK. The cell is filled with the sample gas, in this case n-hexane, yielding a very pure vapour atmosphere on top of the substrate. The actual thickness of the liquid film that is forming at the solid-gas interface can then be controlled by changing the substrate temperature.

Figure 3.18 shows the older cell design. The Sample material is prepared in a glass reservoir that is connected to the rest of the cell by a bellows valve. The substrate is placed inside a cylindric dome, allowing for a wide range of different scattering angles. The dome shown on the photograph is made of beryllium, which is transparent in the hard X-ray regime. In principle a better temperature stability can be achieved using the beryllium dome, since the uniform metal surface equalises the vapour temperature at the boundary. However, the practical gain proved to be negligible. Because of this and since beryllium is difficult to handle, another dome made of steel and featuring a polyimide (Kapton) window was used.

The scattering geometry is basically the same as the one used for the surface-XPCS experiments (see figure 2.6). In fact, a main part of the measurements was the attempt to measure the capillary wave spectrum of mesoscopic alkane films by means of surface-XPCS. The trough

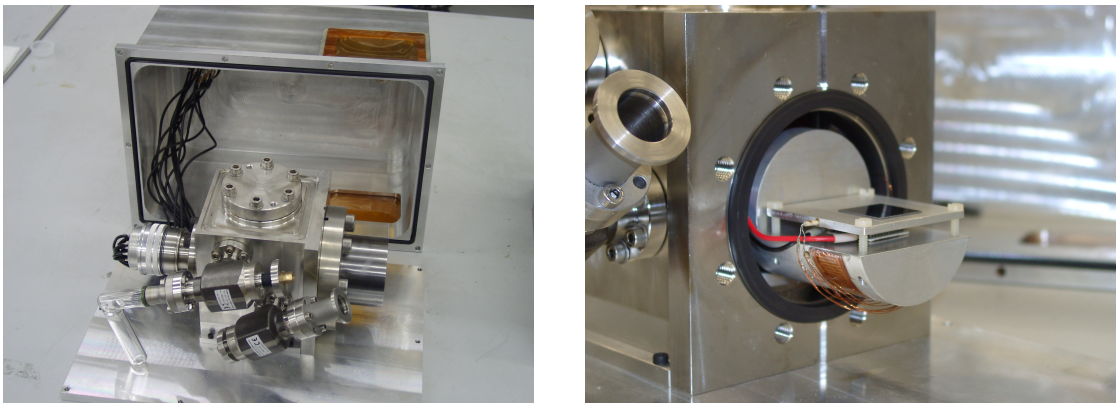

Figure 3.18: Sample cell for vapour-deposited thin-films. The right image shows a detailed view of the substrate holder; the heating foil and the Peltier element can be seen. The left image shows a total view of the cell, with the glass reservoir for the sample material on the left.

holding the liquid sample is replaced by the substrate in the cell. This adds an additional degree of freedom, since the influence of gravity forces is negligible for films < 100nm. This means that the sample cell can be tilted, making it possible to change the incident angle during the experiment. Therefore it is possible to measure e.g. X-ray reflectivities in order to determine the film thickness.

One group of substrates that were used for the measurements consisted of surface gratings. Those were made of silicon wafers that had been oxidised to a depth of $\sim 100\mu$m. Into that oxide film, shallow grooves had been etched, yielding a surface grating with a periodicity of 2μm and a height difference of ~ 10nm [87]. After the etching process, residues of photo resist were removed using a plasma cleaning process. Figure 3.19) shows a scanning electron microscopy (SEM) image of one of the gratings. The grooves are quite even and show only few defects. Directly prior to the measurements, the gratings were cleaned again using n-hexane.

The second group of substrates consisted of silicon dies cut in the (100) plane. Those were first cleaned using the well-established RCA-1 wafer cleaning method [39]. Directly before the measurement, they were cleaned again using n-hexane.

The glass reservoir was cleaned and filled with the sample liquid, evacuated to remove the air and then connected to the sample cell prior to the measurement. Afterwards the cell was "flushed" several times, in the sense that the sample cell was repeatedly evacuated to pressures below 1mbar and vapour was fed into the cell by opening the reservoir shortly. Directly prior to the measurement, the sample cell was evacuated to a pressure $< 10^{-4}$mbar, and then the reservoir was opened for a few seconds to fill the cell with vapour.

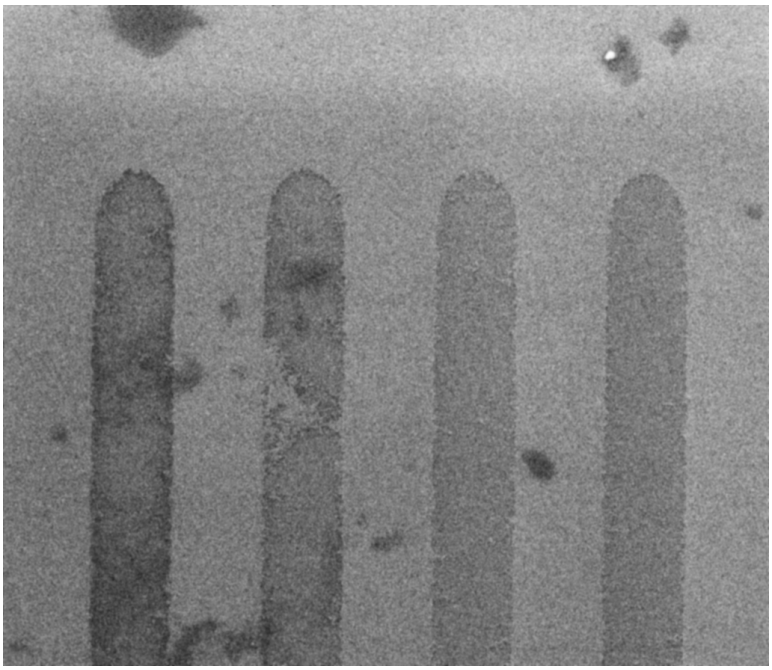

Figure 3.19: Scanning electron microscopy image of a SiO_2 surface grating. Depicted is the border of the grating area. Some defects can be seen, but overall the etched grooves are very even. The aspect ratio of the etched areas is very low.

The thickness of the film on the substrate was controlled by cooling and heating the substrate holder. It was measured by means of X-ray reflectivity, which also allowed to study the stability of the film. Film thicknesses from mono-layer coverage up to a few 100Å have been investigated. The films can easily be removed from the substrate by heating the film by a few °C.

3.3.3 Results

Since the original goal of this series of experiments was to determine the influence of the film confinement on the capillary wave spectrum, thin vapour-deposited films of n-hexane were to be examined by means of surface-XPCS. The viscoelastic formalism (section 2.3.2) predicts that even a low-viscosity sample should show overdamped waves if confined into a thin film. However, it should still show capillary waves dynamics that can be detected by means of XPCS.

The measurements on the SiO_2 gratings showed that they were of a very high quality. Eleven and more diffraction orders could be discerned (figure 3.20). Determining the thickness of an adsorbed film by means of X-ray reflectivity proved to be difficult due to the grating

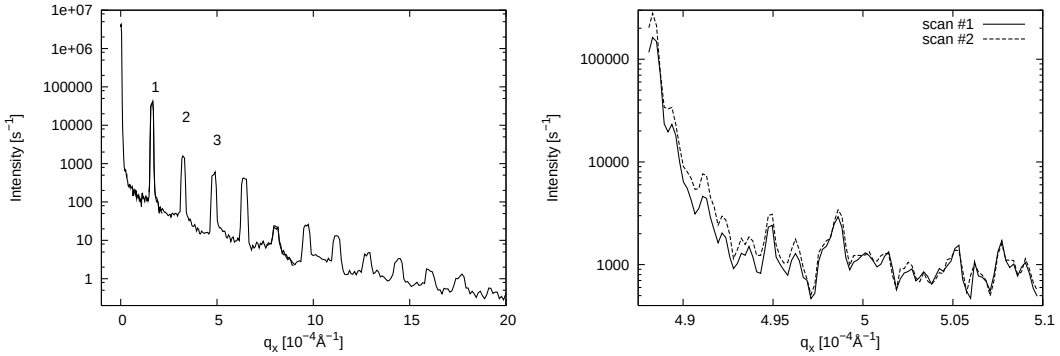

(a) Diffraction peaks (b) Speckles on 3rd order

Figure 3.20: Diffraction peaks from a SiO_2 grating. The incident angle on the sample was $\alpha_i \approx 0.18°$. 11 diffraction orders can be discerned. On the grating, a $\sim$ 100Å n-hexane film was adsorbed. The right image shows two scans of the diffuse scattering in direct vicinity of the third diffraction peak. The time between the two scans was $\sim$ 15min.

structure. Therefore the sample was moved perpendicular to the beam so that the radiation hit a smooth area, where then the reflectivity scan was performed.

Films with thicknesses up to a few 100Å were prepared. The Hamaker constant of n-hexane on silicon dioxide calculated according to equation (2.100) and based on the material values given in [16] is approximately $-5 \cdot 10^{-20}$J. This leads to a van der Waals cut-off (equation (2.108)) of $q_{\mathrm{vdW}} \approx 6.75 \cdot 10^{-4}\text{Å}^{-1}$ for a 100Å film. The investigated scattering vectors were of the order of 10^{-5}Å^{-1} and therefore smaller than the van der Waals cut-off.

However, in the viscoelastic formalism the structure factor $S(q)$ (equation (2.104)) is given as a Lorentzian and well defined for $q \to 0$. This means that q_{vdW} is not a cut-off in the sense that no surface dynamics is expected for $q < q_{\mathrm{vdW}}$, but only in the sense that the common q^{-2} dispersion of capillary waves is only observed for $q > q_{\mathrm{vdW}}$. Figure 3.21 shows the calculated structure factor for a 100Å thin n-hexane film on a silicon dioxide substrate according to equation (2.117). The spectrum is Lorentzian-like, with the maximum at $\omega = 0$. One therefore expects overdamped capillary waves.

The diffuse scattering in direct vicinity of a diffraction peak was investigated. However, XPCS measurements showed no dynamics from the film. In order to investigate why the thin films showed no capillary dynamics whatsoever during the first experiment, static diffuse scans were performed. These showed a distinct speckle structure, confirming that the scattered intensity was static. The speckle structure changed during film thickness changes and remained constant otherwise.

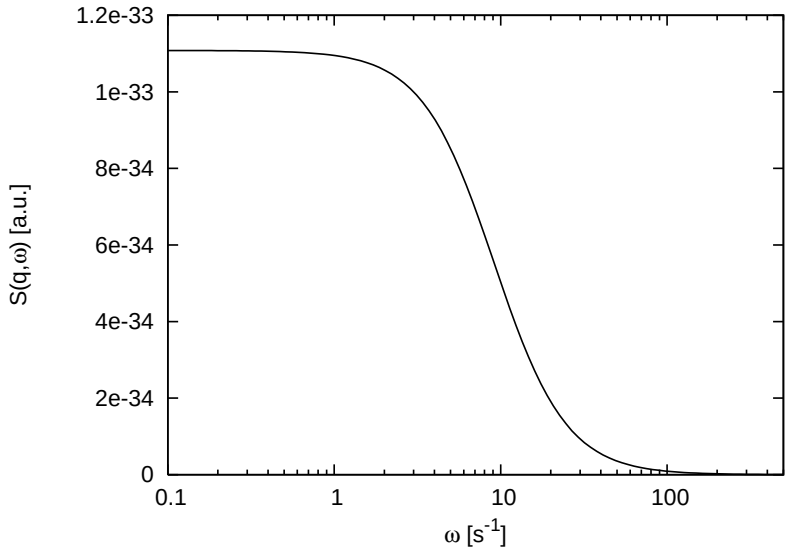

Figure 3.21: Dynamic structure factor calculation for a thin film. The figure shows the expected dynamic structure factor of a 100Å thin n-hexane film on a silicon dioxide substrate at $q = 10^{-5}\text{Å}^{-1}$ according to equation (2.117). The maximum of the spectrum is at $\omega = 0$, indicating overdamped capillary waves.

Figure 3.20 shows a scan of the diffuse scattering near the third diffraction order. The speckle structure is almost constant over a period of at least 15 minutes. The speckles appeared on top of the diffraction intensity. This means that gratings like the ones used here could in principle be used as a reference source for the purpose of heterodyne mixing in surface-XPCS. However, due to the apparent absence of capillary waves dynamics on the films no actual XPCS measurements could be performed.

The measurements on silicon dies yielded similar results. This means that the grating structure is not the reason for the static behaviour of the films. The presence of the films on the substrate was again verified by means of X-ray reflectivity. An example is shown in figure 3.22. The reflectivity profiles can be modelled reasonably well using a simple electron density profile, consisting of just one layer on top of a silicon substrate. However, different profiles produced inconsistent results. While e.g. the 43Å profile shown in figure 3.22 can be explained assuming a film density close to that of n-hexane ($\delta \approx 2.7 \cdot 10^{-6}$ at 8keV), the 181Å profile can only be modelled if the electron density of the film is assumed to be only 40% of that value. The film roughness is comparable in both cases ($\sim$ 6Å).

A more detailed analysis of a large number of reflectivity profiles taken later at the beamline "8ID" (APS, Argonne, USA) by C. Gutt et al. yielded that a simple density profile is often insufficient to explain the data [31]. A possible explanation, especially when taking into

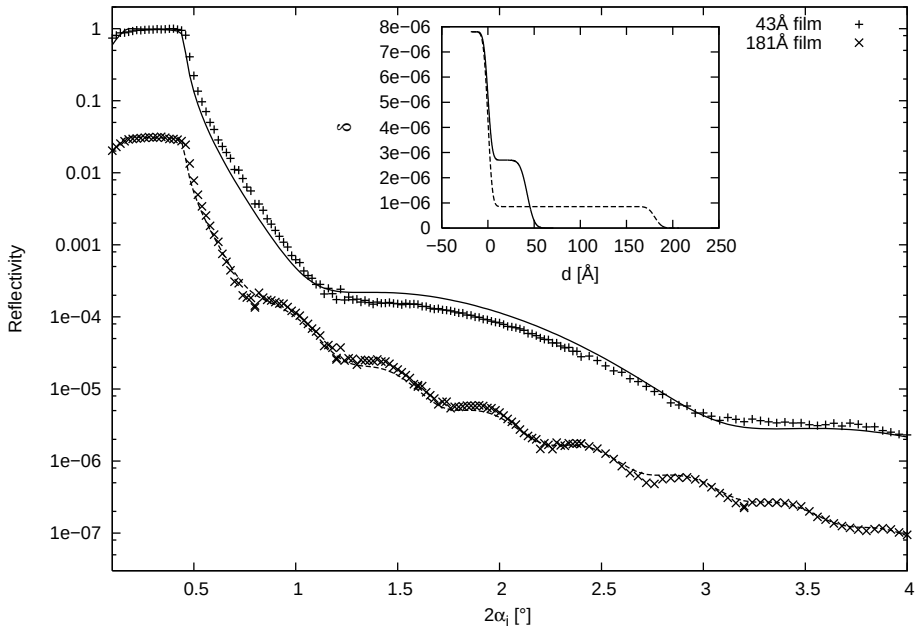

Figure 3.22: X-ray reflectivities of adsorbed hexane films. Also shown are theoretical curves based on a simple layer model. The inset shows the corresponding electron density profiles, in terms of the δ component of the index of refraction (see section A.1) at 8keV.

account the 181Å film shown before, is that the sample material is not completely wetting the substrate. XPCS measurements did not yield any surface dynamics on the accessible length scales ($\sim$ 100µm), supporting that conclusion. If the film is not laterally continuous, capillary waves are suppressed on length scales that are not significantly smaller than the mean island size.

The investigation of the diffuse scattering from the samples showed again a static speckle structure. The speckles changed during thickness changes and could therefore be attributed to the sample material. Figure 3.23 shows a representative set of rocking scans performed on a thin hexane film ($h \sim 50$Å). The scattered intensity shows a clear speckle structure. Furthermore, the speckle positions did not change between scans, yielding almost identical results in each measurement. Taking into account the measuring time ($\sim$ 5min), the sample appeared to be stable over a period of at least 15 minutes.

To answer the question if the observed speckle structure is indeed connected to the hexane sample and not just the wafer surface, measurements before and after hexane adsorption were taken, and also at different film thicknesses. The speckle structure seen in the scans

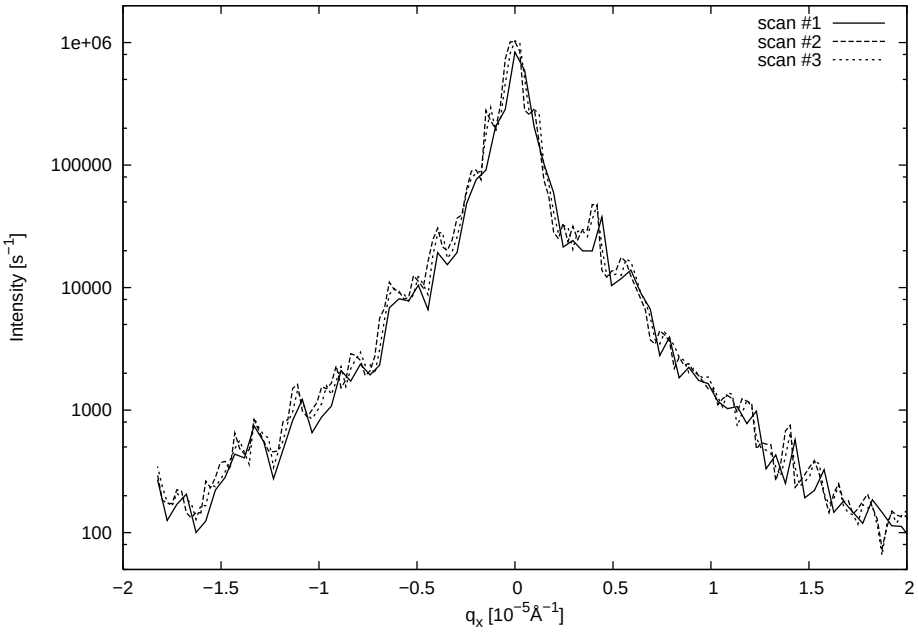

Figure 3.23: Coherent rocking scans of n-hexane adsorbed on silicon. The film thickness was ~ 50Å, and $q_z = 5.7 \cdot 10^{-2}$Å^{-1}. The three curves correspond to three consecutive scans with identical parameters. It can be seen that the speckle structure stays largely the same between scans.

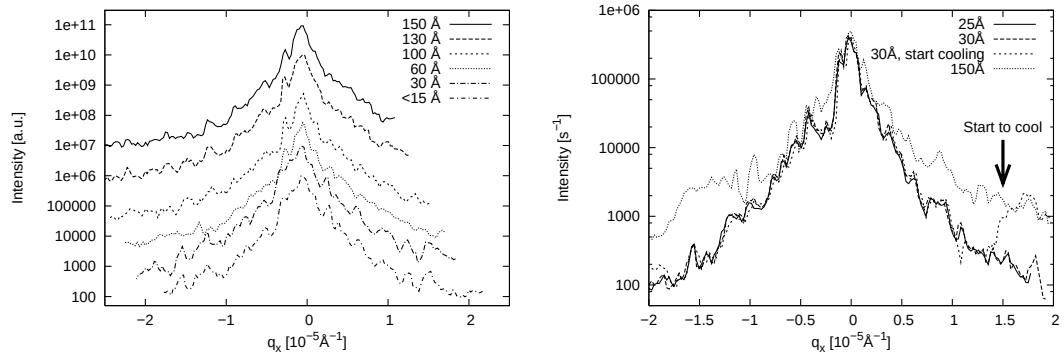

(a) slow condensation (b) rapid condensation

Figure 3.24: Influence of thickness changes on the speckle pattern. Shown are rocking scans at $q_z = 5.7 \cdot 10^{-2}$Å^{-1}. The left image corresponds to a slow condensation process, while the right one depicts rapid condensation. During slow condensation, the speckle patterns change only slowly. Rapid condensation produces a drastic change in the speckle pattern. The third scan on the right is a repetition of the second, where towards the end rapid growth of a ~ 150Å film was started. The starting point of the cooling procedure is marked. The fourth scan shows the 150Å film after stabilising.

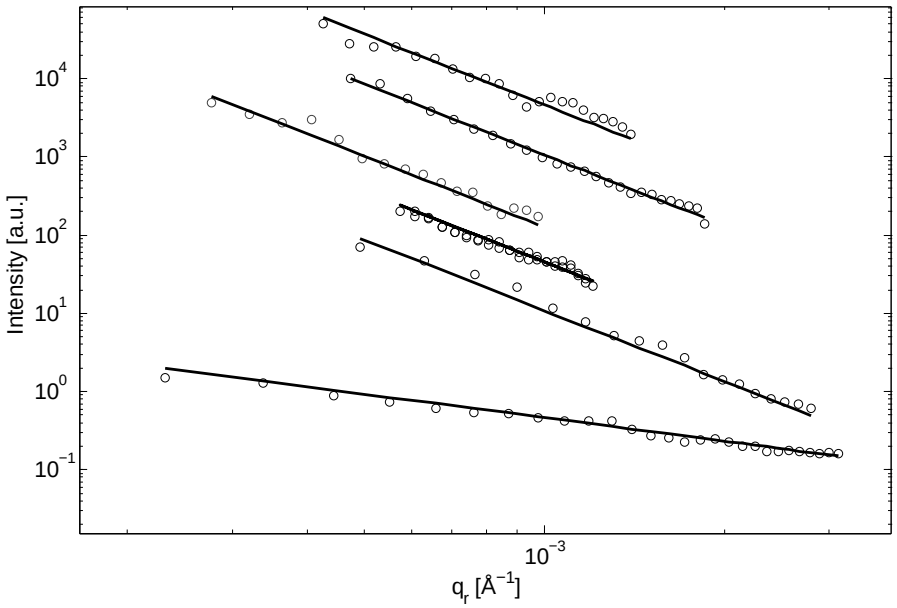

Figure 3.25: Diffuse scattering from n-hexane thin-films. Data taken at beamline "8ID", APS (Argonne/Chicago) [31]. The data sets correspond (from bottom to top) to the following film thicknesses: 60, 100, 300, 400, 500, 600Å. All scans except the 60Å show a clear q^{-3} behaviour, while the thinnest film shows a q^{-1} behaviour.

turned out to be a function of the film thickness and adsorption time (i.e. the temperature gradient during preparation).

Figure 3.24 shows consecutive rocking scans of growing films. On the left a series of slow thickness changes is shown. The speckle pattern changes slowly and consecutive scans show a clear relationship. The right subfigure shows a rapid condensation process. The first scan was taken at a thickness of $\sim$ 25Å, while the second corresponds to 30Å. Between those two scans the temperature of the substrate was decreased slowly. The speckle pattern is almost constant, meaning identical surface structures on the observed length scales. This indicates that the surface structure of very thin films is determined mostly by the substrate. The third scan is a repetition of the second, where towards the end rapid growth of a thicker film ($\sim$ 150Å) was started. As a consequence, the speckle pattern changes significantly, and the diffuse scattering intensity increases noticeably.

In addition to the speckle scans at ID10, measurements at 8ID yielded that the diffuse scattering of identically prepared n-hexane films shows a q^{-3} behaviour (figure 3.25), which corresponds to the exponential height-height correlation function proposed as a model for dewetting polymer films [31]. The only exception was a very thin film ($\sim$ 60Å), indicating a

possible crossover from q^{-3} to q^{-1} behaviour between 60 and 100Å which means that for low coverages, the surface structure is indeed determined entirely be the substrate.

The diffuse scattering of a self-affine surface is given by equation (2.20). It shows that the diffuse scattering of a sample can exhibit a q^{-3} behaviour if the surface is self-affine on the corresponding length scale [93]. On the other hand, a liquid surface covered by capillary waves shows a q^{-2} behaviour, as can be seen in equation (2.16).

It is therefore highly likely that the investigated hexane films actually were no films at all, and that the sample liquid was only partially wetting the silicon substrate. The diffuse scattering indicates a self-affine behaviour rather than capillary waves roughness, which would also explain why no surface dynamics could be observed using surface-XPCS. The measured speckle patterns probably correspond to the lateral structure of individual wetting areas.

3.3.4 Summary

Hexane thin films adsorbed on silicon substrates have been investigated using surface-sensitive X-ray scattering techniques. The scattering revealed no dynamics in XPCS measurements. Coherent scans of the diffuse scattering revealed a static speckle structure.

Surface gratings etched into oxidised silicon wafers were also used as substrates. The gratings showed clear and pronounced diffraction orders. Near a diffraction order the diffuse scattering showed speckles, meaning that the diffuse scattering from the adsorbed film and the diffraction from the grating superimposed. This indicates that XPCS measurements with heterodyne mixing should be possible using this setup.

The measured speckle structures could be attributed to the adsorbed sample layer, as it changed noticeably during thickness changes. However, if the sample temperature (and therefore film thickness) was held constant, the speckle pattern remained unchanged over prolonged periods of time ($\geq$ 15min).

The thickness of the adsorbed films on the wafer substrates has been verified with X-ray reflectivity using the same setup. An analysis of the reflectivity data indicates that a simple, smooth layer model is not sufficient to describe the data in a satisfying way. At least one reflectivity curve can be described best assuming a layer of drastically reduced electron density, supporting the conclusion that the sample material was not completely wetting the substrate.

The results are in agreement with those of additional experiments on the same system [31]. There, the diffuse scattering intensity has been extracted from CCD data, revealing a q^{-3} behaviour. This can be explained assuming an exponential height-height correlation function characteristic for solid surfaces. The same behaviour has already been observed on partially dewetted polymer films [93]. Therefore a possible explanation for the observed behaviour is that the sample was only partially wetting the substrate, forming droplets and "islands" of liquid material which effectively suppress capillary dynamics on the corresponding length scales.

4 Summary and Outlook

Surface-sensitive XPCS measurements on n-hexane, water and mixtures of water with ethanol have been performed and analysed. It has been shown that the results cannot be interpreted correctly without taking a finite experimental resolution into account. A simplified formalism has been proven to be useful in both the description and analysis of the data, making it possible to indirectly measure the resolution function of the setup as a fit parameter during a reference measurement. The resulting values can then be used to correctly interpret the data of the actual sample.

It has been shown that finite experimental resolution is a possible explanation for the effect of intrinsic heterodyne mixing. The effective resolution showed a slight dependence on the sample, which caused the change of the detected correlation function from homodyne to heterodyne.

A promising modification in the form of a Fresnel zone plate has been tested, which resulted in a noticeable increase in the maximal q_x vector that could be reached. Furthermore, non-intrinsic heterodyne mixing has been observed at least once, and with very good signal-to-noise ratio. First tests to implement systematic heterodyne mixing in XPCS have also been performed. It could be shown that it is possible to deflect a part of the specularly reflected radiation towards the detector using a diffraction grating.

Since the scattering off a liquid surface seemed to decrease the coherence length of the specular reflected radiation, an energy-dispersive variation of Young's double-slit experiment was performed incorporating different liquid samples as an additional mirror. The coherence properties of the radiation were determined through the visibility of the diffraction fringes from a double-mirror. A dependence of the coherence length on the material used was observed, although the data so far is not sufficient to prove a functional dependency on a particular fluid property like the surface tension or the viscosity. In this context, further systematic investigation is necessary, e.g. on mixtures of water with ethanol and water with glycerol, since these provide the possibility to vary the surface tension and viscosity of the sample over a wide range.

In an additional experiment, hexane thin films adsorbed on silicon wafer substrates and surface gratings have been investigated using surface-sensitive X-ray scattering techniques. The gratings showed clear and pronounced diffraction orders. Near a diffraction order the diffuse scattering showed speckles, meaning that the diffuse scattering from the adsorbed film and the diffraction from the grating superimposed. This indicates that XPCS measurements with heterodyne mixing should be possible using this setup. The measured static speckle structures could be attributed to the adsorbed sample layer, as it changed noticeably during thickness changes.

The results of the measurements on silicon wafers are consistent with the grating results. Coherent scans of the diffuse scattering yielded again a static speckle structure. The results are in agreement with those of additional experiments on the same system [31]. There, the diffuse scattering intensity revealed a q^{-3} behaviour. This was explained assuming an exponential height-height correlation function characteristic for solid surfaces, as has already been observed on partially dewetted polymer films [93]. Therefore a possible explanation for the observed behaviour is that the sample was only partially wetting the substrate, forming droplets and "islands" of liquid material which effectively suppress capillary dynamics on the corresponding length scales.

In summary, three applications of coherent X-ray scattering methods to soft-matter systems have been presented and discussed. X-rays are especially useful on those systems since other techniques like e.g. scanning microscope techniques are generally not able to investigate the structure and dynamics of liquid systems. Another advantage is the surface sensitivity due to the effect of total external reflexion. However, the observed influence of the sample material on the experimental resolution and coherence lengths requires further investigation.

A Appendices

A.1 X-ray reflectivity

In this section, a few aspects of X-ray reflectivity measurements will be recapitulated. X-ray reflectivity has been used as a supporting technique during the measurements on thin adsorbed hexane films in order to estimate the thickness of the film on the substrate.

In reflectivity measurements, the incident angle α_i and the detection angle α_f are equal (see figure A.1). This means that the wave vector transfer $\vec{q}$ is perpendicular to the surface, and a reflectivity scan yields only information on the structure of the sample that has been laterally averaged.

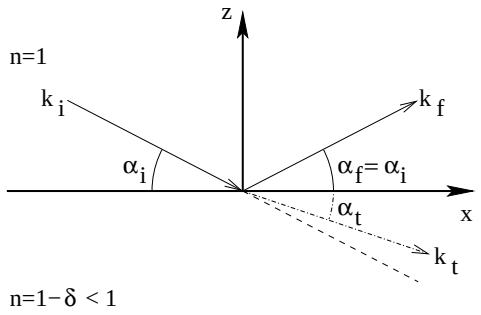

Figure A.1: Schematic representation of the scattering geometry in an X-ray reflectivity setup. Part of the incident wave is transmitted into the sample at the angle α_t, while the other is reflected ($\alpha_f = \alpha_i$).

Reflectivity scans are best suited for smooth and planar samples with small roughness values ($\sim$ 10Å or smaller), like e.g. surfaces of liquids, polished and/or varnished surfaces and thin organic films on smooth substrates. The latter case applies to polymer films on silicon, for example [86], and to thin adsorbed alkane films as well. Both have been subject to theoretical and experimental investigations in the past [31, 40].

Index of refraction in the case of X-rays

In this section the index of refraction in the X-ray case is introduced, which allows a treatment of X-ray reflectivity using optics formulae. Inhomogeneities of the sample material are neglected. Furthermore, it is assumed to be isotropic and non-magnetic. In this case, the spatial propagation of the electric field in matter is described by the Helmholtz equation [8]

$$\Delta\vec{E}(\vec{r},\omega) + k^2 n^2(\vec{r},\omega)\vec{E}(\vec{r},\omega) \quad = \quad 0, \tag{A.1}$$

where $n(\vec{r},\omega)$ is the refractive index at location $\vec{r}$ and frequency ω, representing the optical characteristics of the scattering material. In general, the index of refraction for N atoms per unit volume is given in the Drude model as [35, 37]

$$n^2(\vec{r},\omega) \quad = \quad 1 + N\frac{e^2}{\epsilon_0 m}\sum_{j=1}^{N}\frac{f_j}{\omega_j^2 - \omega^2 - 2\mathrm{i}\omega\eta_j}, \tag{A.2}$$

which describes each atom as a harmonic oscillator with resonance frequency ω_j. e is the elemental charge, m the mass of an electron and ϵ_0 the vacuum permittivity. The η_j denote damping factors, while the f_j describe the forced oscillation strengths of the electrons of each single atom:

$$f_j \quad = \quad f_j^0 + f_j'(\omega) + \mathrm{i}f_j''(\omega), \tag{A.3}$$

with $f_j'(\omega)$ and $f_j''(\omega)$ taking into account the frequency-dependant dispersion and absorption of the material.

In the case of X-rays, equation (A.2) simplifies into [92]

$$n(\vec{r},\omega) \quad = \quad 1 - \delta(\vec{r},\omega) + \mathrm{i}\beta(\vec{r},\omega) \tag{A.4}$$

with

$$\delta(\vec{r},\omega) \quad = \quad \frac{2\pi c^2}{\omega^2} r_e\,\rho(\vec{r})\sum_{j=1}^{N}\frac{f_j^0 + f_j'(E)}{Z} \tag{A.5}$$

and

$$\beta(\vec{r},\omega) \quad = \quad \frac{2\pi c^2}{\omega^2} r_e\,\rho(\vec{r})\sum_{j=1}^{N}\frac{f_j''(E)}{Z} = \frac{\lambda}{4\pi}\mu(\vec{r}) \tag{A.6}$$

being real and positive numbers. r_e denotes the classical electron radius or Thompson scattering length of the electron, $\rho(\vec{r})$ the electron density, Z is the total number of electrons and $\mu(\vec{r})$ a linear absorption coefficient. For small $\vec{q}$, the refractive index can be expressed as

$$n(\vec{r},\omega) = 1 - \frac{2\pi c^2}{\omega^2} r_e \rho(\vec{r}) + \mathrm{i}\frac{c}{2\omega}\mu(\vec{r}). \tag{A.7}$$

For a photon energy of e.g. $\sim$ 8keV, the value of δ is usually of the order of $10^{-5} - 10^{-6}$. Furthermore, for the materials investigated in the context of this thesis, the absorption coefficient μ can be neglected.

Since the real part of n is slightly smaller than 1, one observes total external reflexion below a special incident angle, which is called the critical angle of total external reflexion α_c of the material. Since $\delta \ll 1$, the following useful approximation holds:

$$\alpha_c \approx \sqrt{2\delta}. \tag{A.8}$$

For incident angles smaller than α_c, the X-rays do not penetrate deeply into the medium, and form a so-called evanescent (i.e., non-propagating) mode perpendicular to the surface. In the case of hard X-rays, the critical angle is usually $\alpha_c < 1^\circ$. The standard energy for the experiments presented in this thesis was 8keV. At this energy, which is approximately the energy of the copper K_α emission line at a wave length $\lambda \approx 1.54$Å, the critical angle e.g. of silicon is $\sim 0.22^\circ$, and of water $\sim 0.15^\circ$.

Single, smooth surface

The most simple case is the one of a single, smooth surface. Here, the reflected and transmitted parts of the incident wave can be described by the Fresnel equations. The corresponding reflexion and transmission coefficients in this case are [35]

$$r = \frac{k_{i,z} - k_{t,z}}{k_{i,z} + k_{t,z}}$$

$$\text{and } t = \frac{2k_{i,z}}{k_{i,z} + k_{t,z}} \tag{A.9}$$

$$\text{with } k_{i,z} = k\sin\alpha_i \quad \text{and} \quad k_{t,z} = nk\sin\alpha_t = k\sqrt{n^2 - \cos^2\alpha_i}. \tag{A.10}$$

Since $n \approx 1$ for hard X-rays, the influence of polarisation is very small and will be neglected [92].

The intensity $R_F = |r|^2$ of the reflected wave or Fresnel reflectivity in the small-angle case is then given by

$$R_F = \frac{(\alpha_i - p_+)^2 + p_-^2}{(\alpha_i + p_+)^2 + p_-^2} \tag{A.11}$$

$$\text{with } p_\pm = \sqrt{\frac{1}{2}\left[\sqrt{(\alpha_i^2 - \alpha_c^2)^2 + 4\beta^2} \pm (\alpha_i^2 - \alpha_c^2)\right]}. \tag{A.12}$$

The $p_\pm$ are the real and imaginary part of the complex transmission angle: $\alpha_t = p_+ + \mathrm{i}p_-$.

Roughness

The case of an ideally-smooth surface is actually an oversimplification, since all real surfaces and interfaces show finite roughness. Roughness essentially means that the actual vertical interface position h is a function of the lateral coordinates, i. e. $h = h(x, y)$. The precise form of $h(x, y)$ is system-dependent. In the case of many solids, $h(x, y)$ can be described based on self-affine fractal functions [85].

Since a reflectivity measurement averages the index of refraction over a large surface area, the main consequence of roughness is that the mean transverse profile of the index of refraction $n(z)$ is no longer a step-function as in the smooth case, but becomes continuous. We assume that the local index of refraction $n(x, y, z)$ can still be described by a step function at the local height $h(x, y)$, with the values $n_1 = 1$ above $h(x, y)$ and $n_2 = n$ below $h(x, y)$:

$$n(x, y, z) = \Theta(z - h(x, y)) + n\Theta(h(x, y) - z) \tag{A.13}$$

The laterally averaged index of refraction $\bar{n}(z)$ is then given by

$$\bar{n}(z) = \iint n(x, y, z)\, \mathrm{d}x\, \mathrm{d}y. \tag{A.14}$$

Due to the averaging process, the rough surface can therefore be replaced by an assembly of smooth surfaces at different heights z, weighted by a probability density $P(z)$ with a mean value $\bar{z} = \int z\, P(z)\mathrm{d}z = 0$ and a root-mean-square (RMS) roughness

$$\sigma^2 = \int z^2\, P(z)\mathrm{d}z. \tag{A.15}$$

One can then calculate the reflexion and transmission coefficients as [92]

$$\begin{aligned} \tilde{r} &= \frac{f(k_{t,z}+k_{i,z})}{f(k_{t,z}-k_{i,z})}\cdot r \\ \text{and } \tilde{t} &= \frac{1}{f(k_{t,z}-k_{i,z})}\cdot t \end{aligned} \tag{A.16}$$

with r, t being the Fresnel coefficients of a smooth surface, and f defined as

$$f(k) = \int \mathrm{e}^{-\mathrm{i}kz}\, P(z)\,\mathrm{d}z. \tag{A.17}$$

Assuming e.g. a Gaussian probability density

$$P(z) = \frac{1}{\sqrt{2\pi}\sigma}\exp\left(-\frac{z^2}{2\sigma^2}\right), \tag{A.18}$$

the refractive-index profile is then given as

$$n(z) = \frac{1+n}{2} - \frac{1-n}{2}\,\mathrm{erf}\left(\frac{z}{\sqrt{2}\sigma}\right) \tag{A.19}$$

with the error function erf(), yielding [92]

$$\begin{aligned} \tilde{r}_{\text{Gauss}} &= r\,\mathrm{e}^{-2k_{i,z}k_{t,z}\sigma^2} \\ \text{and } \tilde{t}_{\text{Gauss}} &= t\,\mathrm{e}^{(k_{i,z}-k_{t,z})^2\sigma^2/2} \end{aligned} \tag{A.20}$$

as modified reflexion and transmission coefficients. For very small roughnesses $\sigma \to 0$, the refractive-index profile takes again the form of a step function and $\tilde{r} \to r$ and $\tilde{t} \to t$.

Multiple interfaces

In this section, the reflectivity of a layer system is considered. Since interfacial roughness merely leads to a modification of the Fresnel coefficients, both the case of smooth and rough interfaces can be treated in an identical way. However, one should note that this is true only if all interfaces can be treated individually. This is equivalent to the condition that the interfacial roughnesses σ_i are significantly smaller than the layer thicknesses l_i.

Figure A.2 shows a stratified system containing several interfaces, numbered 1 to N. The first interface is located between the vacuum and the topmost layer, while the last interface lies between the lowest layer and the substrate. The substrate or layer $N+1$ is considered to

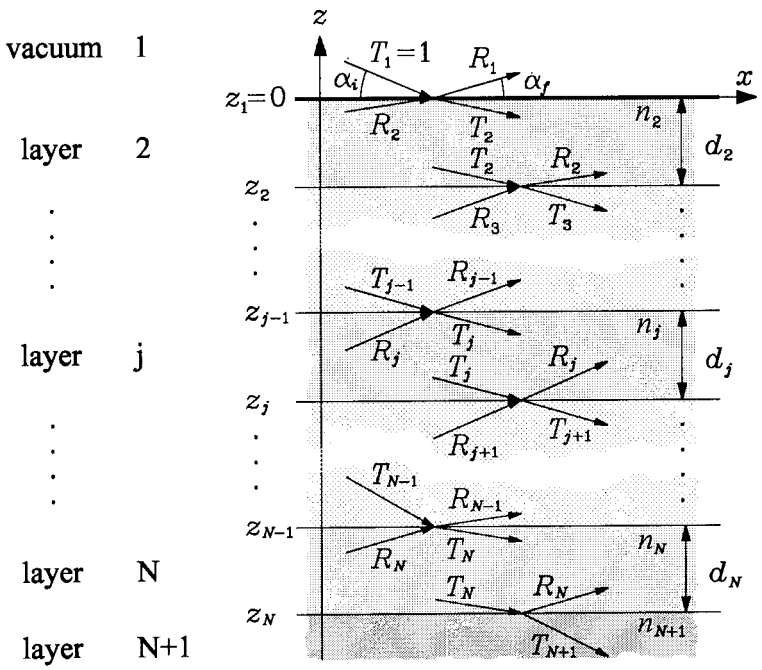

Figure A.2: X-ray reflexion of a system containing multiple interfaces. Presented is a system containing N interfaces, with the "layers" 1 and $N+1$ representing the outer vacuum and the substrate, respectively. Image taken from [92].

be semi-infinite; thus no part of the radiation transmitted into the substrate contributes to the reflexion off interface N.

For each of the other interfaces, both the reflected and transmitted fraction have to be taken into account, since e.g. the radiation transmitted into layer i hits the interface below, where a part is reflected backwards and another is transmitted into the layer $i+1$, and so on. All those fractions have to be added taking into account phase shifts at the interfaces, finally yielding the reflectivity of the surface. The actual calculation is commonly done using the recursive so-called Parratt algorithm [63]. This algorithm is well-documented and there are several software implementations available [10, 76]. Another, equivalent approach by Abelès uses transfer matrices and is even older [1].

In the following the Parratt approach will be presented in more detail. It is implemented by the `LSFIT` software [76] which was used to analyse the reflectivity data in the presented experiments. Neglecting roughness, the ratio of reflexion R_j to transmission T_j at interface j is expressed in terms of the underlying interface $j+1$ as

$$X_j = \frac{R_j}{T_j} = \mathrm{e}^{-2\mathrm{i}k_{z,j}z_j}\frac{r_{j,j+1}+X_{j+1}\mathrm{e}^{2\mathrm{i}k_{z,j+1}z_j}}{1+r_{j,j+1}X_{j+1}\mathrm{e}^{2\mathrm{i}k_{z,j+1}z_j}}. \tag{A.21}$$

Here

$$r_{j,j+1} = \frac{k_{z,j} - k_{z,j+1}}{k_{z,j} + k_{z,j+1}} \tag{A.22}$$

denotes the Fresnel coefficient of interface j (see also e.q. (A.9)), and $k_{z,j} = k\sqrt{n_j^2 - \cos^2(\alpha_i)}$ the z component of the wave vector in layer j. Since the substrate is assumed to be significantly thicker than the penetration depth of the radiation, $X_{N+1} = 0$ terminates the recursion. The specular reflectivity is then

$$R = |R_1|^2 = |X_1|^2. \tag{A.23}$$

If one takes into account a small finite interfacial roughnesses, the result presented above is still valid if one modifies the Fresnel coefficients analogous to e.g. (A.16):

$$\begin{aligned} \tilde{r}_{j,j+1} &= \frac{f(k_{z,j+1} + k_{z,j})}{f(k_{z,j+1} - k_{z,j})} \cdot r_{j,j+1} \\ \text{and } \tilde{t}_{j,j+1} &= \frac{1}{f(k_{z,j+1} - k_{z,j})} \cdot t_{j,j+1}, \end{aligned} \tag{A.24}$$

which leads in the case of a Gaussian probability distribution to a result very similar to (A.20):

$$\begin{aligned} \tilde{r}_{j,j+1\text{Gauss}} &= r_{j,j+1}\, \mathrm{e}^{-2k_{z,j}k_{z,j+1}\sigma_j^2} \\ \text{and } \tilde{t}_{j,j+1\text{Gauss}} &= t_{j,j+1}\, \mathrm{e}^{(k_{z,j}-k_{z,j+1})^2\sigma_j^2/2}. \end{aligned} \tag{A.25}$$

Figure A.3 shows a simple example for the reflectivity of stratified media. Here, the reflectivity of a smooth layer on top of a smooth substrate with higher electron density is shown. Adsorption effects have also been neglected. The reflectivity is unity for incident angles $\alpha_i < \alpha_c$, and then drops steeply for larger angles. While a single surface is described well by the Fresnel reflectivity, the layer introduces oscillations in the specular intensity, whose periodicity is given by [92]

$$\Delta q_z = \frac{2\pi}{l}, \tag{A.26}$$

in terms of the perpendicular wave vector transfer q_z and the layer thickness l.

If one introduces roughness, the reflected intensity for angles $\alpha_i \gg \alpha_c$ is decreased significantly (figure A.4). Furthermore, the visibility of the oscillations is decreased. Introduction

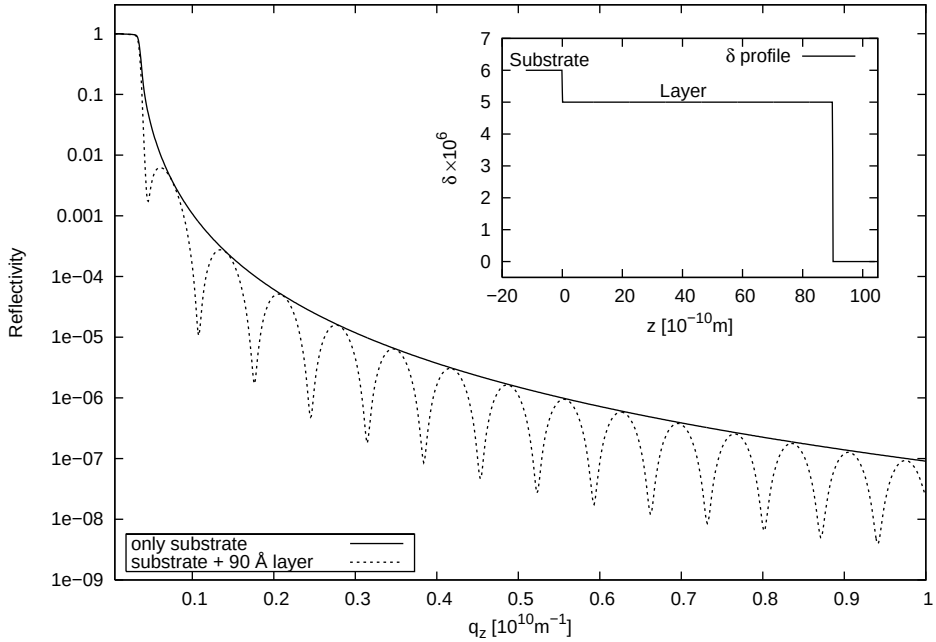

Figure A.3: Calculated reflectivity of a fictitious 90Å layer system. The layer is positioned on top of a substrate of higher electron density (see inset). The reflectivity shows clear oscillations (dashed line); the solid line marks the fresnel reflectivity of the substrate without any layer.

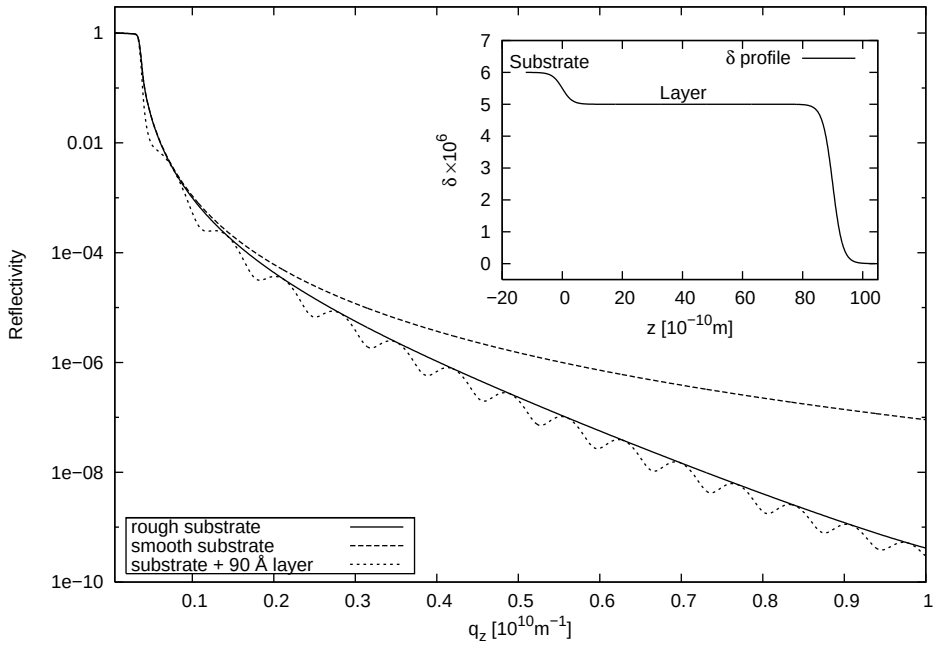

Figure A.4: Calculated reflectivity of a layered system including roughness. The parameters are the same as in figure A.3, but this time introducing roughnesses of 3Å for both substrate and layer. The Fresnel reflectivity of the smooth substrate is shown as reference.

of additional layers leads to a significantly more complex reflectivity, due to the coherent interaction between the individual layer signals.

If one considers a liquid surface covered by capillary waves, the error function erf() in equation (A.19) has to be replaced by a tanh() function. However, the differences between the two cases are small, and thus the Gaussian result is still valid as an approximation.

One should note that in general the density profile cannot be determined from the reflectivity in an unambiguous way. This is due to the well-known phase problem in scattering techniques: the scattered electrical field is connected to the sample structure by means of a Fourier transform. Since one can only measure the intensity of the field the phase information is lost, which means that the sample structure cannot be directly reconstructed from the measured data. The usual approach is therefore to formulate a model of the measured sample system that can be described by as few parameters as possible (e.g. electron densities, thicknesses and roughnesses of layers) and then use a least-squares optimiser to find the best-fitting set of parameters. This approach usually works quite well, at least for simple systems.

A problematic case is the case of large roughnesses, i. e. when the inequality $\sigma_i \ll l_i$ no longer holds. In this case the layers can no longer be treated individually, and the simple treatment presented here breaks down. Fortunately one can still use the Parratt formalism, by means e.g. of the so-called effective density description [92]. However, it will not be described in detail here, since X-ray reflectivity plays rather the role of a supporting technique in the experiments presented in this work, and the `LSFIT` software [76] directly supports this model.

A.2 Dynamics of a liquid film of arbitrary depth: viscoelastic theory (complete calculation)

In this section, the calculation leading to the results of section 2.3.2 will be derived in a more complete form. Following linear response theory, the power spectrum is connected to the liquid's dynamic susceptibility $\chi_{zz}(|\vec{k}|,\omega)$ (corresponding to a vertical surface displacement u_z) by [33]

$$S(\vec{k},\omega) = \frac{2k_BT\,\Im(\chi_{zz}(k,\omega))}{\omega}, \tag{A.27}$$

where k_B denotes Boltzmann's constant and T is the liquid's temperature. The dynamic susceptibility $\chi_{zz}(k,\omega)$ marks the ratio of the vertical displacement u_z of the surface to an external pressure P_z (comparable to a spring constant).

To calculate χ_{zz}, one makes an ansatz for monochromatic plane waves

$$\vec{v}(\vec{r},t) = (\bar{v}_x(z)\hat{e}_x + \bar{v}_z(z)\hat{e}_z)\exp[\mathrm{i}(kx-\omega t)] \tag{A.28}$$

$$P(\vec{r},t) = \bar{P}(z)\exp[\mathrm{i}(kx-\omega t)] \tag{A.29}$$

to find a solution for the velocity $\vec{v}$ and pressure P in the linearised Navier-Stokes equation

$$\frac{\partial}{\partial t}\vec{v} = -\frac{1}{\rho_m}\nabla P + \nu\Delta\vec{v}, \tag{A.30}$$

where $\nu = \eta/\rho_m$ denotes the kinematic viscosity of the liquid and ρ_m its density. The liquid is assumed to be incompressible, i. e., $\rho_m = \text{const}$. Inserting (A.28) and (A.29) into (A.30)

$$\begin{aligned} -\mathrm{i}\omega\begin{pmatrix}\bar{v}_x(z)\\0\\\bar{v}_z(z)\end{pmatrix}\exp[\mathrm{i}(kx-\omega t)] = \Bigg[\nu\begin{pmatrix}\partial^2/\partial z^2\bar{v}_x(z)-k^2\bar{v}_x(z)\\0\\\partial^2/\partial z^2\bar{v}_z(z)-k^2\bar{v}_z(z)\end{pmatrix} \\ -\frac{1}{\rho_m}\begin{pmatrix}\mathrm{i}k\bar{P}(z)\\0\\\partial/\partial z\bar{P}(z)\end{pmatrix}\Bigg]\exp[\mathrm{i}(kx-\omega t)] \end{aligned} \tag{A.31}$$

yields the following conditions [33]:

$$-\mathrm{i}\omega\bar{v}_x(z) = \nu\left(\partial^2/\partial z^2 - k^2\right)\bar{v}_x(z) - \frac{\mathrm{i}k\bar{P}(z)}{\rho_m} \tag{A.32}$$

$$\text{and } -\mathrm{i}\omega\bar{v}_z(z) = \nu\left(\partial^2/\partial z^2 - k^2\right)\bar{v}_z(z) - \frac{\partial/\partial z\bar{P}(z)}{\rho_m}. \tag{A.33}$$

By eliminating the pressure dependence

$$-\mathrm{i}\omega\partial/\partial z\bar{v}_x(z) = \nu\left(\partial^2/\partial z^2 - k^2\right)\partial/\partial z\bar{v}_x(z) - \frac{\mathrm{i}k\partial/\partial z\bar{P}(z)}{\rho_m} \tag{A.34}$$

$$-k\omega\bar{v}_z(z) = -\mathrm{i}k\nu\left(\partial^2/\partial z^2 - k^2\right)\bar{v}_z(z) + \frac{\mathrm{i}k\partial/\partial z\bar{P}(z)}{\rho_m} \tag{A.35}$$

$$\Rightarrow -\mathrm{i}\omega\left[\partial/\partial z\bar{v}_x(z) - \mathrm{i}k\bar{v}_z(z)\right] = \nu\left(\partial^2/\partial z^2 - k^2\right)\left[\partial/\partial z\bar{v}_x(z) - \mathrm{i}k\bar{v}_z(z)\right] \tag{A.36}$$

one gets the following intermediate result:

$$-\frac{\mathrm{i}\omega}{\nu}\bar{w}(z) = \left(\frac{\partial^2}{\partial z^2} - k^2\right)\bar{w}(z) \tag{A.37}$$

$$\text{with } \bar{w}(z) = \frac{\partial}{\partial z}\bar{v}_x(z) - \mathrm{i}k\bar{v}_z(z). \tag{A.38}$$

(A.37) is solved by

$$\bar{w}(z) = B\cosh(\kappa z) + C\sinh(\kappa z) \tag{A.39}$$

$$\text{with } \kappa = \sqrt{k^2 - \mathrm{i}\omega/\nu},\ \Re(\kappa) > 0 \text{ and } B, C = \text{const.} \tag{A.40}$$

Inserting the continuity condition

$$\underbrace{\frac{\partial}{\partial t}\rho_m}_{=0} + \nabla\vec{v} = 0 \tag{A.41}$$

$$\Rightarrow \mathrm{i}k\bar{v}_x(z) + \frac{\partial}{\partial z}\bar{v}_z(z) = 0 \tag{A.42}$$

into (A.38) yields

$$\bar{w}(z) = \frac{\partial}{\partial z}\bar{v}_x(z) - \mathrm{i}k\bar{v}_z(z) \tag{A.43}$$

$$= \frac{\mathrm{i}}{k}\frac{\partial^2}{\partial z^2}\bar{v}_z(z) - \mathrm{i}k\bar{v}_z(z) \tag{A.44}$$

$$\tag{A.45}$$

$$\Leftrightarrow -\mathrm{i}k\bar{w} = \left(\frac{\partial^2}{\partial z^2} - k^2\right)\bar{v}_z(z) \tag{A.46}$$

To solve this inhomogeneous differential equation for $\bar{v}_z(z)$, the Green's function of $L = -(\partial^2/\partial z^2 - k^2)$ is calculated first, as this is a standard problem with a fairly straight-forward solution. To ensure continuity at the hard wall, one stipulates

$$\bar{v}_z(z=0) = \frac{\partial}{\partial z}\bar{v}_z(z=0) = 0. \tag{A.47}$$

This is the homogeneous initial-value-problem, and therefore the Green's function has the form

$$G_L(z,z') = \begin{cases} 0 & z < z' \\ A_L \mathrm{e}^{-kz} + B_L \mathrm{e}^{kz} & z > z' \end{cases} \tag{A.48}$$

with $\phi_\pm(z) = \mathrm{e}^{\pm kz}$ apparently forming a set of linearly independent solutions[1] of $L\phi = 0$. Applying the usual continuity and 'jump' conditions yields for $z > z'$ [7]

$$0 = \lim_{z\to z',-} G_L(z,z') = \lim_{z\to z',+} G_L(z,z') \tag{A.49}$$

$$\Rightarrow G_L(z,z') = C_L\left[\mathrm{e}^{-k(z-z')} - \mathrm{e}^{k(z-z')}\right] = -2C_L \sinh[k(z-z')] \tag{A.50}$$

and

$$\lim_{z\to z',+} \frac{\partial}{\partial z} - \underbrace{\lim_{z\to z',-} \frac{\partial}{\partial z}}_{=0} = -1 \tag{A.51}$$

$$\Rightarrow G_L(z,z') = \frac{-1}{k}\sinh[k(z-z')]. \tag{A.52}$$

Therefore, the Green's function for $-L = (\partial^2/\partial z^2 - k^2)$ is given by

$$G_{-L}(z,z') = -G_L(z,z') = \frac{1}{k}\sinh[k(z-z')]\theta(z-z'), \tag{A.53}$$

[1] In fact, since the solution space of $L\phi = 0$ is a 2D Hilbert space, any pair of linearly independent solutions forms a basis, leading to the same result.

and the solution of (A.46) is

$$\bar{v}_z(z) = \sum_{\pm} A_{\pm} e^{\pm kz} - i \int_0^{\infty} \sinh[k(z-z')]\theta(z-z')\bar{w}(z')\,dz' \quad (A.54)$$

$$= \sum_{\pm} A_{\pm} e^{\pm kz} - i \int_0^{z} \sinh[k(z-z')]\bar{w}(z')\,dz'. \quad (A.55)$$

The boundary conditions (A.47) yield $A_{\pm} = 0$ (as well as via (A.42) $\bar{v}_x(z=0) = 0$). Therefore, one can now write (inserting (A.39)) the following expression for $\bar{v}_z$:

$$\bar{v}_z(z) = -i \int_0^{z} \sinh[k(z-z')] \left[B\cosh(\kappa z') + C\sinh(\kappa z')\right] dz' \quad (A.56)$$

$$= \frac{-i}{\kappa^2 - k^2} \Big[B\left(\kappa \sinh[k(z-z')]\sinh(\kappa z') + k\cosh[k(z-z')]\cosh(\kappa z')\right) \quad (A.57)$$

$$+C\left(\kappa \sinh[k(z-z')]\cosh(\kappa z') + k\cosh[k(z-z')]\sinh(\kappa z')\right) \Big]_{z'=0}^{z} \quad (A.58)$$

$$= \frac{-i}{\kappa^2 - k^2} \left[Bk\cosh(\kappa z) + Ck\sinh(\kappa z) - Bk\cosh(kz) - C\kappa\sinh(kz)\right] \quad (A.59)$$

$$= \frac{-i}{k^2 - \kappa^2} \left[Bk(\cosh(kz) - \cosh(\kappa z)) + C(\kappa\sinh(kz) - k\sinh(\kappa z))\right] \quad (A.60)$$

$$= -i\left[\hat{B}k(\cosh(kz) - \cosh(\kappa z)) + \hat{C}(\kappa\sinh(kz) - k\sinh(\kappa z))\right] \quad (A.61)$$

$$\text{with} \qquad C/\hat{C} = B/\hat{B} = (k^2 - \kappa^2). \quad (A.62)$$

The corresponding expression for $\bar{v}_x(z)$ can be determined via the continuity condition (A.42) to be

$$\bar{v}_x(z) = \hat{B}\left(k\sinh(kz) - \kappa\sinh(\kappa z)\right) + \hat{C}\kappa\left(\cosh(kz) - \cosh(\kappa z)\right). \quad (A.63)$$

Using the x component of (A.31) and considering (A.40), finally the following equation for the pressure is obtained:

$$\bar{P}/\rho_m = -i\nu(B\sinh(kz) + C(\kappa/k)\cosh(kz)). \quad (A.64)$$

The remaining unknowns are the coefficients B and C, which need to be determined by boundary conditions. At the free surface ($z = h$), these are [33, 41]:

$$\left.\frac{\partial}{\partial z}v_x + \frac{\partial}{\partial x}v_z\right|_{z=h} = 0 \quad (A.65)$$

$$\text{and } -P + 2\eta\left.\frac{\partial}{\partial z}v_z\right|_{z=h} = \gamma\frac{\partial^2}{\partial x^2}u_z - g\rho_m u_z + P_z \quad (A.66)$$

with the vertical surface displacement

$$u_z = \frac{\mathrm{i}}{\omega} v_z\big|_{z=h} \tag{A.67}$$

and an external force per area

$$P_z(x,t) = P_{z,0}\exp[\mathrm{i}(kx-\omega t)] \tag{A.68}$$

which acts on the surface in the z direction. γ denotes the liquid's surface tension, and g the gravitational acceleration as usual.

Using again the plane waves ansatz (A.28)-(A.29), the boundary conditions are transformed into

$$\frac{\partial}{\partial z}\bar{v}_x + \mathrm{i}k\bar{v}_z\Big|_{z=h} = 0 \tag{A.69}$$

$$\text{and } -\frac{\bar{P}(z)}{\rho_m} + 2\nu\frac{\partial}{\partial z}\bar{v}_z + \frac{\mathrm{i}}{\omega}\left[\frac{\gamma k^2}{\rho_m} + g\right]\bar{v}_z\Big|_{z=h} = \frac{P_{z,0}}{\rho_m}. \tag{A.70}$$

Considering (A.61) and (A.63), the first condition (A.69) yields the first part of a linear equation system

$$A_{11}\hat{B} + A_{12}\hat{C} = 0 \tag{A.71}$$

with the following coefficients:

$$A_{11} = 2k^2\cosh(kh) - (k^2+\kappa^2)\cosh(\kappa h) \tag{A.72}$$

$$A_{12} = 2k\kappa\sinh(kh) - (k^2+\kappa^2)\sinh(\kappa h). \tag{A.73}$$

For the second part of the equation system, (A.64) is needed as well. Inserting this into the second boundary condition (A.70), one gets

$$A_{21}\hat{B} + A_{22}\hat{C} = \frac{P_{z,0}}{\rho_m} \tag{A.74}$$

with the coefficients

$$\begin{aligned} A_{21} &= -\mathrm{i}\nu\left[(k^2+\kappa^2)\sinh(kh) - 2k\kappa\sinh(\kappa h)\right] \\ &\quad + \frac{k}{\omega}\left[\frac{\gamma k^2}{\rho_m} + g\right]\left[\cosh(kh) - \cosh(\kappa h)\right] \qquad \text{(A.75)} \\ A_{22} &= -\mathrm{i}\nu(k^2+\kappa^2)\frac{\kappa}{k}\cosh(kh) + 2\mathrm{i}\nu k\kappa\cosh(\kappa h) \\ &\quad + \frac{1}{\omega}\left[\frac{\gamma k^2}{\rho_m} + g\right]\left[\kappa\sinh(kh) - k\sinh(\kappa h)\right]. \qquad \text{(A.76)} \end{aligned}$$

Therefore, B and C are determined by the equation system (A.71), (A.74). This can be used to calculate the *dynamic susceptibility*

$$\chi_{zz}(k,\omega) := \frac{u_z}{P_z} = \frac{\mathrm{i}}{\omega}\cdot\frac{\bar{v}_z\big|_{z=h}}{P_{z,0}} \qquad \text{(A.77)}$$

via

$$\begin{aligned} u_z &= \frac{1}{\omega}\left[\hat{B}k\left(\cosh(kh) - \cosh(\kappa h)\right) + \hat{C}\left(\kappa\sinh(kh) - k\sinh(\kappa h)\right)\right] \\ &= \frac{P_{z,0}\left[A_{11}\left(\kappa\sinh(kh) - k\sinh(\kappa h) - A_{12}k\left(\cosh(kh) - \cosh(\kappa h)\right)\right)\right]}{\rho_m\omega\left(A_{22}A_{11} - A_{12}A_{21}\right)} \qquad \text{(A.78)} \end{aligned}$$

as

$$\chi_{zz}(k,\omega) = \frac{A_{11}\left(\kappa\sinh(kh) - k\sinh(\kappa h) - A_{12}k\left(\cosh(kh) - \cosh(\kappa h)\right)\right)}{\rho_m\omega\left(A_{22}A_{11} - A_{12}A_{21}\right)}. \qquad \text{(A.79)}$$

(A.79) is the desired solution for the dynamic susceptibility of a liquid film of arbitrary depth.

A.3 XPCS resolution calculation: MatLab source

In this section, the source code of the MatLab program that was used to analyse the XPCS spectra in this thesis will be listed for reference purposes. The code is meant to be used as a part of the Mfit package provided by the Institut Laue-Langevin (ILL) [23].

```
function [y, name, pnames, pin]=propa_conv(x,p, flag)
% propa_conv : correlation function for
% propagating CW including a resolution function in Q & osc. ►
    beamline
% artifacts
%
% [y, {name, pnames, pin}]=propa_conv_blosc(x,p, {flag})
%
% p(1)    :    contrast (i.e. [0...1])
% p(2)    :    background [ ~1]
% p(3)    :    surface tension [N/m]
% p(4)    :    viscosity [mPa s]
% p(5)    :    density [g/ccm]
% p(6)    :    qx [inv A]
% p(7)    :    qy [inv A]
% p(8)    :    dqx1 [inv A]
% p(9)    :    dqy1 [inv A]
% p(10)   :    dqx2 [inv A]
% p(11)   :    dqy2 [inv A]
% p(12)   :    heterodyne part [%]
% p(13)   :    resolution order
% p(14)   :    number of sigmas in x direction
% p(15)   :    number of sigmas in y direction
% p(16)   :    background of beamline osc
% p(17)   :    main beamline frequency
% p(18)   :    beamline osc dampening
% p(19)   :    qz
```

```
% Author: MS, RMF (modifications 05/2005-04/2006)

%version = 040106
kboltzmann  = 1.380658e-23;
temperature = 300;

if nargin==2;

    contrast   = p(1)                          ;
    background = p(2)                          ;
    bl_background = p(16);
    bl_freq = p(17);
    bl_damp = p(18);
    ratio      = p(12)/100                     ;

    surftension = p(3);
    viscosity = p(4);
    density = p(5);
    qx = p(6);
    qy = p(7);
    dqx1 = p(8);
    dqy1 = p(9);
    dqx2 = p(10);
    dqy2 = p(11);
    qz = p(19);

    sigmaX1 = dqx1 / realsqrt(2*log(2));
    sigmaY1 = dqy1 / realsqrt(2*log(2));
    if (dqx2 == 0.0)
        sigmaX2 = sigmaX1;
    else
        sigmaX2 = dqx2 / realsqrt(2*log(2));
    end
```

```
if (dqy2 == 0.0)
    sigmaY2 = sigmaY1;
else
    sigmaY2 = dqy2 / realsqrt(2*log(2));
end


interpoints = round(p(13)); % interpolation points, >= 0
convwidthX = p(14);    % width of the convol. area (fact. of ►
   sigma, x)
convwidthY = p(15);    % width of the convoluted area (y ►
   direction)

l1 = 3 + 2 * interpoints;
l2 = l1;

lt = l1*l2             ; % total number of points ( Qx & Qy ►
   loops )

q0          = realsqrt((qx)^2 + (qy)^2) ;
gamma0      = 2e+00* (1e-03*viscosity/(1e+03*density))*(1.0e►
   +10*q0)^2 ;
omega0      = 1e+00*((surftension/(1e+03*density))*(1.0e+10*q0)►
   ^3)^0.5   ;

if (sigmaX1==0.0e+00 & sigmaY1==0.0e+00)
    hetero = exp(-gamma0.*x) .* cos(omega0.*x)      ;
    homo   = hetero.^2                              ;
else
    if (sigmaX1==0.0e+00 | sigmaY1==0.0e+00)
    %--- perfect q_y resolution
        if (sigmaY1 == 0.0e+00)
            for n1 = 1 : l1
```

```
            deltaqx      = ((n1-1)/(l1-1) * 2 - 1) * ►
                sigmaX1 * convwidthX;
            q            = realsqrt( (qx+deltaqx)^2 + (qy)►
                ^2 ) ;
            fac(n1)      = 1/q^2 * 1/(realsqrt(2*pi)*►
                sigmaX1)...
                         * exp(-(deltaqx)^2/(2*sigmaX1^2)) ►
                                    ;
            gamma(n1)    = 2e+00* (1e-03*viscosity/(1e+03*►
                density)) * (1.0e+10*q)^2     ;
            omega(n1)    = 1e+00*((surftension/(1e+03*►
                density)) * (1.0e+10*q)^3)^0.5      ;
            func1(:,n1) = fac(n1) * exp(-gamma(n1).*x) .* ►
                cos(omega(n1).*x)    ;
        end
        hetero = (sum(func1')/sum(fac))' ;
        homo   = hetero.^2       ;
    end
%--- perfect q_x resolution
    if (sigmaX1 == 0.0e+00)
        for n2 = 1 : l2
            deltaqy      = ((n2-1)/(l2-1) * 2 - 1) * ►
                sigmaY1 * convwidthY;
            q            = realsqrt( (qx)^2 + (qy+deltaqy)►
                ^2 ) ;
            fac(n2)      = 1/q^2 * 1/(realsqrt(2*pi)*►
                sigmaY1)...
                         * exp(-(deltaqy)^2/(2*sigmaY1^2)) ►
                                    ;
            gamma(n2)    = 2e+00* (1e-03*viscosity/(1e+03*►
                density)) * (1.0e+10*q)^2     ;
            omega(n2)    = 1e+00*((surftension/(1e+03*►
                density)) * (1.0e+10*q)^3)^0.5      ;
```

```
            func1(:,n2) = fac(n2) * exp(-gamma(n2).*x) .* ►
                cos(omega(n2).*x)    ;
        end
        hetero = (sum(func1')/sum(fac))' ;
        homo   = hetero.^2       ;
    end
else
%-- general case : q_x and q_y resolution effects
    m3 = 0 ; % total counter

    for n2 = 1:l2                                % qy ►
        resolution loop
        for n1 = 1:l1                            % qx ►
            resolution loop
            n3 = (n2-1)*l1 + n1;
            deltaqx      = ((n1-1)/(l1-1) * 2 - 1) * ►
                sigmaX1 * convwidthX;
            deltaqy      = ((n2-1)/(l2-1) * 2 - 1) * ►
                sigmaY1 * convwidthY;
            q            = realsqrt( (qx+deltaqx)^2 ...
                                + (qy+deltaqy)^2 ) ►
                                    ;
            gauss(n3)    = 1/(realsqrt(2*pi)*sigmaX1)...
                         * exp(-(deltaqx)^2/(2*sigmaX1^2))►
                           ...
                         * 1/(realsqrt(2*pi)*sigmaY1)...
                         * exp(-(deltaqy)^2/(2*sigmaY1^2));
            fac(n3)      = 1/q^2 .* gauss(n3);
            gamma(n3)    = 2e+00* (1e-03*viscosity/(1e+03*►
                density)) * (1.0e+10*q)^2 ;
            omega(n3)    = 1e+00*((surftension/(1e+03*►
                density)) * (1.0e+10*q)^3)^0.5   ;
```

```
                func1(:,n3) = fac(n3) * exp(-gamma(n3).*x) .* ►
                    cos(omega(n3).*x);
            end
        end
        hetero = (sum(func1')/sum(fac))' ;
        g = 1/(realsqrt(2*pi)*sigmaX2)*exp(-(qx)^2/(2*sigmaX2►
            ^2))* 1/(realsqrt(2*pi)*sigmaY2)* exp(-(qy)^2/(2*►
            sigmaY2^2));%gauss
             %l = sigmaX2/(2*pi)*1/(qx^2+(sigmaX2/2.0)^2) ;%►
                 lorentz

        r = g; % reso function

        hetero = hetero / max(hetero);
        homo   = (hetero*(qz^2)*kboltzmann*temperature/(2*pi*►
            surftension)*1e-20 + r).^2;
        homo   = homo - r^2;        % normalisation #1
        homo   = homo / max(homo); % normalisation #2
    end
end

y = contrast * (ratio * hetero + (1-ratio) * homo) + ►
    background * cos(bl_freq * x) .* exp(-bl_damp * x) + ►
    bl_background ;

else
    y=[];
    name='propa_conv';
    pnames=str2mat('contrast','background','surf. tens. [N/m]',...
                   'viscosity [mPa s]','density [g/ccm]','qx [inv ►
                       A]',...
                   'qy [inv A]','dqx1 [inv A]','dqy1 [inv A]',...
                   'dqx2 [inv A]','dqy2 [inv A]',...
```

```
                'hetero part [%]','interp. points','conv. wid. ►
                    x',...
                'conv. wid. y',...
                'bl osc background', 'bl osc freq', 'bl osc ►
                    dampening',...
                'qz [inv. ?]');
if flag==1
    pin=[2.00e-02,1.00e+00,18.0e-03,0.30e+00,...
        0.69e+00,8.00e-06,0.00e+00,0.00e+00,0.00e►
            +00,0.00e+00,0,3,3,1,0,0,0,3.2e-2] ;
else
    pin = p      ;
end
if flag==2
    mf_msg('Click on bl osc background');
    [x bl_background] = ginput(1);

    mf_msg('Click on bl osc frequency');
    [bl_freq x] = ginput(1);
    bl_freq = pi / (2 * bl_freq);

    mf_msg('Click on background');
    [x background] = ginput(1);
    background = abs(background - bl_background);

    mf_msg('Click on contrast');
    [x contrast] = ginput(1);
    contrast = abs(contrast - background - bl_background);

    pin=[contrast,background,18.0e-03,0.30e+00,...
        0.69e+00,8.00e-06,0.00e+00,0.00e+00,0.00e►
            +00,0.00e+00,0,3,3,1,bl_background,bl_freq,0,3.2e►
            -2] ;
```

```
    end
end
```

A.4 Additional software implementations

For analysing the dynamics data of liquid films, the viscoelastic formalism presented in sections 2.3.2 and A.2 is very useful, especially since it is usually not clear *a priori* whether the simplified Lorentzian power spectrum is a valid approximation. Since the current software implementation of the surface-XPCS calculation including resolution effects assumes the low-viscosity limit to be fulfilled, it is necessary to check beforehand if any corrections are needed.

However, the formula in its most general form is numerically ill-conditioned, meaning that even very small calculation errors (e.g. rounding artifacts) can make the calculation impossible. To be able to calculate the spectrum, an optimised C++ implementation has been written. The implementation uses arbitrary-precision math to compensate for the numerical problems of the formalism and has proven to be fast and stable.

An interface to the Python programming language has been written to simplify usage, and has been successfully tested and used. The source code is available on request, and should compile on most C++ compiler systems and operating systems.

Furthermore, since temperature control is very important during measurements on liquids, a software to control Lakeshore controllers (models 330&340) has been written. The software allows for the automatised readout of temperatures, as well as the control of parameters like set-point, PID parameters and heater power via RS232 connection to the device.

This makes it possible to place the controller virtually anywhere, even inside the hutch, while allowing to control the most important values from the control room. Also, the temperature protocol can be important to check if e.g. insufficient temperature stability is responsible for certain measurement artifacts. Furthermore, arbitrary "temperature ramps" can be implemented, allowing e.g. for a slow approach of the desired temperature.

The software features a graphical user interface allowing for quick visualisation of e.g. temperature gradients, and can be compiled for Windows and for Unix-like operating systems providing POSIX interfaces (e.g., Linux). A binary installer for Windows as well as the source code are available on request.

Bibliography

[1] ABELÈS, F.: Recherches sur la propagation des ondes électromagnétiques sinosoïdales dans les milieux strafifiés. Application aux couches minces. In: *Ann. Phys. (Paris)* 12 (1950), no. 5, p. 596–640, 706–782

[2] ABRAMOWITZ, M. (Ed.) ; STEGUN, I. (Ed.): *Handbook of Mathematical Functions: with Formulas, Graphs, and Mathematical Tables*. New Ededition. Dover Publications, 1965

[3] *Advanced Photon Source*. `http://www.aps.anl.gov/`

[4] AJAEV, V. S.: Evolution of dry patches in evaporating liquid films. In: *Phys. Rev. E* 72 (2005), no. 3, p. 031605

[5] ALS-NIELSEN, J. ; MCMORROW, D.: *Elements of Modern X-Ray Physics*. Wiley, 2001

[6] ANDELMAN, D. ; JOANNY, J.-F. ; ROBBINS, M.O.: Complete wetting on rough surfaces: Statics. In: *Europhys. Lett.* 7 (1988), no. 8, p. 731

[7] BARTON, G.: *Elements of Green's Functions and Propagation*. Reprint (with corrections). Oxford Science Publications, 1989, 1991

[8] BORN, M. ; WOLF, E.: *Principles of Optics*. 7th edition. Cambridge University Press, 1999

[9] BRASLAU, A. ; PERSHAN, P. S. ; SWISLOW, G. ; OCKO, B. M. ; ALS-NIELSEN, J.: Capillary waves on the surface of simple liquids measured by x-ray reflectivity. In: *Phys. Rev. A* 38 (1988), no. 5, p. 2457

[10] BRAUN, C.: *Parratt32*. Hahn-Meitner-Institut, Berlin, Germany. `http://www.hmi.de/bensc/instrumentation/instrumente/v6/refl/parratt_en.htm`. – Software for X-ray and neutron reflectivity calculation.

[11] BRONSTEIN, I. N. ; SEMENDJAJEW, K. A. ; MUSIOL, G. ; MÜHLIG, H.: *Taschenbuch der Mathematik*. 3. Auflage. Verlag Harri Deutsch, 1997

[12] CAI, Z. H. ; LAI, B. ; YUN, W. B. ; MCNULTY, I. ; HUANG, K. G. ; RUSSELL, T. P.: Observation of X-Ray Speckle by Coherent Scattering at Grazing Incidence. In: *Phys. Rev. Lett.* 73 (1994), no. 1, p. 82

[13] DAVID, C. ; NÖHAMMER, B. ; SOLAK, H. H. ; ZIEGLER, E.: Differential x-ray phase contrast imaging using a shearing interferometer. In: *Appl. Phys. Lett.* 81 (2002), no. 17, p. 3287

[14] DERNE, B. J. ; PECORA, R.: *Dynamic light scattering*. Wiley, 1976

[15] DIERKER, S. B. ; PINDAK, R. ; FLEMING, R. M. ; ROBINSON, I. K. ; BERMAN, L.: X-Ray Photon Correlation Spectroscopy Study of Brownian Motion of Gold Colloids in Glycerol. In: *Phys. Rev. Lett.* 75 (1995), no. 3, p. 449

[16] DOERR, A. K.: *Untersuchung der strukturellen Eigenschaften dünner Benetzungsfilme*. Kiel, Christian-Albrechts-Universität, PhD thesis, 1999

[17] DOERR, A. K. ; TOLAN, M. ; PRANGE, W. ; SCHLOMKA, J.-P. ; SEYDEL, T. ; PRESS, W. ; SMILGIES, D. ; STRUTH, B.: Observation of Capillary Waves on Liquid Thin Films from Mesoscopic to Atomic Length Scales. In: *Phys. Rev. Lett.* 83 (1999), no. 17, p. 3470

[18] *DOW Glycerine: Viscosity*. `http://www.dow.com/glycerine/resources/viscosity.htm`. – online ressource, last checked: 2006-12-01

[19] EARNSHAW, J. C.: Surface light scattering: a methodological review. In: *Appl. Opt.* 36 (1997), p. 7583

[20] EARNSHAW, J. C. ; ROBINSON, D. J.: Dynamic light scattering from colloidal monolayers. In: *Journal of Physics: Condensed Matter* 2 (1990), no. 46, p. 9199

[21] EISEBITT, S. ; LUNING, J. ; SCHLOTTER, W. F. ; LORGEN, M. ; HELLWIG, O. ; EBERHARDT, W. ; STOHR, J.: Lensless imaging of magnetic nanostructures by X-ray spectro-holography. In: *Nature* 432 (2004), p. 885

[22] *European Synchrotron Radiation Facility*. `http://www.esrf.fr/`

[23] FARHI, E. u. a.: *Mfit*. Institut Laue-Langevin, Grenoble, France. `http://www.ill.fr/tas/matlab/doc/`. – General purpose data fitting and analysis software package.

[24] FENDT, R.: *Strukturuntersuchungen an dünnen Flüssigkeitsfilmen*, Universität Dortmund, Master's thesis, 2003

[25] GENNES, P. G.: Wetting: statics and dynamics. In: *Rev. Mod. Phys.* 57 (1985), no. 3, p. 827

[26] GERVASIO, F. L. ; CARLONI, P. ; PARRINELLO, M.: Electronic Structure of Wet DNA. In: *Phys. Rev. Lett.* 89 (2002), no. 10, p. 108102

[27] GHADERI, T.: *X-ray Intensity Correlation Spectroscopy from Fluid Surfaces*, Universität Dortmund, PhD thesis, 2006

[28] GRIGORIEV, I. S. (Ed.) ; MEILIKHOV, E. J. (Ed.): *Handbook of Physical Quantities*. CRC Press, 1997

[29] GUTT, C. ; GHADERI, T. ; CHAMARD, V. ; MADSEN, A. ; SEYDEL, T. ; TOLAN, M. ; SPRUNG, M. ; GRÜBEL, G. ; SINHA, S. K.: Observation of Heterodyne Mixing in Surface X-Ray Photon Correlation Spectroscopy Experiments. In: *Phys. Rev. Lett.* 91 (2003), no. 7, p. 076104

[30] GUTT, C. ; SPRUNG, M. ; FENDT, R. u. a.: *Influence of coherence in XPCS measurements*. 2006. – to be published

[31] GUTT, C. ; SPRUNG, M. ; FENDT, R. u. a.: *The surface structure of vapor deposited thin liquids film in a partial wetting situation*. 2006. – to be published

[32] HENDERSON, J. R.: Statistical mechanics of the disjoining pressure of a planar film. In: *Phys. Rev. E* 72 (2005), no. 5, p. 051602

[33] JÄCKLE, J.: The spectrum of surface waves on viscoelastic liquids of arbitrary depth. In: *J. Phys.: Cond. Mat.* 10 (1998), no. 32, p. 7121–7131

[34] JÄCKLE, J. ; KAWASAKI, K.: Intrinsic roughness of glass surfaces. In: *J. Phys.: Cond. Mat.* 7 (1995), no. 23, p. 4351–4358

[35] JACKSON, J. D.: *Classical Electrodynamics*. Third edition. John Wiley & Sons, 1999

[36] JAKEMAN, E.: The effect of heterodyne detection on the statistical accuracy of optical linewidth measurements. In: *J. Phys. A: Gen. Phys.* 5 (1972), p. L49

[37] JAMES, R. W.: *The Optical Principles of the Diffraction of X-Rays*. Ox Bow Press, 1982

[38] *Korea thermophysical properties Data Bank*. `http://www.cheric.org/kdb/`. – online ressource, last checked: 2006-12-01

[39] KERN, W. (Ed.): *Handbook of Semiconductor Wafer Cleaning Technology – Science, Technology, and Applications*. Noyes, 1993

[40] KIM, H. ; RUHM, A. ; LURIO, L. B. ; BASU, J. K. ; LAL, J. ; LUMMA, D. ; MOCHRIE, S. G. J. ; SINHA, S. K.: Surface Dynamics of Polymer Films. In: *Phys. Rev. Lett.* 90 (2003), no. 6, p. 068302

[41] LAMB, H.: *Lehrbuch der Hydrodynamik*. Zweite Auflage. Teubner, 1931

[42] LANDOLT, H. H. ; BÖRNSTEIN, R.: *Zahlenwerte und Funktionen aus Physik, Chemie, Astronomie, Geophysik und Technik*. 6. Auflage. Springer, 1956. – Band II/3

[43] LANDOLT, H. H. ; BÖRNSTEIN, R.: *Zahlenwerte und Funktionen aus Physik, Chemie, Astronomie, Geophysik und Technik*. 6. Auflage. Springer, 1969. – Band II/5

[44] LANDOLT, H. H. ; BÖRNSTEIN, R.: *Numerical Data and Functional Relationships in Science and Technology*. New Series. Springer, 1997. – Vol. IV/16

[45] LANDOLT, H. H. ; BÖRNSTEIN, R.: *Numerical Data and Functional Relationships in Science and Technology*. New Series. Springer, 2001. – Vol. IV/18A

[46] LEITENBERGER, W. ; WENDROCK, H. ; BISCHOFF, L. ; WEITKAMP, T.: Pinhole interferometry with coherent hard X-rays. In: *J. Synchr. Rad.* 11 (2004), no. 2, p. 190

[47] LENGELER, B.: Coherence in X-ray physics. In: *Naturwissenschaften* 88 (2001), no. 6, p. 249

[48] LEVICH, V. G.: *Physicochemical Hydrodynamics*. Second edition. Prentice-Hall, Englewood Cliffs, 1962

[49] LIBBERT, J. L. ; PINDAK, R. ; DIERKER, S. B. ; ROBINSON, I. K.: Speckle in coherent x-ray reflectivity from Si(111) wafers. In: *Phys. Rev. B* 56 (1997), no. 11, p. 6454

[50] LIBBERT, J. L. ; PITNEY, J. A. ; ROBINSON, I. K.: Asymmetric Fraunhofer Diffraction from Roller-Blade Slits. In: *J. Synchr. Rad.* 4 (1997), no. 3, p. 125

[51] LIDE, D. R. (Ed.): *CRC Handbook of Chemistry and Physics*. 79th edition. CRC Press, 1997

[52] LIN, B. ; SCHLOSSMAN, M. L. ; MERON, M. ; WILLIAMS, S. M. ; VICCARO, P. J.: Characterization of x-ray spatial coherence and its propagation. In: *Rev. Sci. Instr.* 67 (1996), no. 9, p. 3363

[53] LIVET, F. ; BLEY, F. ; EHRBURGER-DOLLE, F. ; MORFIN, I. ; GEISSLER, E. ; SUTTON, M.: X-ray intensity fluctuation spectroscopy by heterodyne detection. In: *J. Synchr. Rad.* 13 (2006), no. 6, p. 453

[54] MADSEN, A. ; SEYDEL, T. ; SPRUNG, M. ; GUTT, C. ; TOLAN, M. ; GRÜBEL, G.: Capillary Waves at the Transition from Propagating to Overdamped Behavior. In: *Phys. Rev. Lett.* 92 (2004), no. 9, p. 096104

[55] MADSEN, A. ; SEYDEL, T. ; TOLAN, M. ; GRÜBEL, G.: Grazing-incidence scattering of coherent X-rays from a liquid surface. In: *J. Synchr. Rad.* 12 (2005), no. 6, p. 786

[56] MANDEL, L. ; WOLF, E.: *Optical coherence and quantum optics*. Cambridge university press, 1995

[57] MIAO, J. ; ISHIKAWA, T. ; JOHNSON, B. ; ANDERSON, E. H. ; LAI, B. ; HODGSON, K. O.: High Resolution 3D X-Ray Diffraction Microscopy. In: *Phys. Rev. Lett.* 89 (2002), no. 8, p. 88303

[58] MOCHRIE, S. G. J. ; MAYES, A. M. ; SANDY, A. R. ; SUTTON, M. ; BRAUER, S. ; STEPHENSON, G. B. ; ABERNATHY, D. L. ; GRÜBEL, G.: Dynamics of Block Copolymer Micelles Revealed by X-Ray Intensity Fluctuation Spectroscopy. In: *Phys. Rev. Lett.* 78 (1997), no. 7, p. 1275

[59] MÜLLER-BUSCHBAUM, P.: *Röntgenstreuung and flüssigen Benetzungsfilmen*. Kiel, Christian-Albrechts-Universität, PhD thesis, 1996

[60] NEUHÄUSLER, U. ; SCHNEIDER, G. ; LUDWIG, W. ; MEYER, M. A. ; ZSCHECH, E. ; HAMBACH, D.: X-ray microscopy in Zernike phase contrast mode at 4 keV photon energy with 60 nm resolution. In: *J. Phys. D: Appl. Phys.* 36 (2003), p. A79

[61] NUGENT, K. A.: Partially coherent diffraction patterns and coherence measurement. In: *J. Opt. Soc. Am.* 8 (1991), no. 10, p. 1574

[62] NUGENT, K. A. ; TREBES, J. E.: Coherence measurement technique for short-wavelength light sources. In: *Rev. Sci. Instr.* 63 (1992), no. 4, p. 2146

[63] PARRATT, L. G.: Surface Studies of Solids by Total Reflection of X-Rays. In: *Phys. Rev.* 95 (1954), no. 2, p. 359–369

[64] PAULUS, M. ; GUTT, C. ; TOLAN, M.: Surface roughness and adsorption isotherms of molecularly thin liquid films: An x-ray reflectivity study. In: *Phys. Rev. E* 72 (2005), no. 6, p. 061601

[65] PFOHL, T. ; RIEGLER, H.: Critical Wetting of a Liquid/Vapor Interface by Octane. In: *Phys. Rev. Lett.* 82 (1999), no. 4, p. 783

[66] PIETSCH, U.: *Anomalous XPCS*. 2005. – private communication

[67] PIETSCH, U. ; HOLÝ, V. ; BAUMBACH, T.: *High-Resolution X-Ray Scattering*. Second edition. Springer, 2004

[68] PIETSCH, U. ; PANZNER, T. ; LEITENBERGER, W. ; VARTANYANTS, I.: Coherence experiments using white synchrotron radiation. In: TOLAN, M. (Ed.) ; SALDITT, T. (Ed.) ; SCHREYER, A. (Ed.): *Proceedings of the Eighth International Conference on Surface X-ray and Neutron Scattering, SXNS-8 (2004)*, Elsevier, 2005, p. 45

[69] RETSCH, C. C. ; MCNULTY, I.: X-Ray Speckle Contrast Variation across Absorption Edges. In: *Phys. Rev. Lett.* 87 (2001), no. 7, p. 77401

[70] ROBBINS, M. O. ; ANDELMAN, D. ; JOANNY, J.-F.: Thin liquid films on rough or heterogeneous solids. In: *Phys. Rev. A* 43 (1991), no. 8, p. 4344

[71] ROBINSON, I. K. ; PINDAK, R. ; FLEMING, R. M. ; DIERKER, S. B. ; PLOOG, K. ; GRÜBEL, G. ; ABERNATHY, D. L. ; ALS-NIELSEN, J.: Observation and explanation of one-dimensional x-ray speckle patterns from synthetic multilayers. In: *Phys. Rev. B* 52 (1995), no. 14, p. 9917

[72] ROBINSON, I. K. ; PITNEY, J. A. ; LIBBERT, J. L. ; VARTANYANTS, I. A.: Surface morphology by reflectivity of coherent X-rays. In: *Physica B* 248 (1998), p. 387

[73] ROCHE, P. ; DEVILLE, G. ; KESHISHEV, K. O. ; APPLEYARD, N. J. ; WILLIAMS, F. I. B.: Low Damping of Micron Capillary Waves on Superfluid ^{4}He. In: *Phys. Rev. Lett.* 75 (1995), no. 18, p. 3316

[74] ROSHI, A. ; BARJAMI, S. ; IANNACCHIONE, G. S. ; PATERSON, D. ; MCNULTY, I.: Structure and dynamics of a nanocolloidal silica gel dispersion. In: *Phys. Rev. E* 74 (2006), no. 3, p. 31404

[75] SCHÄFFER, Erik ; WONG, Po-zen: Dynamics of Contact Line Pinning in Capillary Rise and Fall. In: *Phys. Rev. Lett.* 80 (1998), no. 14, p. 3069

[76] SEECK, O. H.: *LSFIT*. Available on request from the author, 1999. – Software for X-ray and neutron reflectivity calculation.

[77] SEYDEL, T. ; MADSEN, A. ; TOLAN, M. ; GRÜBEL, G. ; PRESS, W.: Capillary waves in slow motion. In: *Phys. Rev. B* 63 (2001), no. 7, p. 073409

[78] SEYDEL, T. ; TOLAN, M. ; OCKO, B. M. ; SEECK, O. H. ; WEBER, R. ; DIMASI, E. ; PRESS, W.: Freezing of capillary waves at the glass transition. In: *Phys. Rev. B* 65 (2002), no. 18, p. 184207

[79] SHOKUIE, K.: *Untersuchungen an ultradünnen Alkanfilmen auf Silizium mittels Röntgenreflektometrie*, Universität Dortmund, Master's thesis, 2005

[80] SINHA, S. K. ; SIROTA, E. B. ; GAROFF, S. ; STANLEY, H. B.: X-ray and neutron scattering from rough surfaces. In: *Phys. Rev. B* 38 (1988), no. 4, p. 2297

[81] SINHA, S. K. ; TOLAN, M. ; GIBAUD, A.: Effects of partial coherence on the scattering of x rays by matter. In: *Phys. Rev. B* 57 (1998), no. 5, p. 2740

[82] SPRUNG, M. ; GUTT, C. u. a.: *XPCS measurements on n-Hexane*. 2003. – unpublished experimental data (ID10A, ESRF)

[83] SPRUNG, M. ; SEYDEL, T. ; GUTT, C. ; WEBER, R. ; DIMASI, E. ; MADSEN, A. ; TOLAN, M.: Surface roughness of supercooled polymer melts. In: *Phys. Rev. E* 70 (2004), no. 5, p. 51809

[84] STADLER, L.-M. ; SEPIOL, B. ; KANTELHARDT, J. W. ; ZIZAK, I. ; GRÜBEL, G. ; VOGL, G.: Revealing antiphase-domain dynamics in alloys by combining advanced statistical techniques with x-ray photon correlation spectroscopy. In: *Phys. Rev. B* 69 (2004), no. 22, p. 224301

[85] STETTNER, J.: *Charakterisierung von rauhen MBE-$CoSi_2$/Si-Schichtsystemen mittels Röntgenstreuung*. Kiel, Christian-Albrechts-Universität, PhD thesis, 1995

[86] STREIT, S. ; GUTT, C. ; CHAMARD, V. ; ROBERT, A. ; SPRUNG, M. ; STERNEMANN, H. ; TOLAN, M.: *Two dimensional dynamics of metal nanoparticles on the surface of thin polymer films studied with coherent x-rays*. 2006. – to be published

[87] The surface gratings were provided by the Department of Electrical Engineering of the University of Dortmund, High Frequency Institute (group of E. Voges).

[88] THOMPSON, A. C. (Ed.) ; VAUGHAN, D. (Ed.): *X-Ray Data Booklet*. Second edition. Lawrence Berkeley National Laboratory, 2001

[89] THURN-ALBRECHT, T. ; STEFFEN, W. ; PATKOWSKI, A. ; MEIER, G. ; FISCHER, E. W. ; GRÜBEL, G. ; ABERNATHY, D. L.: Photon Correlation Spectroscopy of Colloidal Palladium Using a Coherent X-Ray Beam. In: *Phys. Rev. Lett.* 77 (1996), no. 27, p. 5437

[90] THURN-ALBRECHT, T. ; ZONTONE, F. ; GRÜBEL, G. ; STEFFEN, W. ; MÜLLER-BUSCHBAUM, P. ; PATKOWSKI, A.: Photon correlation spectroscopy with high-energy coherent x rays. In: *Phys. Rev. E* 68 (2003), no. 3, p. 31407

[91] TIDSWELL, I. M. ; RABEDEAU, T. A. ; PERSHAN, P. S. ; KOSOWSKY, S. D.: Complete wetting of a rough surface: An x-ray study. In: *Phys. Rev. Lett.* 66 (1991), no. 16, p. 2108

[92] TOLAN, M.: *X-ray scattering from soft matter thin films*. Springer, 1999 (Springer Tracts in Modern Physics)

[93] TOLAN, M. ; SEECK, O. H. ; SCHLOMKA, J.-P. ; PRESS, W. ; WANG, J. ; SINHA, S. K. ; LI, Z. ; RAFAILOVICH, M. H. ; SOKOLOV, J.: Evidence for Capillary Waves on Dewetted Polymer Film Surfaces: A Combined X-ray and Atomic Force Microscopy Study. In: *Phys. Rev. Lett.* 81 (1998), no. 13, p. 2731

[94] VLIEG, E. ; VRIES, S. A. D. ; ALVAREZ, J. ; FERRER, S.: Slits as Adjustable Pinholes for Coherent X-ray Scattering Experiments. In: *J. Synchr. Rad.* 4 (1997)), no. 4, p. 210

[95] WANG, J. ; SOOD, A. K. ; SATYAM, P. V. ; FENG, Y. ; WU, X. ; CAI, Z. ; YUN, W. ; SINHA, S. K.: X-Ray Fluorescence Correlation Spectroscopy: A Method for Studying Particle Dynamics in Condensed Matter. In: *Phys. Rev. Lett.* 80 (1998), no. 5, p. 1110

Index